

ULTRASONICALLY CONTROLLED/POWERED IMPLANTABLE MEDICAL DEVICES

by

Jiawei Zhou

A Dissertation

Submitted to the Faculty of Purdue University

In Partial Fulfillment of the Requirements for the degree of

Doctor of Philosophy



School of Electrical & Computer Engineering

West Lafayette, Indiana

December 2018

THE PURDUE UNIVERSITY GRADUATE SCHOOL
STATEMENT OF COMMITTEE APPROVAL

Dr. Babak Ziaie, Chair

School of Electrical and Computer Engineering

Dr. Saeed Mohammadi

School of Electrical and Computer Engineering

Dr. Çağrı A. Savran

School of Mechanical Engineering

Dr. Kinam Park

Weldon School of Biomedical Engineering

Approved by:

Dr. Pedro Irazoqui

Head of the Graduate Program

*This dissertation is dedicated to my family, my father, Jing Zhou,
my mother Guangyu Meng and
my wife, Danni Huang with my gratitude for their support, encouragement and love.*

ACKNOWLEDGMENTS

I am grateful to many people who have helped me along this odyssey towards my degree. This dissertation and my work could not be completed without their support. I want to mention everyone here but there are surely people who may not appear on the page but have influenced me profoundly during my growth. I would like to firstly thank those who contribute to the completion of this work.

I would express my forever gratitude to my parents, Mr. Jing Zhou and Ms. Guangyu Meng, and my love, Ms. Danni Huang. I thank them for their endless love, support as I pursue this degree and their encouragement during the hardest time of my life. I could not achieve such accomplishment without their help and care.

I want to thank my academic adviser and mentor, Professor Babak Ziaie for his patience, guidance, support and enlightenment during my research and study at Purdue University. His insightful opinion and horizons have taught me to develop creative and critical thinking patterns for theoretical problems and realistic challenges. I appreciate his advice towards both my life and study, discussion with us during the group meeting and delightful talk during conference travels and group dinners. He created a perfect atmosphere in the group for conducting researches.

I would like to thank all the nice people I met at Purdue University during our collaboration on research. I want to firstly thank all my academic committee members, Professor Kinam Park, Professor Çağrı A. Savran, and Professor Saeed Mohammadi, for their support during my Ph.D. studies. I am also grateful to Dr. Albert Kim, Dr. Seung Hyun Song, Mr. Shayak Samaddar, Dr. Bennett D. Elzey, Dr. David H. Thompson, Mr. Sayemul Islam, Mr. Tianshuo Zhang, Mr. Benjamin Ramsey and Mrs. Sandra Torregrosa-Allen for their assistance and contributions to the completion of this dissertation.

I also want to extend my thanks to all the staff at Birck Nanotechnology Center for their help in maintaining the lab and assistance during my researches, and all my colleagues and friends from Ziaie Biomedical Microdevices Laboratory (ZBML). I want to thank Dr. Manuel Ochoa, Dr. Rahim Rahimi, Dr. Hongjie Jiang, Dr. Wuyang Yu, Dr. Tejasvi Parupudi, Dr. Chang Keun Yoon, Dr. Jun Hyeong Park, Dr. Seung Seob Lee, Ms. Farah Alimagham, Mr. Zachariah Hughes, Mr. Vaibhav Jain, Mr. Junyoung Kim, Ms. Rebeca Hannah Olivera, Mr. Mark Ocai, Mr. Tianlin Tan, Mr. Lior Ben Yehoshua, and all my other lab colleagues.

TABLE OF CONTENTS

LIST OF TABLES	7
LIST OF FIGURES	8
ABSTRACT	10
1. INTRODUCTION	11
1.1 Motivation and Background	11
1.2 Organization of the Dissertation	15
2. ULTRASOUND GENERATION AND COUPLING.....	16
2.1 Introduction.....	16
2.1.1 Inductive Powering.....	16
2.1.2 Capacitive Powering.....	17
2.1.3 Optical Wireless Powering	18
2.1.4 Ultrasonic Coupling.....	19
2.2 Piezoelectricity and Piezo-Materials.....	20
2.2.1 Lead Zirconate Titanate (PZT)	21
2.2.2 Polyvinylidene Fluoride (PVDF).....	21
2.2.3 New Materials.....	22
2.3 Output Voltage and Omnidirectionality of Acoustic Powering.....	22
2.4 Transmission Model and Equivalent Circuit	25
2.5 The Acoustic Field in Near-Field Region.....	27
3. FREQUENCY MATCHING AND ACOUSTIC MATCHING FOR TRANSDUCERS.....	35
3.1 Introduction.....	35
3.2 Electrical Impedance of PZT	35
3.3 Acoustic Impedance of Materials	42
4. ULTRASONICALLY CONTROLLED POWER MANAGEMENT SYSTEM	50
4.1 Introduction.....	50
4.2 Background and System Overview.....	50
4.2.1 Device Operation	51
4.2.2 Circuit Schematic.....	52
4.3 Fabrication	54

4.4	Experimental Results	56
4.4.1	<i>In Vitro</i> Results	56
4.4.2	<i>Ex Vivo</i> Results	60
4.5	Conclusion	60
5.	AN IMPLANTABLE MINITUARIZED LIGHT SOURCE FOR LOCALIZED PHOTODYNAMIC THERAPY.....	62
5.1	Introduction.....	62
5.2	Background and System Overview.....	62
5.3	Fabrication	64
5.4	Experimental Results	65
5.4.1	Validation of Ultrasonic Powered Light Source.....	65
5.4.2	<i>Ex Vivo</i> Results	69
5.4.3	<i>In Vitro</i> Results	69
5.4.4	<i>In Vivo</i> Results	71
5.5	Conclusion	73
6.	ULTRASONICALLY POWERED MICRO-IMPLANT FOR COMBINED PHOTODYNAMIC AND ELECTROLYTIC TUMOR ABLATION.....	75
6.1	Introduction.....	75
6.2	Background and System Overview.....	75
6.2.1	Circuit Schematic.....	76
6.2.2	System Operation.....	77
6.3	Fabrication	78
6.4	Experimental Results	78
6.4.1	Induced pH Change	79
6.4.2	Light and Electrical Output Evaluation	80
6.4.3	Oxygen Generation.....	82
6.5	Conclusion	82
	REFERENCES	84
	VITA	93
	PUBLICATIONS.....	94

LIST OF TABLES

Table 1.1 Electrical power consumption for different applications.....	12
Table 2.1 Mechanical properties of PZT-5A	26
Table 4.1 Output characteristics of some common D flip-flops	59
Table 4.2 UCPMS current consumption as compared to several commercial RF SoC systems ..	59
Table 5.1 Specifications of the components used in the μ Light	65
Table 5.2 Photosensitizers and estimated treatment time using μ Light.....	68

LIST OF FIGURES

Figure 1.1 A high power closely coupled wireless powering system.....	13
Figure 2.1 Wireless powering system with magnitude control from external primary side.....	17
Figure 2.2 The simplified capacitive coupling link equivalent circuit	18
Figure 2.3 The schematic of near-infrared laser enabled wireless recharging system	19
Figure 2.4 Schematic of ultrasonic powering system for implantable devices.....	20
Figure 2.5 Input acoustic waves induce charge generation along poling direction.	22
Figure 2.6 Illustration for omni-directional powering using ultrasonic wave	23
Figure 2.7 Normalized power output at various axial angular misalignments	24
Figure 2.8 Schematic of the KLM model for the ultrasonic communication link.	25
Figure 2.9 Near-field boundary calculation of a circular transducer	27
Figure 2.10 Near-field boundary calculation of a rectangular transducer	29
Figure 2.11 Non-reflective condition transmission measurement	30
Figure 2.12 Picture of water tank setup used for acoustic transmission measurement.....	31
Figure 2.13 Measured acoustic intensity at various locations away from the transducer.....	31
Figure 2.14 Measured acoustic intensity along central axis	32
Figure 2.15 Measured output voltage along central axis	33
Figure 2.16 Measured acoustic intensity with reflection	33
Figure 2.17 Measured output voltage along central axis	34
Figure 3.1 Impedance spectrum analysis of 1 mm PZT disk.....	36
Figure 3.2 Impedance spectrum analysis of 2 mm PZT disk.....	36
Figure 3.3 Impedance spectrum of $1 \times 10 \times 10 \text{ mm}^3$ thick PZT	37
Figure 3.4 Impedance spectrum of $1 \times 1 \times 5 \text{ mm}^3$ thick PZT	38
Figure 3.5 Impedance spectrum of $1 \times 1 \times 1 \text{ mm}^3$ thick PZT	38
Figure 3.6 Impedance spectrum of $1 \times 1 \times 1 \text{ mm}^3$ thick PZT	39
Figure 3.7 Impedance spectrum of $1 \times 1 \times 1 \text{ mm}^3$ thick PZT	40
Figure 3.8 Impedance spectrum analysis of $1 \times 1 \times 5 \text{ mm}^3$ PZT	40
Figure 3.9 Impedance spectrum analysis of $2 \times 2 \times 2 \text{ mm}^3$ PZT	41
Figure 3.10 Impedance spectrum analysis of $2 \times 4 \times 2 \text{ mm}^3$ PZT	41
Figure 3.11 Acoustic reflection at air-water interface	43
Figure 3.12 Configuration of ultrasonic transducer consisting of three layers.....	43

Figure 3.13 Three-layer structure for the case of impedance matching layer	44
Figure 3.14 Matching layer structure for PZT enabled ultrasonic powering.....	45
Figure 3.15 Fabricated ultrasonic powered device packaging with acoustic matching.....	46
Figure 3.16 Sound travelling velocity measurement	47
Figure 3.17 Power transmission calculation at 2.3 MHz with 3D printing material	48
Figure 3.18 Power transmission water tank setup for matching layer.....	48
Figure 3.19 Measured transmitted acoustic intensity at 2.3 MHz	49
Figure 4.1 System block diagram	52
Figure 4.2 Circuit diagram of the UCPMS and signal patterns at four points.....	54
Figure 4.3 Fabrication process.....	55
Figure 4.4 Rectified output voltage at various distance along central axis	56
Figure 4.5 Rectified output voltage at various lateral distance in a non-reflective condition	56
Figure 4.6 Switching time of UCPMS.....	57
Figure 4.7 I-V output characterization of UCPMS	58
Figure 4.8 Ex vivo experiment setup.	60
Figure 5.1 Photosensitizer, μ Light in a tumor, equivalent transmission diagram for ultrasonic powering, fabrication process.	64
Figure 5.2 Light irradiance characterizations of μ Light without reflection.....	67
Figure 5.3 Light intensity with reflections.....	67
Figure 5.4 Ex vivo light penetration through bovine tissue.....	69
Figure 5.5 LD50 value measurement.....	70
Figure 5.6 Experiment for cell culture essay	72
Figure 6.1 Schematic of the combined EA-PDT system.	77
Figure 6.2 Fabrication process.....	78
Figure 6.3 Characterization for ultrasonic powering and pH measurement	80
Figure 6.4 Light intensity under various acoustic inputs.....	81
Figure 6.5 Output voltage across electrodes under various acoustic inputs.	81
Figure 6.6 Dissolved oxygen concentration increases over time in 0.9% wt. NaCl solution.	82

ABSTRACT

Author: Zhou, Jiawei. PhD

Institution: Purdue University

Degree Received: December 2018

Title: Ultrasonically Controlled/Powered Implantable Medical Devices.

Committee Chair: Babak Ziaie

Implantable biomedical devices have been widely used to treat a variety of diseases for many decades. If allowed by the size and form factor, batteries have been the power source of choice in implantable devices (e.g., cardiac pacemakers). Batteries are, however, still big and come in shapes that are not ideal for minimally invasive deployment. Inductive powering is another commonly used energy source in which two well-aligned coils allow a transmitter to power the implanted receiver (e.g., cochlear implants). Once the receiver coil becomes small (mm-scale), the inductive powering link becomes very inefficient and sensitive to slight misalignment between the coils. Hence, it becomes increasingly difficult to power small devices implanted deep (>5 cm) within the tissue using inductive powering. Ultrasonic powering is an attractive alternative for powering miniature devices since it can penetrate deep into the tissue, it has greater efficiency at mm-scale receiver size, it can be omni-directional, and it is more amenable to miniaturization.

In this dissertation, I describe the use of ultrasonic waves to power and control mm-scale implantable devices. After a detailed look at ultrasonic transmission link, I will discuss factors affecting the power transfer efficiency. These include the effect of receiver aspect ratio and size on the resonant frequency and factors related to acoustic and electrical matching. A 3D printed acoustic matching layer is then described. I will discuss two applications using ultrasound to power and control implantable devices. The first is a low-power on-off acoustic control scheme to reduce the standby power consumption in implantable devices. The second is an ultrasonically powered electrolytic ablator with an on-board micro-light-source for the treatment of cancer.

1. INTRODUCTION

1.1 Motivation and Background

Implantable medical devices (IMDs) that requires the involvement of surgical procedures have been intensively investigated since late 1950s. Based on its definition, an implant is such device that is invented to replace or assist any function of missing or damaged biological structure. Since first reported electrical heart stimulator by P. Zoll in 1952 [1], various implants are utilized in applications such as orthopedics, pacemakers, cardiovascular stents, defibrillators, neural prosthetics, drug delivery system, and physiological sensors [2]–[10]. The development of first pacemaker is an important and intriguing example. In this device, two 60 mAh nickel-cadmium batteries are used to power a first-generation silicon integrated circuit with a size of 55 mm in diameter by 16 mm in height [11]. More recently, with the development of transistor which was commercialized by Texas Instruments Inc. in 1954, and miniaturization of silicon based integrated electronics using planer process, implantable devices are made in small form factor, which broadens the application to real-time vitals monitoring in smaller organs. For instance, EndoSure[®] blood pressure sensor from CardioMEMS is inserted into aorta to detect any possible intraoperative leaks of the stent graft.

With the increasing demand of active implantable medical devices (powered by on-board battery or other power supply in other forms), the mismatch of the service life of the power source and the longevity required by the patients come into focus. As reported, an average required lifetime of implanted cardiac defibrillators (ICDs) can be nearly 10 years. Whereas the service life for most ICDs is only 4.7 years [12]. After the service period of implanted device, patients will have to suffer from the surgical intervention which increases the risk of being infected as well as the economic burden for patients. As a fact, in most cases, the main factor which limits the service time of implantable devices is the longevity of the power source. The power consumption for different devices are different and can be generally summarized in Table 1.1 [12] [13]. As listed, the electrical power requirement for such implant that requires a continuous power supply fall into a range of micro to milliwatt. Thus, for example, if a device is powered by a 3V 120 mAh battery, if it consumes an electrical power of 50 μ W, the longevity of this device is calculated to be 300

days which is less a year. Therefore, one can expect that it is critical to design an appropriate power source and a controllable power management unit for different applications.

Table 1.1 Electrical power consumption for different applications [12] [13]

Implantable device	Typical power requirement
Pacemaker	30-100 μ W
Cardiac defibrillator	30-100 μ W
Neurological stimulator	30 μ W to several mW
Drug pump	100 μ W to 2 mW
Cochlear implants	10 mW

For over decades, batteries have become the most popular energy sources for implantable medical devices. The invention of lithium-metal batteries in the early 1970s [14] opened up the possibility of powering implantable cardiac pacemakers and other active devices such as implantable cardioverter defibrillators (ICDs) and deep brain stimulators (DBSs) for many years without replacing the battery. The first pacemaker which is powered by lithium cell was invented by Antonioli G. in 1973 which soon replaces zinc/mercuric oxide batteries as the major power source for implantable devices. After the introduction of the first design, various lithium chemical batteries have been developed, such as Li/I₂, LiMnO₂, and LiSO₂ [12]. These batteries can supply μ A (lithium/iodine) to mA (lithium/manganese oxide) level currents in small form factors [15]. Recently, a notable breakthrough has been brought up by Medtronic with the commercialization of lead-less pacemakers (Micra[®], 0.8 cc total capsule size with an embedded lithium-hybrid CFx silver vanadium oxide battery) having cylindrical-shaped miniature batteries that can last for up to 12 years [16]. Another example of current implantable sensing system is Medtronic Reveal[®] insertable cardiac monitoring system, which can continuously monitor heart rhythms for up to 3 years [17].

As an attractive alternative, wireless powering or inductive coupling link technology is proposed for those power-hungry devices (e.g. cochlear implants), which will quickly drain the power of battery. Such magnetic coupling resembles the recognition of radio frequency identification (RFID)

[18]. Most inductive powering design uses a frequency lower than 20 MHz in order to avoid tissue heating by the absorption of RF power [19]. For inductive powering, low power RF signal is radiated and picked up by reader coil antenna to provide a stable sinusoidal wave. The transmitted signal is normally stable and can be easily converted to DC voltage to power the implanted electronics. For example, Figure 1.1 illustrates the deployment of an inductively powered left ventricular assist device (LVAD) [20]. As shown, a coupling system consists of two coils with one pick-up coil located inside body and the other primary coil outside the body. To maintain the transferring efficiency, two coils are well designed to have the same resonant frequency. The primary circuitry system or the transmitter is tuned to oscillate at a low load impedance for driving the transmitter coil. Conventional inductive powering normally requires a good alignment between primary and secondary coils and suffers from a drastic loss of powering efficiency when transmission depth increases [21].

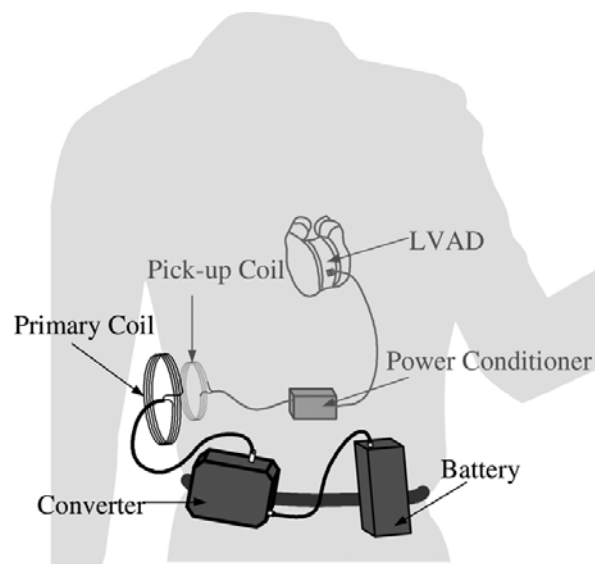


Figure 1.1 A high power closely coupled wireless powering system [20]

Other than cardiac pacemakers or monitoring devices that need to operate on continuously, many emerging implantable diagnostic systems need to function intermittently. For instance, a bladder pressure sensor can wake up several times a day, and sense and transmit measured physiological parameters, and then switch back into a sleep-mode to conserve power. Such systems are

sometimes implanted deep inside body which is not suitable for inductive powering and mostly powered using on-board batteries. Therefore, the desirable approach to save the energy for such systems is to be able to wirelessly turn the system on-off. Although low-power circuit design is widely available with many manufacturers, TI for example, standby (sleep mode) power consumption in such systems is still high, impeding their application in long-term implants. For example, a low-power wireless micro manometer is introduced by S. Majerus [10]. An ASIC power-control unit is proposed to regulate the power consumption of the implant. While operating, the average current consumption is 8.6 μA . A recent work reported by our group using a CC1110F32 RF System-on-Chip (Texas Instrument, USA) module for an implantable bladder pressure sensor, consumes 1.5 μA (3V power supply) in the sleep mode. By employing a CR2032 (3V, 225mAh, Panasonic, Japan) battery, the implanted system can be powered for 5.6 years in an hourly transmitting manner [22]. To reduce the standby power consumption further, an independent power management circuitry is needed. For example, a discrete-component bi-stable low-power radio-frequency triggered switch has been introduced which consumes 25 nA (1.35V) in the off-state [23]. Another integrated RF wireless battery power management circuit has also been developed by H. Allen [24]. A continuously operated RF detector (300nW, 2.7V, standby power consumption) is implemented to activate a ring-oscillator which determines the on-time of the controlled system. Once triggered by signal at certain frequency, the controlled system is turned on. However, in abovementioned cases, a RF switch which is always in a standby mode consumes power in an order of nano to microwatt due to the functionality and complexity of the RF circuit.

As one solution to the aforementioned challenges, we present a remote powering link technology via ultrasonic wave has several advantages over traditional methods. Compared to inductive powering, ultrasonic wave can penetrate deeper (>10 cm) into the body. Not like inductive powering which requires a secondary coil in large size, mm or sub-mm piezo element is adequate for providing a voltage in several volts. Additionally, because of the reflection of sonic wave inside body, ultrasonic powering is less sensitive to the misalignment or the position of implant [21]. Recently, several ultrasonic powered devices have been developed for different applications. For example, a miniature ultrasonic powered nerve cuff stimulator is presented by P. Larson [25]. The device is 8 mm long and capable of generating a current more than 1 mA. Another device is an implantable micro oxygen generator (IMOG) which is designed by our group [26]. The IMOG

mainly consists of a piezoelectric element (lead zirconate titanate, PZT), a rectifying circuit and an ion exchange membrane to prevent the generation of chlorine. The implant ($2 \times 2 \times 8 \text{ mm}^3$) can generate 0.816 mW of electrical power, resulting in 0.525 $\mu\text{L}/\text{min}$ oxygen generation. Moreover, ultrasonic wave can also be used as a substitution to RF control to switch on and off the system which offers low standby power consumption, smaller form factor of the receiver, and design simplicity.

1.2 Organization of the Dissertation

The thesis focuses both on the optimization and application of ultrasonic coupling technology. In the following chapters, an ultrasound powering model will be discussed with device powered/controlled by ultrasound. In the Chapter 2, the basic theory behind ultrasonic powering is explained which includes: the basic idea of wireless powering, converting principles of piezo-materials, standard equivalent circuit and some characterization results. In Chapter 3, acoustic impedance matching and frequency matching will be both discussed with several experiments for optimization. Three different ultrasonic powered or controlled devices are presented in 1) Chapter 4, an ultrasonically controlled power management system/switch to save energy in battery-powered systems; 2) Chapter 5, an ultrasonically-powered micro-light source for localized photodynamic therapy; and 3) Chapter 6, an implantable device for combined photodynamic and electrolytic tumor ablation.

2. ULTRASOUND GENERATION AND COUPLING

2.1 Introduction

Wireless powering and communication technology has become one of the emerging technologies which contribute to the prosperity of implantable devices [27]–[29]. Many different power transfer methods are developed by people which featured with various advantages and disadvantages. In this chapter, several main wireless power transfer methods will firstly be described, either electrical or mechanical. In the following sections, ultrasonic powering will be introduced as one possible method to some of the unsolved challenges. The properties of piezoelectric material are discussed followed by a section about the equivalent transmission model of ultrasound powering. In the last two sections, the powering efficiency and transmission pattern of ultrasonic powering are characterized and discussed.

2.1.1 Inductive Powering

Inductive powering or inductive energy harvesting has become one of the most attractive powering technologies for short range wireless power transfer. Like other RF communication technology, the antenna coil radiates a low-power RF signal which is often designed to offer a fixed-frequency carrier sinusoidal wave. Because of the stability of the RF signal while transmitting through the human body. Figure 2.1 illustrates a schematic of inductive powering system via electro-magnetic field [30]. The powering transfer system consists of two coils. A primary coil is attached onto the body from the outside while the receiving coil implanted inside the body. Two coils usually share a common resonant frequency. In practice, the number of turns can be added until specified inductance is reached. Theoretically, the resonant frequency of primary and secondary coils can be calculated using Equation 2.1 [31]:

$$f_0 = \frac{1}{2\pi\sqrt{LC}} \quad (2.1)$$

where L is the inductance of coils and C is, the capacitor connected in the resonant circuit. While other parameters are considered, such as mutual inductance (M), which determine the powering efficiency (K) by Equation 2.2:

$$K = \frac{M}{\sqrt{L_1 L_2}} \quad (2.2)$$

where L_1 and L_2 are the inductance of transmitting and receiving coils respectively.

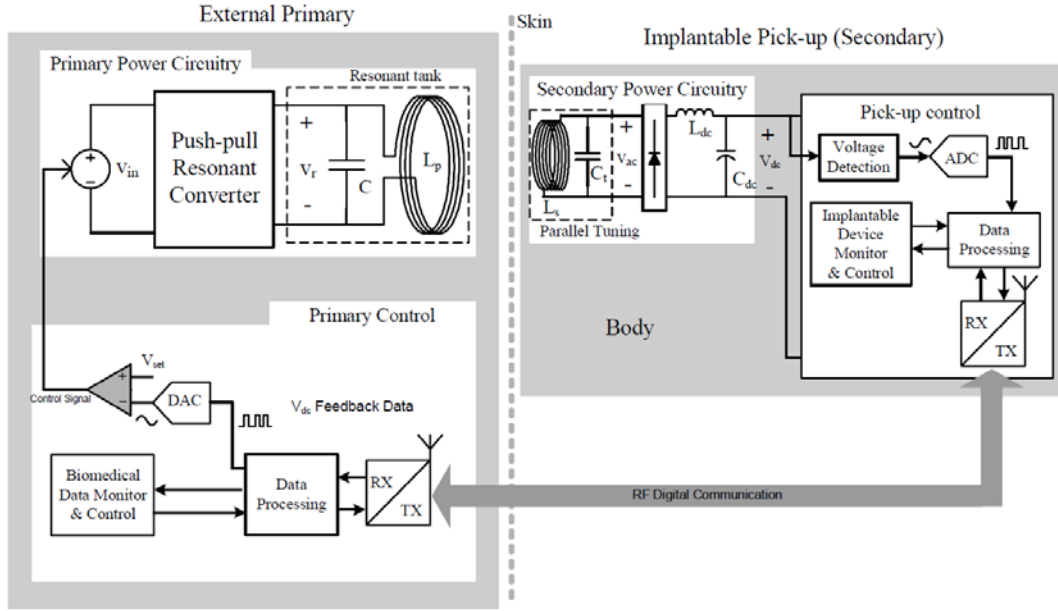


Figure 2.1 Wireless powering system with magnitude control from external primary side [30]

2.1.2 Capacitive Powering

Similar to inductive powering and data transfer, capacitive powering or coupling link is also used in the case of short-range wireless communication. In such system, two parallel aligned conductive plates are acting as a plate capacitor. The first plate is attached to the body from outside while the second plate is implanted inside the body. Such method can be used both for transmitting power and data [32]. The simplified circuit model of capacitive powering system is revealed in Figure 2.2 [31]. As shown, V_{in} is the input voltage. Two capacitors, C_1 and C_2 , are the major pads for energy transfer. Thus, a voltage transfer efficiency over a load resistance can be given by Equation 2.3:

$$\frac{V_{out}}{V_{in}} = \left(\frac{R_L^2}{R_L^2 + X_{Ceq}^2} \right) \quad (2.3)$$

where C_{eq} is the sum of C_1 and C_2 . Thus, the V_{out} is increased to maximum when X_{Ceq} is much smaller than the load resistance.

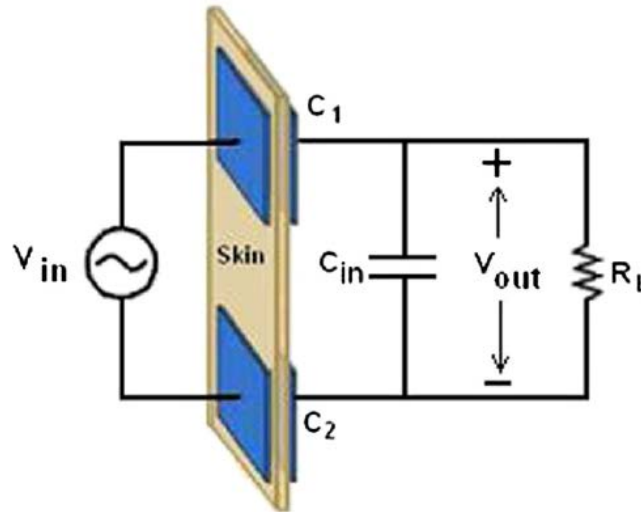


Figure 2.2 The simplified capacitive coupling link equivalent circuit [31]

The disadvantage of such coupling technology is also obvious and arises some concerns. The implanted plates may significantly increase the temperature of surrounding tissues. Moreover, due to the non-magnetic property of human body, the electric field will be absorbed by the body.

2.1.3 Optical Wireless Powering

Some optical methods have also been developed to recharge the on-board battery [33], [34]. In this design, a rechargeable lithium battery is connected with a series of photodiodes. Near-infrared (NIR) light is adopted for a better transmission through the tissue. As claimed, at a light intensity of 22 mW/cm^2 with 17 min of irradiation, the stored energy is $480 \mu\text{Ah}$ which is enough for a cardiac pacemaker to operate for 24 hours [34]. *Ex vivo* studies also suggested that a large lighting area can significantly reduce the heat generation by NIR irradiation.

However, such technology still suffers from the intrinsic converting efficiency of semiconductor photocells. Due to the transmission depth of NIR light, such system is not operational for deeply seated implantable devices. Due to the low power generation from light, the need of electricity storage, e.g. a capacitor or battery, increases the overall size of the implant which also impedes the application of optical recharging system.

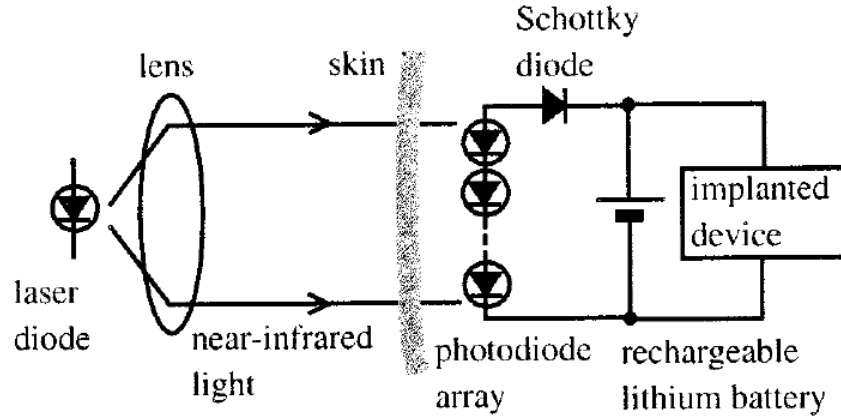


Figure 2.3 The schematic of near-infrared laser enabled wireless recharging system [33]

2.1.4 Ultrasonic Coupling

Besides three aforementioned power coupling technologies, ultrasonic powering is a modern technology aimed for deeper power transfer for implantable devices. The method offers several advantages over inductive powering such as less electronic interference with other electromagnetic devices [35], omni-directional transmission [36] and deeper penetration depth [21]. In 2004, an ultrasonic powered neuro stimulator which provides a current in milliamperes level was developed by Phillips *et al* [37]. Figure 2.3 shows a general schematic for ultrasonic powering system [33]. The ultrasonic wave is generated by a transducer on the skin which converts the electrical AC input into mechanical vibration. Most, piezoelectric materials are used as transducer. On the other side, inside body, another piezoelectric element receives the ultrasound and converts it back to electrical power. In 2010, Zhu *et al.* designed a biosensor which is powered by ultrasonic wave at 21.4 nW [38]. In this work, a MEMS resonator is used to energy conversion for its small size. In another work by our group, a micro implantable oxygen generator is developed using a mm-scale PZT cuboid as receiver which can generate power in a level of milliwatts [26]. In 2015, a ultrasonically powered implantable light source (μ Light) was also introduced by our group to generate light intratumorally for photo-dynamic therapy [39]. On-board LEDs were integrated with PZT to convert acoustic vibration in deep tumors.

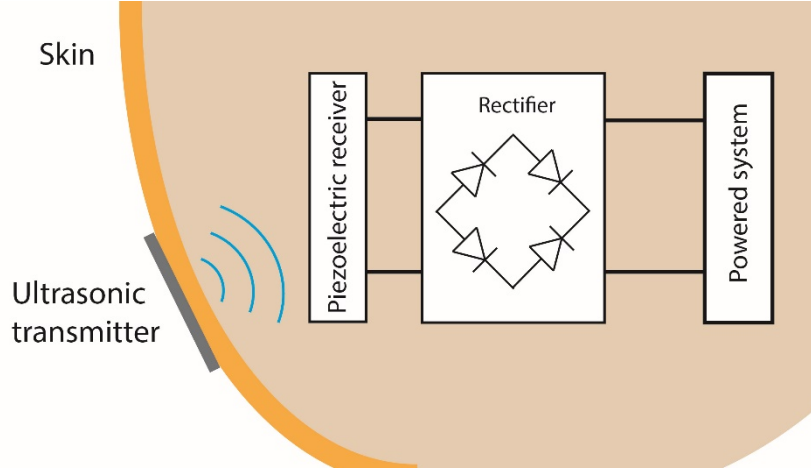


Figure 2.4 Schematic of ultrasonic powering system for implantable devices.

2.2 Piezoelectricity and Piezo-Materials

Piezoelectricity is a phenomenon which describes a correlation between applied force and induced electric charges or the applied voltages and generated deformation. With these basic phenomenon, piezoelectric materials are always used for energy conversion and physical sensing.

The first correlation is called the direct piezoelectric effect that explain the case when a mechanical force or strain is applied to the material, some electrical charges and voltage are generated across the surfaces of material. Conversely, if an electric voltage is applied to a piece of piezoelectric material, a mechanical strain will be generated.

In the theory, the linear piezoelectric constitutive equations are derived [40]:

$$\begin{aligned}\mathbf{E} &= \beta^S \mathbf{D} - h \mathbf{S} \\ \mathbf{T} &= c^D \mathbf{S} - h^t \mathbf{D}\end{aligned}\quad (2.4)$$

and

$$\begin{aligned}\mathbf{D} &= \epsilon^T \mathbf{E} - d \mathbf{T} \\ \mathbf{S} &= s^E \mathbf{T} - d^t \mathbf{E}\end{aligned}\quad (2.5)$$

where \mathbf{T} , \mathbf{E} , \mathbf{S} and \mathbf{D} are the vectors of stress, electric field, strain and electric displacement (charge per unit area) respectively. c^D denotes the elastic matrix, β^S is the dielectric impermeability matrix, s^E is the elastic compliance matrix, ϵ^T represents the transpose of the dielectric matrix. In the equations, a quasi-static approximation is often assumed so that the system is not time-variant with no changes over time.

Despite the fact that there are many types of piezoelectric materials can be used as a sensor, most studies are focused on the use of two types of piezoelectric materials for biomedical powering applications, namely piezoelectric ceramics and polymeric materials.

2.2.1 Lead Zirconate Titanate (PZT)

PZT is the most commonly used piezoelectric materials for energy conversion. Other elements are often doped into PZT for a better performance. These ceramics are sintered at a temperature of 800-1000 °C by mixing lead, zirconium and titanium oxide powders to form perovskite PZT. After proper milling, the power is mixed with adhesive binder and sintered in a mold for designed shape. The poling process happens before the ceramic completely cools down. The material is placed under a high electric field to induce the paraelectric to ferroelectric phase transition. Under such electric field, most of the dipoles are aligned to be parallel to the applied field. At atoms level, the cubic lattice structure becomes tetragonal. Unlike the unpoled piezoelectric materials, the poled material has a net polarization. The material after poling shows aforementioned piezoelectric properties.

As a member of ceramic family, PZT exhibits most of the characteristics of ceramics. The material is mechanically isotropic which contributes to the omnidirectionality of ultrasonic powering.

2.2.2 Polyvinylidene Fluoride (PVDF)

PVDF is a polymeric material with a long chain of repeating monomer. The piezoelectric property is introduced by its inherent dipole moment that in each monomer. Positively charged hydrogen atoms and negatively charged fluorine atoms induce the electric charges. The fabrication of PVDF film starts with the solidification of the melted polymer, followed by stretching and poling along certain direction. After cooling and molding, the polymer chains can be aligned by stretching. Thus, polarized dipole moment can be found in the film which contributes to its piezoelectric characteristics. Due to its fabrication process, the material is only considered to be mechanically isotropic under small strains. The Young's modulus of PVDF is relatively low and approximately 1/12 that of aluminum [41]. It is therefore much more suitable for flexible design. It is important to mention that, however, PVDF is pyroelectric, and this high dependence on temperature affects the performance of sensing as compared to PZT sensors.

2.2.3 New Materials

Other than the aforementioned PZT and PVDF, other new piezoelectric materials have been found and systemized by researchers [42]. A piezoelectric ceramic with microstructure texture has been investigated and experimentally prepared by Jeong et al. using tape-cast SrTiO₃ (STO). They concluded that samples with addition of STO showed an excellent piezoelectric coefficient over the STO-free sample [43]. Elfrink et al. analyzed aluminum nitride (AlN) as a piezoelectric energy harvesting material. As reported, a output power of 60 μ W was monitored at an acceleration of 2.0 G [44]. A stacked piezocomposite structure of carbon/epoxy layers, PZT ceramic and glass/epoxy has also been studied by Tien and Goo [45]. As a promising biocompatible piezoelectric material, BaTiO₃ is also compared by people with other biocompatible materials for implantable ultrasonic transducers [46]. Its coupling coefficient is about 60% of PZT and currently commercially available.

2.3 Output Voltage and Omnidirectionality of Acoustic Powering

With known coupling coefficient, the output voltage along poling direction can be derived from input acoustic pressure.

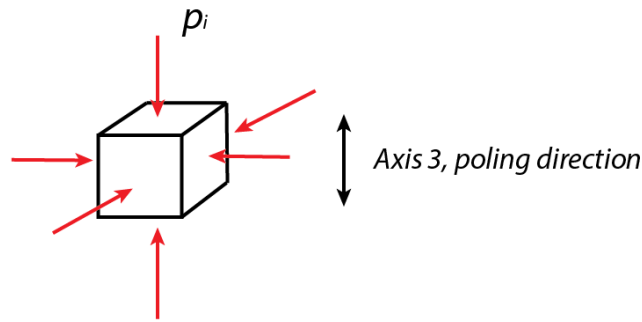


Figure 2.5 Input acoustic waves induce charge generation along poling direction.

As shown in the Figure 2.5, assume a cubic piezoelectric element, when being submerged in acoustic field, incoming waves squeeze the material from 6 facets. Generated charge density σ_3 can be quantified as:

$$\sigma_3 = \sum_{i=1}^6 d_{3i} p_i \quad (2.6)$$

where d_{3i} is the coupling coefficient corresponding to poling direction and p_i denotes the input acoustic pressure. Therefore, the electric field across the dielectric material is given by:

$$E_3 = \frac{\sigma_3}{\varepsilon_{33}} \quad (2.7)$$

where ε_{33} is the permittivity. By taking the integral along the axis 3, induced voltage is:

$$V_3 = \int E_3 dt \quad (2.8)$$

where t is the thickness along the axis 3. Since electrodes are often plated on the top and bottom surface, this element can be modeled as a parallel plate capacitor with store energy given by:

$$U_E = \frac{1}{2} CV_3^2 = \frac{1}{2} \frac{A\varepsilon_{33}}{t} \left(t \times \frac{\sum_{i=1}^6 d_{3i} p_i}{\varepsilon_{33}} \right)^2 = \frac{1}{2} \times \frac{At}{\varepsilon_{33}} \times \left(\sum_{i=1}^6 d_{3i} p_i \right)^2 \quad (2.9)$$

where A is the surface area. The equivalent mechanical to electrical conversion ratio is then defined as generated potential difference over total received acoustic pressure:

$$\Phi = \frac{V_3}{\sum_{i=1}^6 p_i} \quad (2.10)$$

As we derived, the generated energy stored in piezoelectric material is proportional to the surface area, thickness and acoustic input power. Due to the isotropic mechanical property of the material, acoustic input on different surface can all contribute to the net charges. By deploying device in the transmission media, omni-directionality can be observed with reflection from various boundaries (air/soft tissue, hard tissue/soft tissue), as shown in Figure 2.6 [36].

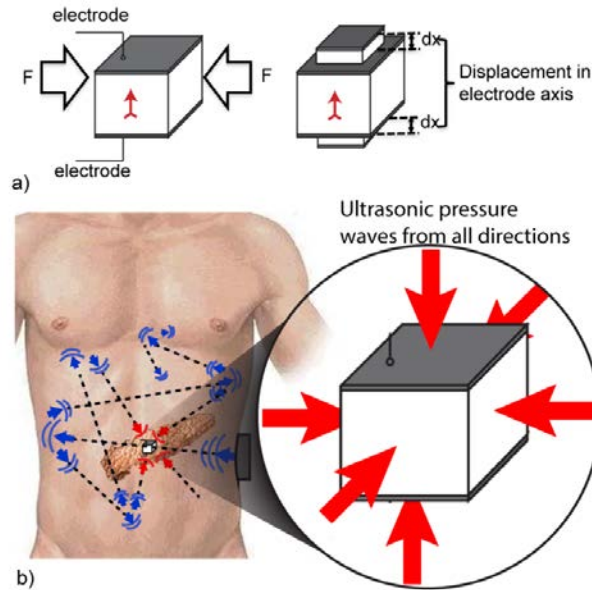


Figure 2.6 Illustration for omni-directional powering using ultrasonic wave [36]

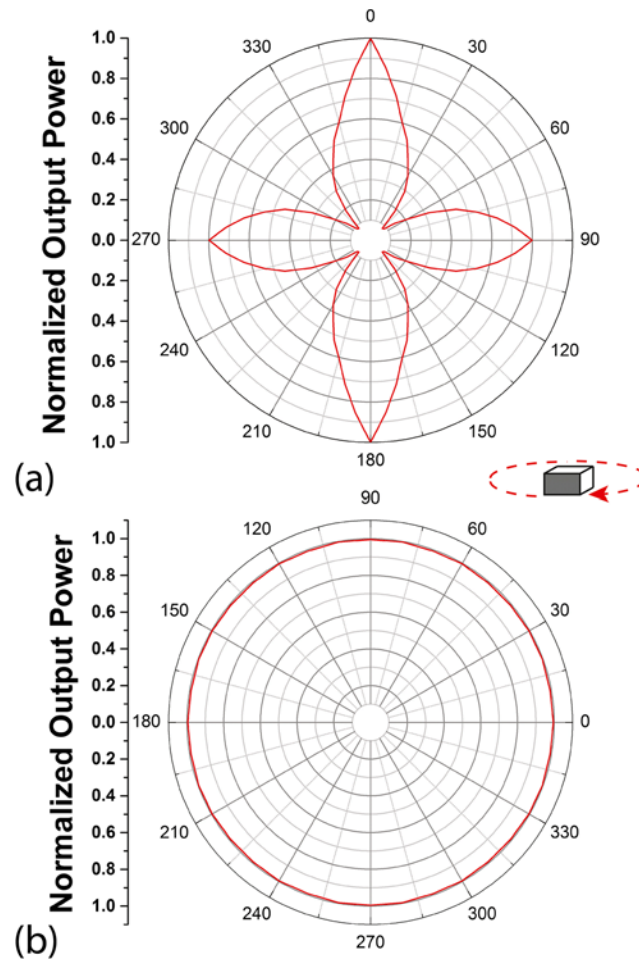


Figure 2.7 Normalized power output at various axial angular misalignments, a power output versus axial angle misalignment for PZT receivers in water tank with suppressed acoustic reflection; b power output versus axial angle misalignment for PZT receivers in water tank with wall reflection [47]

In some previous work done in our group, output power was measured with and without reflection [47]. In the condition shown in Figure 2.7(a), absorption layer was attached on the sidewall of water tank during the measurement. A decreased output power was detected at different angles while rotating along axis perpendicular to poling direction. However, once absorption layer was removed, the output power was maintained at different angles which implies the omnidirectionality of ultrasonic powering under a reflective boundary condition. In a situation of such device being implanted in soft tissue, reflection is expected which provide an ideal scenario for wireless powering.

2.4 Transmission Model and Equivalent Circuit

Ultrasonic coupling system consists of a pair of transducers acting as transmitter and receiver. Fig. 2. shows the equivalent circuit for piezoelectric transmission model developed by Krimholtz, Leedom and Mattaei (KLM model) [48]. In this model, the whole system is divided into three different sections, namely, the transmitter, tissue, and the receiver. Transmitter includes the external transducer and attached matching layers. An AC signal (V_{in}) is usually created for the piezoelectric transducer to vibrate at a frequency (> 20 kHz). The transducer undergoes a vibration mode called thickness-expansion mode. C_t and C_r are the equivalent capacitance of piezoelectric material while X_t and X_r represent frequency dependent impedances that vanish at the resonant frequency of the elements. The electromechanical coupling is modelled as a transformer ($1:\Phi$), as derived in the previous chapter. The mass on the two faces of piezoelectric plate and intermedia are modeled as transmission lines with certain impedances (Z_t , Z_s). Lastly, the received electrical signal is represented as V_L .

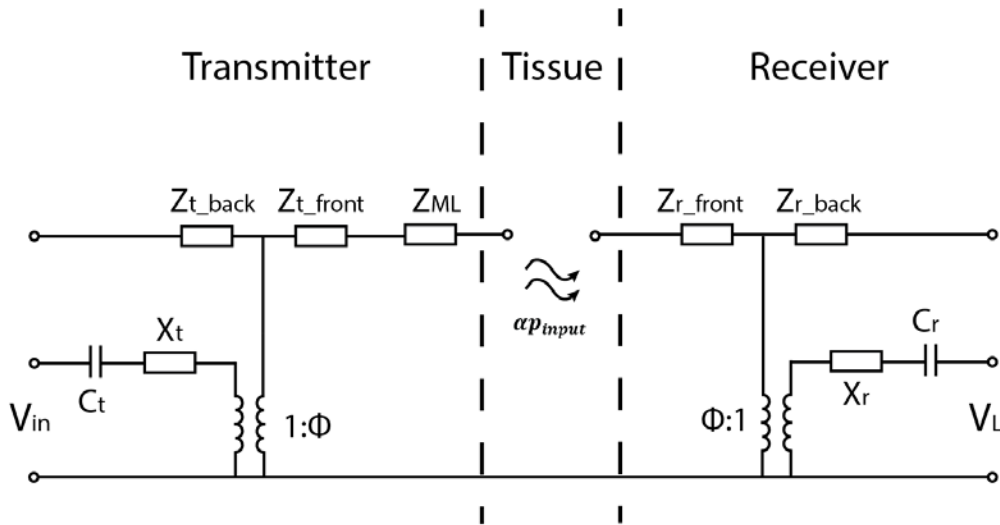


Figure 2.8 Schematic of the KLM model for the ultrasonic communication link.

To increase the transmission efficiency, the operational frequency is often set to the resonance of piezo-elements (X_r becomes zero at resonance). To simplify the equivalent circuit, the receiver is modeled as a voltage source which transform the voltage at a ratio of Φ . C_r represents the parallel capacitance in the material. Table 2.1 summarizes some properties of PZT-5A material used in our

system. For the thickness-expansion mode, the resonant frequency (f_r) is usually defined by its thickness t and frequency of the sound wave in the material, given by:

$$f_r = \frac{v_D}{2 \times t} \quad (2.11)$$

where v_D is the traveling velocity in the piezoelectric material. This quick estimation is more applicable to a case of piezoelectric disk with a width to thickness ratio larger than 10. In a shape close to cube, which is common in most implantable devices, the resonant frequency changes because of the materials Poisson's ratio and other edge mode coupling [49].

Table 2.1 Mechanical properties of PZT-5A

ρ (kg/m^3)	7800
c_{33}^D (N/m^2)	5.2×10^{10}
ϵ_{33}^S	1800
d_{33} (pC/N)	390×10^{-12}
g_{33} ($mV \cdot m/N$)	24×10^{-3}

In order to calculate the transferred power, we firstly introduce the acoustic impedance of the piezoelectric material which is given by [36]:

$$Z_0 = \sqrt{\rho c_{33}^D} \quad (2.12)$$

where ρ is the density and c_{33}^D is the open circuit complex elastic stiffness of the material. At transducer side, the conversion of input electrical power to mechanical output can be represented by (1:Φ):

$$\Phi = \frac{1}{2 \left(\frac{h_{33}}{\omega Z_0} \right)} \csc\left(\frac{\beta t}{2}\right) \quad (2.13)$$

where β is the wave number given by ($\beta = 2\pi/\lambda$) and h_{33} is the piezoelectric pressure constant:

$$\Phi = k_t \sqrt{\frac{c_{33}^D}{\epsilon_{33}^S \cdot \epsilon_0}} \quad (2.14)$$

where k_t is the electromechanical coupling coefficient which greatly determine the converting efficiency of one piezoelectric material and ϵ_{33}^S is the clamped relative complex permittivity.

When the piezoelectric material operates at its resonance, X_r vanishes and the voltage output of the transducer at receiver end can be expressed as:

$$V_L = p_{input} \alpha \cdot T \cdot \Phi \cdot \frac{Z_L}{Z_{eq} + Z_L} \quad (2.15)$$

where p_{input} is the input acoustic pressure, T is the acoustic matching transmission (%). α is the attenuation through the tissue which is modeled as:

$$\alpha = e^{-2\mu x} \quad (2.16)$$

with μ as attenuation coefficient and x being the penetration depth.

$$\eta = \left| \frac{p_{out}}{p_{in}} \right| = \Phi_T \Phi_R \alpha T \quad (2.17)$$

where Φ_T and Φ_R are the transmitter and receiver conversion efficiency respectively.

2.5 The Acoustic Field in Near-Field Region

Since a rectangular disk-shape PZT source was used for most of our experiments, we start from discussing the transmission field for circular disk source in this section.

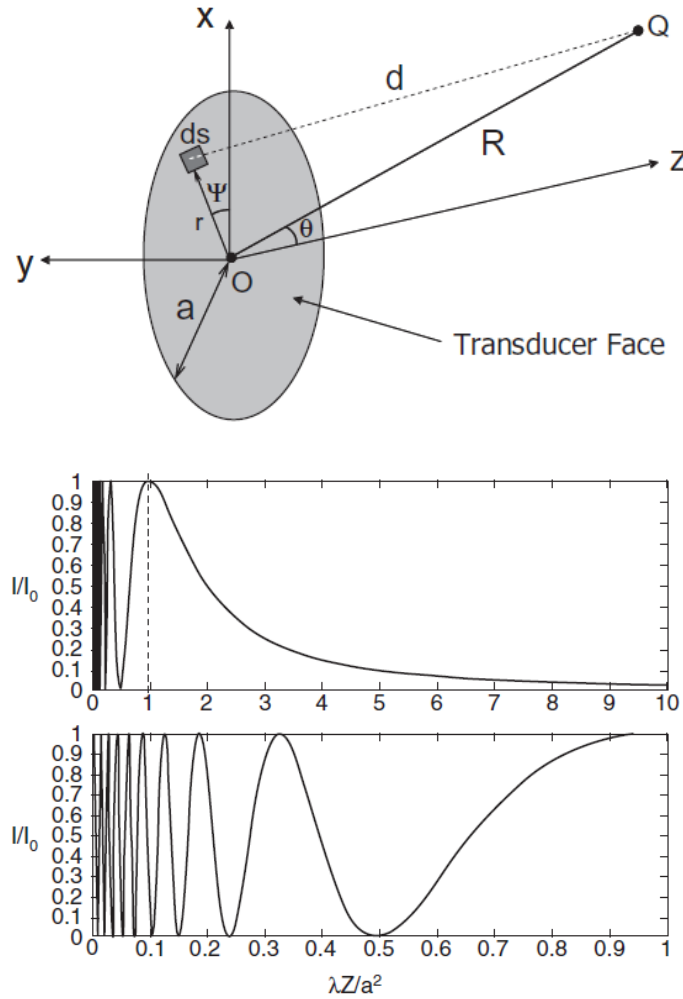


Figure 2.9 Near-field boundary calculation of a circular transducer [50]

By taking the integral of acoustic intensity along center axis, the accumulated intensity on z axis can be expressed as [50]:

$$\frac{I}{I_0} = \sin^2 \left[\frac{\pi}{\lambda} \{ (a^2 + z^2)^{1/2} - z \} \right] \quad (2.18)$$

where I and I_0 are the acoustic intensity at z (distance along central axis) and original generated acoustic intensity respectively. λ is the wavelength of sound wave and a is the radius of the transducer. As expected, several maxima and minima will appear with the location of maxima is given by:

$$z_{max} = \frac{4a^2 - \lambda^2(2m+1)^2}{4\lambda(2m+1)} \quad m = 0, 1, 2, \dots \quad (2.19)$$

and location of minima is given by:

$$z_{min} = \frac{a^2 - \lambda^2 n^2}{2n\lambda} \quad n = 1, 2, 3 \dots \quad (2.20)$$

Thus, close to the maxima and minima points, the acoustic intensity changes rapidly and such field is not feasible for ultrasonic imaging, Figure 2.9 [50]. When m is equal to zero and if the source diameter is much larger than the wavelength, the last maximum point is approximately equal to:

$$Z_{NF} = \frac{a^2}{\lambda} \quad (2.21)$$

This Z_{NF} is then defined as near-field boundary/limit. For a case of water transducer with a radius of 3.5 cm width, at 1.15 MHz frequency, the near-field limit is calculated to be around 0.97m.

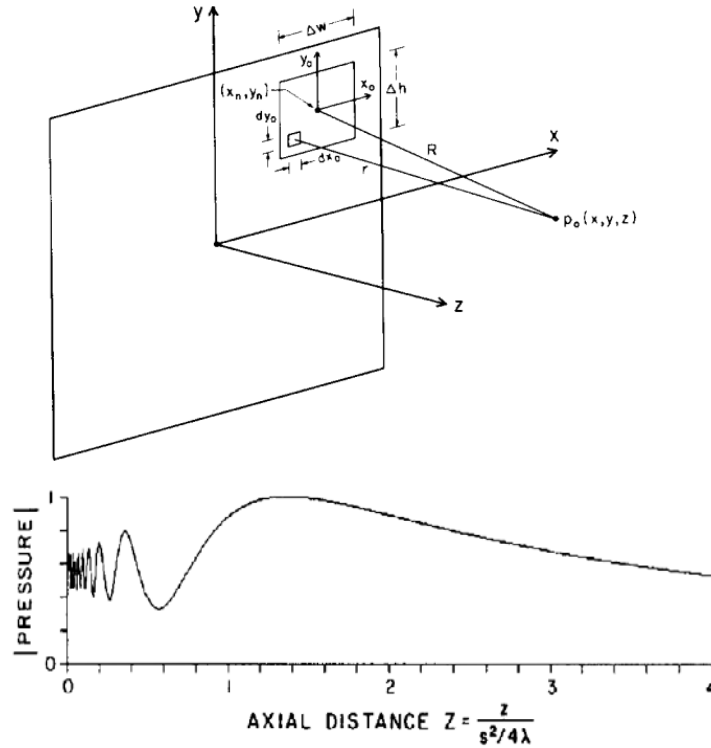


Figure 2.10 Near-field boundary calculation of a rectangular transducer [51]

Another study suggests the transmission pattern of a rectangular transducer is very similar. The near-field boundary is slightly larger than Z_{NF} when the size of the transducer is much larger than the width of the transducer. However, the acoustic intensity didn't reach zero at minimum point and oscillates between $0.3I_0$ and I_0 instead, as shown in the Figure 2.10 [51]. An average intensity of around $0.5I_0$ can be achieved within near-field when there is no reflection. More specifically, the intensity is overall high and varies fast within $0.1Z_{NF}$.

In a more realistic scenario, the acoustic intensity in this region can be changed by echo because of the discontinuities of medium, especially at the boundary of tissues. However, for powering purpose, operation within the near field range generates an overall higher voltage. Therefore, to understand the powering mechanism better, relative powering efficiency is then measured in the near-field region.

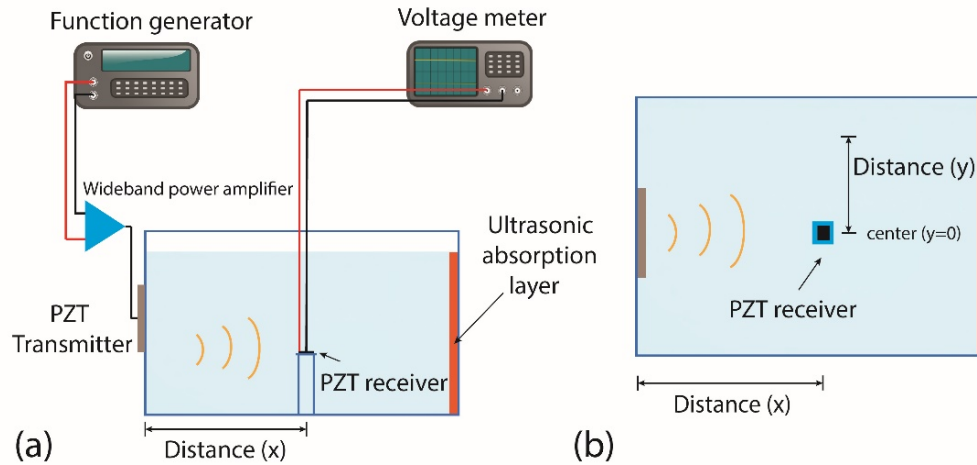


Figure 2.11 Non-reflective condition transmission measurement: (a) side view; (b) top view.

The non-reflective transmission pattern is measured using the setup as shown in Figure 2.10. In such measurement, water is mostly selected as media for its similarity of the acoustic properties to that of the soft tissue. A function generator (33220A, Agilent) is connected to a wideband power amplifier (ENI A300, Electronics & Innovation, Ltd. NY, USA) to create AC electrical signal to drive a PZT transducer which is embedded on the water tank. For avoiding possible electrical noise coupled by connections, at the receiver, generated AC signal is firstly rectified by a rectifying circuit integrated with the PZT element in the water tank. The output of the rectifier in the circuit was connected to a voltage meter for measuring. Figure 2.12 is the water tank being used for the non-reflective measurement. The hydrophone was attached to an adjustable beam which enables the automatic control of measuring distance. The acoustic pressure was evaluated with a fiber optics hydrophone. Rubber absorption layer was fixed on the sidewall to remove the echoes. Hydrophone was placed with tip pointing to the PZT transducer in order to catch the change of acoustic intensity in the coming direction.

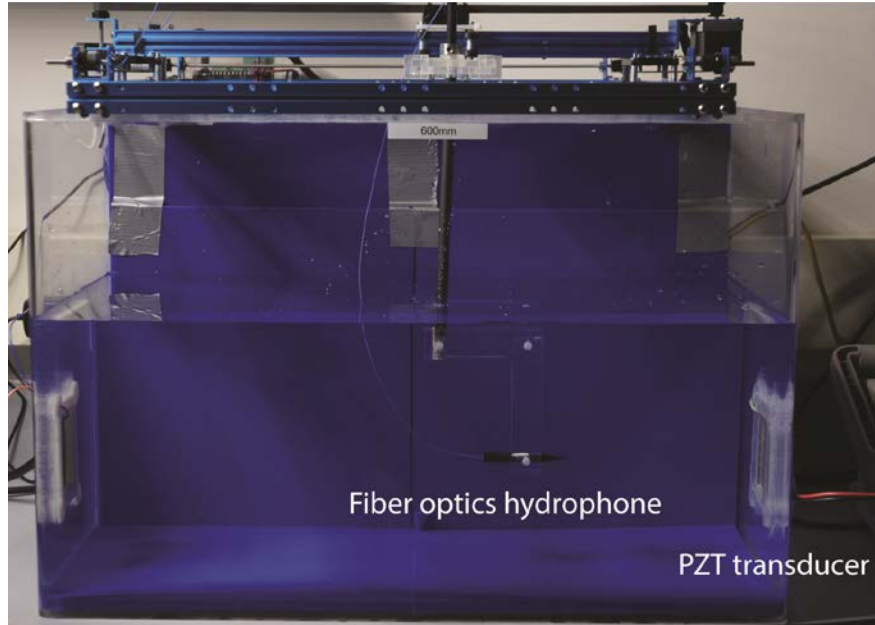


Figure 2.12 Picture of water tank setup used for acoustic transmission measurement.

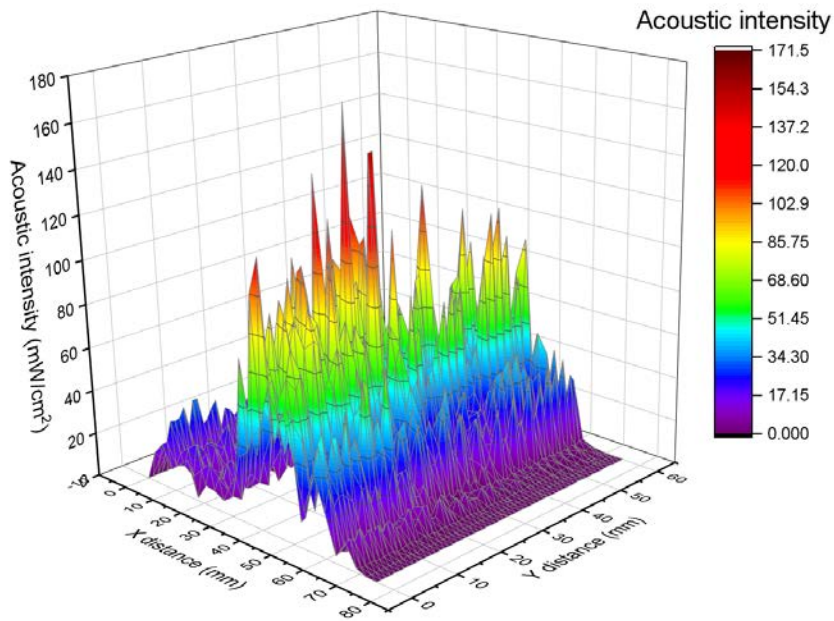


Figure 2.13 Measured acoustic intensity at various locations away from the transducer.

As shown in Figure 2.13, acoustic intensity changes rapidly within the near-field range. In the aspect of visualization, the transducer was placed at the center of “x distance” which is at around 40 mm point on x axis. Along the center axis, as expected, several minima and maxima points are measured with a baseline of around 50 mW/cm^2 , as illustrated in Figure 2.14. Since the data was

measured every 1 mm, some peak values were missed, and the wavelength was around 1.3 mm. Under such circumstances, a higher resolution was required for a more accurate measurement. A lower frequency can also be used to validate the transmission pattern of ultrasound.

In addition to the change along central axis, acoustic intensity attenuates while misalignment exists between transmitter and receiver. The blue/purple region denotes a relatively low intensity which is beyond the coverage of ultrasound transducer. When x distance increases, the measured acoustic intensity decreases dramatically as reported by other groups [52].

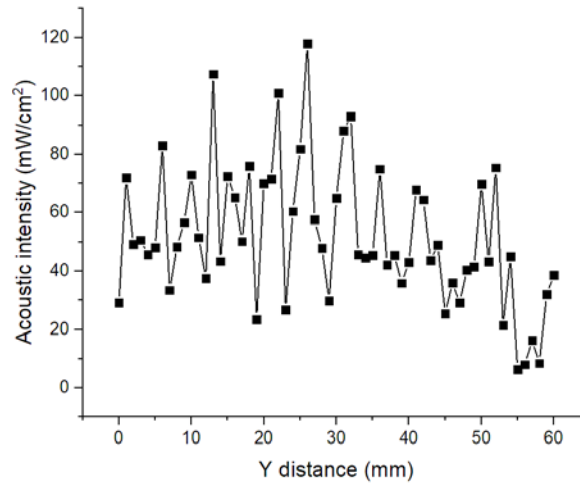


Figure 2.14 Measured acoustic intensity along central axis with distance between 0-60 mm

Thus, in a non-reflective condition, like inductive coupling, transmitter and receiver must be concentrically aligned to produce enough conversion. And according to other characterizations done by our group, the powering efficiency also decreases if poling direction is not parallel to the central axis [36].

To compare and verify the transmission pattern, 100 kHz signal was used for the same measurement. By moving the $2 \times 4 \times 2 \text{ mm}^3$ PZT sensor away from the transducer along the center axis, a change of the output voltage can be observed with a larger period of around 15 mm which is close to the theoretical value. Since a rectangular transducer was implemented, the intensity didn't drop to zero and an averaged intensity was maintained.

However, to operate the device under the FDA limit which is 720 mW/cm^2 peak value at any location with in the near-field range, a reflective condition must be measured to guarantee avoid the safety concern [53].

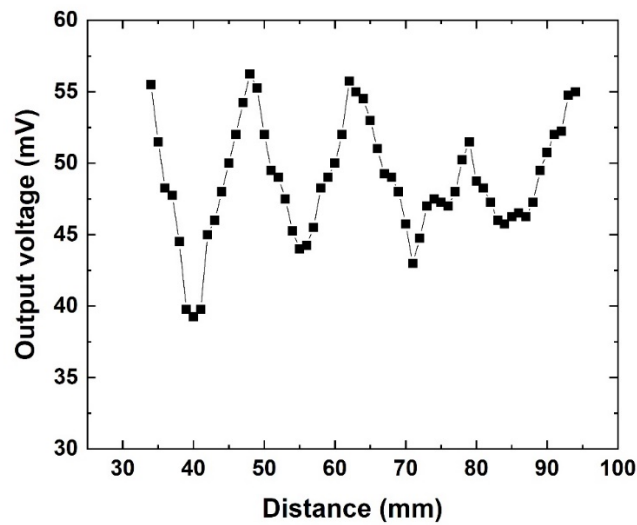


Figure 2.15 Measured output voltage along central axis with distance between 30-95 mm

An acoustic power meter was used with a setup as shown in Figure 2.16. Reflective boundary condition can be imagined as the PZT transmitter was submerged in a small water tank with around 3 cm away from the power reading surface. An averaged intensity was then measured by the transducer at the bottom. To drive the PZT, same signal generator and radio frequency amplifier was used.

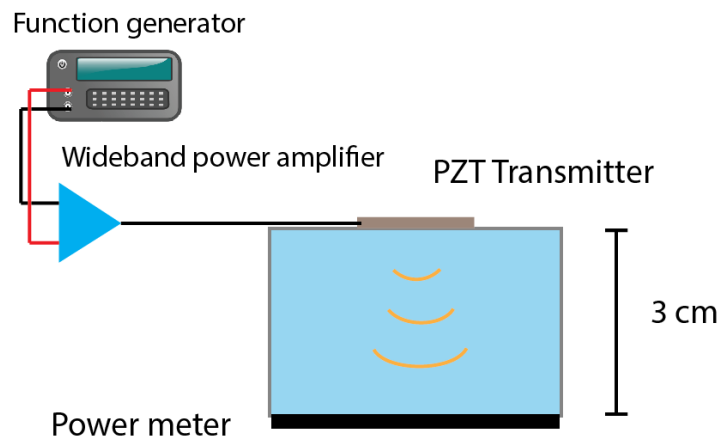


Figure 2.16 Measured acoustic intensity with reflection

The measured result was then extrapolated in Figure 2.17. As shown, the output acoustic intensity from transducer increases with an increasing input electrical voltage. The input voltage was amplified by 55dB and then connected with the PZT. To ensure the safety of operation in human body, the input peak to peak voltage from the signal generator should be kept below 180 mV which is the FDA limit.

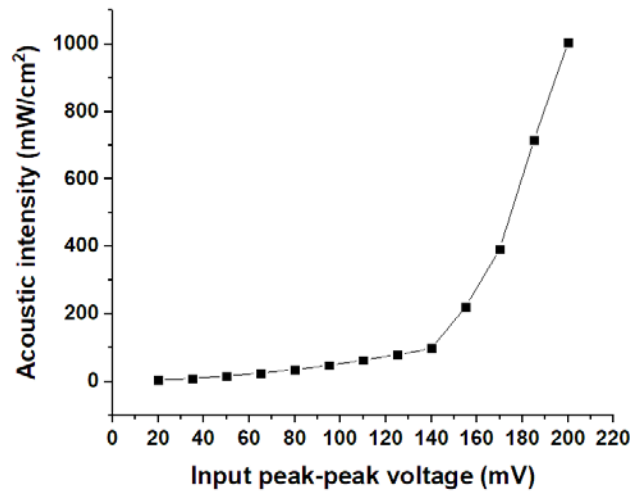


Figure 2.17 Measured output voltage along central axis with distance between 30-95 mm

3. FREQUENCY MATCHING AND ACOUSTIC MATCHING FOR TRANSDUCERS

3.1 Introduction

To maximize the powering efficiency, it is important to match both the resonant frequency of PZT and acoustic impedance of soft tissue. In this chapter, finite element analysis and direct measurement of PZT frequency response will be discussed. A theoretical model for acoustic transmission through layered structure will then be utilized to derive the material thickness for acoustic matching layer. Part of the text is taken from the publication by the author [47].

3.2 Electrical Impedance of PZT

As mentioned in the previous chapter, the thickness-expander (TE) mode resonant frequency of PZT transducer greatly depends on the dimension of PZT. When the width to thickness ratio of PZT is larger than 10, its thickness-expansion resonant frequency depends largely on the thickness, as represented in Equation 2.11. Since most of the external PZT transducers are designed with a shape of disk or plate, this conventional equation can be applied for determining the optimum operational frequency.

To verify the equation and resonant frequency of PZT plate with different thickness (1 mm and 2 mm), one method is to measure the electrical impedance of transducer. The lowest impedance point in the spectrum represents the resonance mode. For a PZT disk, the overall lowest impedance point often points the TE mode vibration as the dominant resonance.

The electrical impedance for large PZT disk with two different thickness were firstly measured using a RF network analyzer (Agilent 4396B). The measured impedance plots for 1 mm sample and 2 mm sample are shown in Figure 3.1 and Figure 3.2 respectively. In the plot, some small resonance mode (small peaks) represent the radial vibration mode and bending mode. There some other vibration modes corresponding to larger dimensions along width. As measured, the frequency of lowest impedance appears to be 2 MHz and 1.07 MHz for 1 mm and 2 mm PZT disc respectively which are close to the theoretical value (2.3 MHz for 1 mm disc and 1.15 MHz for 2 mm disc).

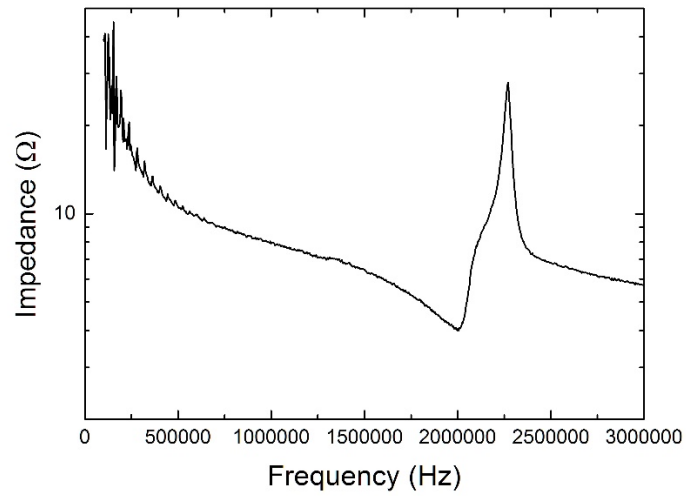


Figure 3.1 Impedance spectrum analysis of 1 mm PZT disk

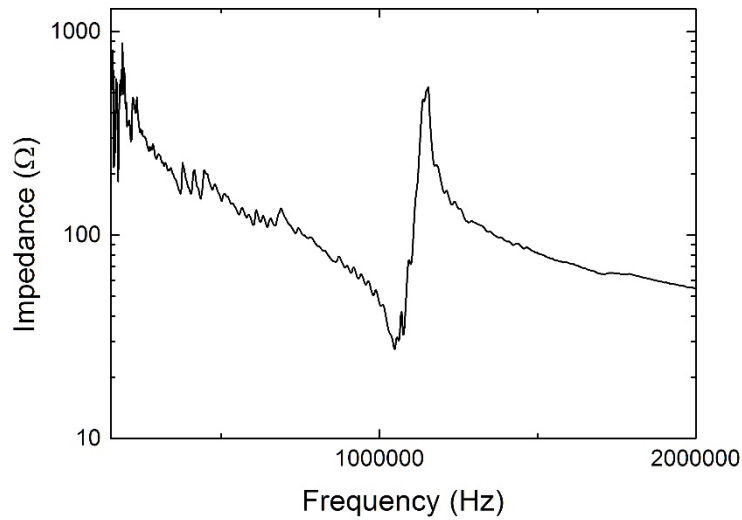


Figure 3.2 Impedance spectrum analysis of 2 mm PZT disk

In terms of piezoelectric receiver, since its dimensions are close to a cube or cuboid, the major resonant frequency is not simply thickness-dependent as it is also affected by the vibration mode along other directions and some coupling mode at the edges and corners. As a result, the resonance becomes more complicated and needs other method to derive the resonance along with the actual measurement. To simulate the electrical impedance of the material, finite element analysis tool

(COMSOL) was utilized to estimate the impedance. To model the physics, material property matrix was acquired from PZT manufacturer and entered in strain-charge form:

$$\begin{bmatrix} S_{11} & S_{12} & S_{13} & 0 & 0 & 0 \\ S_{21} & S_{22} & S_{23} & 0 & 0 & 0 \\ S_{31} & S_{32} & S_{33} & 0 & 0 & 0 \\ 0 & 0 & 0 & S_{44} & 0 & 0 \\ 0 & 0 & 0 & 0 & S_{55} & 0 \\ 0 & 0 & 0 & 0 & 0 & S_{66} \end{bmatrix}^E = \begin{bmatrix} 15.4 & -4.8 & -8.4 & 0 & 0 & 0 \\ -4.8 & 15.4 & -8.4 & 0 & 0 & 0 \\ -8.4 & -8.4 & 21.2 & 0 & 0 & 0 \\ 0 & 0 & 0 & 47.8 & 0 & 0 \\ 0 & 0 & 0 & 0 & 47.8 & 0 \\ 0 & 0 & 0 & 0 & 0 & 40.8 \end{bmatrix}^E 10^{-12} m^2/N \quad (3.1)$$

$$\begin{bmatrix} 0 & 0 & 0 & 0 & d_{15} & 0 \\ 0 & 0 & 0 & d_{24} & 0 & 0 \\ d_{31} & d_{32} & d_{33} & 0 & 0 & 0 \end{bmatrix} = \begin{bmatrix} 0 & 0 & 0 & 0 & 590 & 0 \\ 0 & 0 & 0 & 590 & 0 & 0 \\ -191 & -191 & 430 & 0 & 0 & 0 \end{bmatrix} 10^{-12} C/N \quad (3.2)$$

$$\begin{bmatrix} \epsilon_{11} & 0 & 0 \\ 0 & \epsilon_{22} & 0 \\ 0 & 0 & \epsilon_{33} \end{bmatrix}^T = \begin{bmatrix} 1780 & 0 & 0 \\ 0 & 1780 & 0 \\ 0 & 0 & 1950 \end{bmatrix}^T \quad (3.3)$$

where (3.1) is the elastic compliance matrix; (3.2) is the piezoelectric coupling coefficient and (3.3) represents the free dielectric constant. Solid mechanics and electrostatics model were used to simulate the multi-physics. In the model, boundary condition was set to free movement, a voltage was being applied along the poling direction of PZT. The impedance was then simulated as the result.

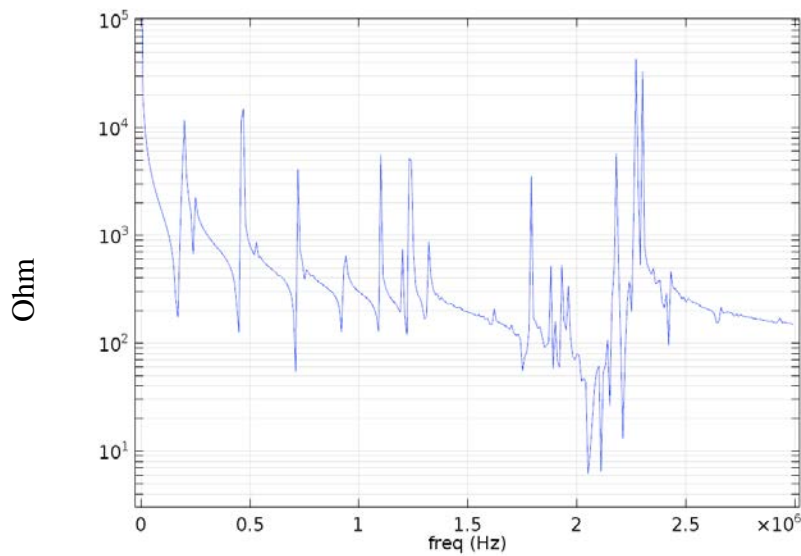


Figure 3.3 Impedance spectrum of $1 \times 10 \times 10 \text{ mm}^3$ thick PZT

Figure 3.3 illustrates the result of simulation of a $1 \text{ (thickness)} \times 10 \times 10 \text{ mm}^3$ PZT, the y axis is the impedance with unit of Ohm, and x axis is the frequency. As expected, the fundamental TE resonance dominates and induces the lowest impedance point around 2 MHz with some weakly coupled vibration mode. Other radial and bending vibrational mode can still be seen at lower frequencies. Different from the actual measurement, more vibration mode can be obtained due to the fact that PZT was being clamped during the measurement so that some vibrations are restrained. However, in the simulation, free boundary condition gives more freedom to the motion of elements. To study the effect of dimension to the resonant frequency, the length of two sides of previous PZT disk was gradually reduced to a cube.

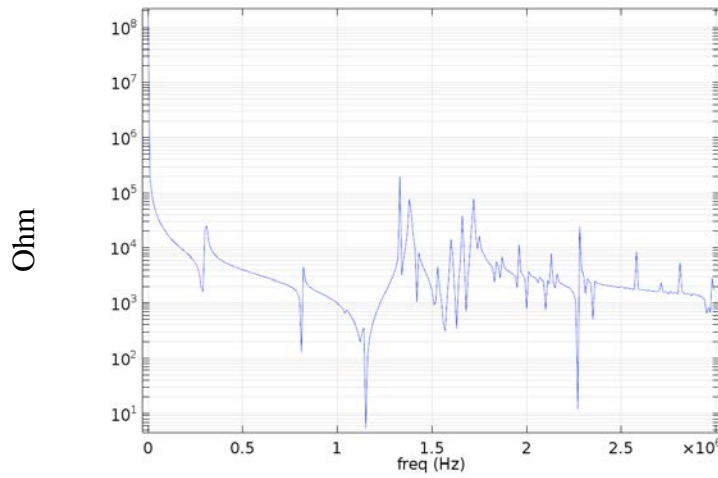


Figure 3.4 Impedance spectrum of $1 \times 1 \times 5 \text{ mm}^3$ thick PZT

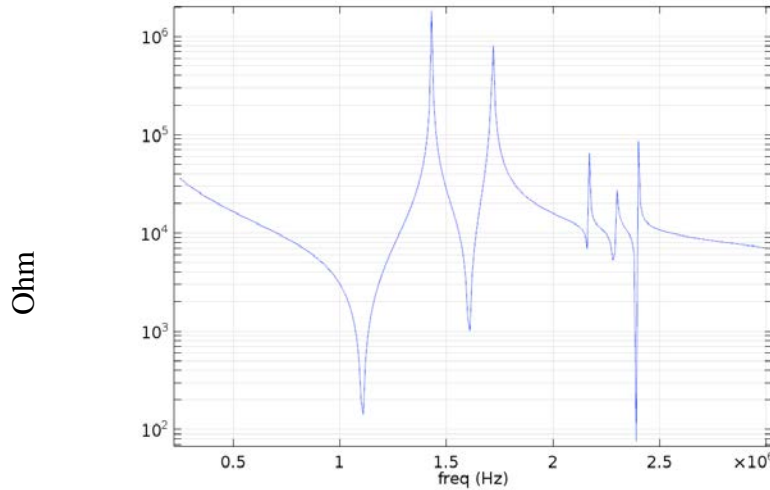


Figure 3.5 Impedance spectrum of $1 \times 1 \times 1 \text{ mm}^3$ thick PZT

The impedance simulation results for PZT in two dimensions, $1 \times 1 \times 5 \text{ mm}^3$ and $1 \times 1 \times 1 \text{ mm}^3$ are shown in Figure 3.4 and Figure 3.5 respectively. The resonant frequency along the small sides becomes more significant as the length being reduced to be comparable with the thickness. A vibration mode at 1.15 MHz creates the minimum point for the electrical impedance. This is due to the effect of that small width. In a more cubic design as Figure 3.5, the symmetric dimensions of the PZT embodies less vibration modes be coupled. Many vibration modes converge, and large vibration mode is detected at the frequency of around 1.15 MHz. This resonance has the same frequency as the 2 mm-thick PZT disk transducer which means this transducer-receiver pack and maximize the power transmission at 1.15 MHz.

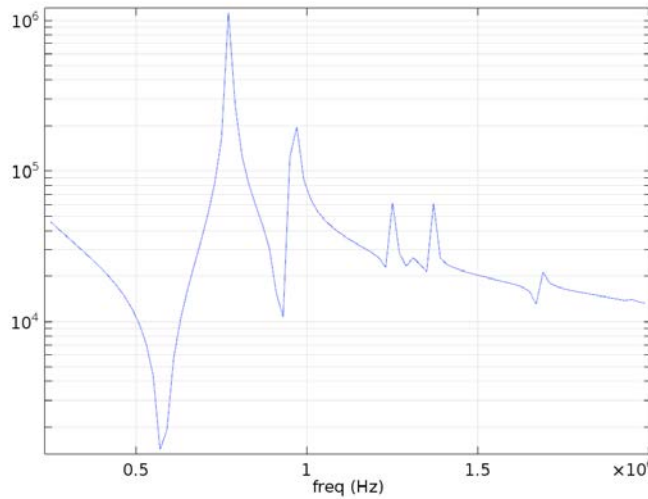


Figure 3.6 Impedance spectrum of $1 \times 1 \times 1 \text{ mm}^3$ thick PZT

Two other simulations are also conducted for two different dimensions, $2 \times 2 \times 2 \text{ mm}^3$ and $2 \times 4 \times 2 \text{ mm}^3$. These two configurations have been used for some of the devices being described in the following chapters. The impedance result for $2 \times 2 \times 2 \text{ mm}^3$ and $2 \times 4 \times 2 \text{ mm}^3$ are shown in Figure 3.6 and Figure 3.7 respectively. For $2 \times 2 \times 2 \text{ mm}^3$ PZT, the resonant frequency was simulated to be around 570 kHz and the resonance for $2 \times 4 \times 2 \text{ mm}^3$ PZT was simulated to be around 610 kHz. These two frequencies are close to the resonance of 2 mm-thick PZT and thus can be selected to produce large electrical output voltage.

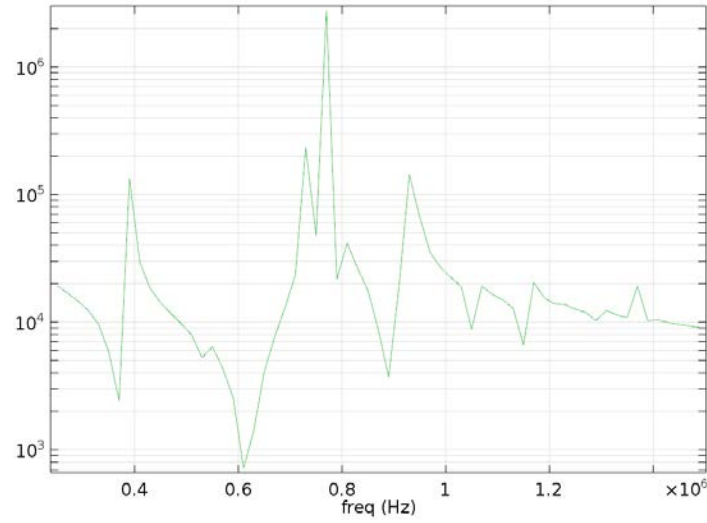


Figure 3.7 Impedance spectrum of $1 \times 1 \times 1 \text{ mm}^3$ thick PZT

To verify the design and simulation result. The PZT disk at 1 mm and 2 mm thickness were then diced into three different sizes, $1 \times 1 \times 5 \text{ mm}^3$, $2 \times 2 \times 2 \text{ mm}^3$, and $2 \times 2 \times 4 \text{ mm}^3$, using a wafer dicing saw (Disco DAD-2H/6 Dicing Saw). We measured impedance spectrum of three different PZT samples with the impedance analyzer. The measured results are shown in Figure 3.8, Figure 3.9, and Figure 3.10.

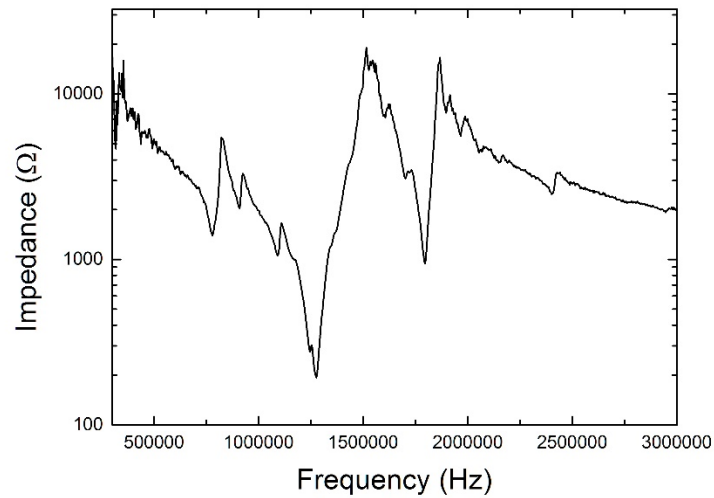


Figure 3.8 Impedance spectrum analysis of $1 \times 1 \times 5 \text{ mm}^3$ PZT

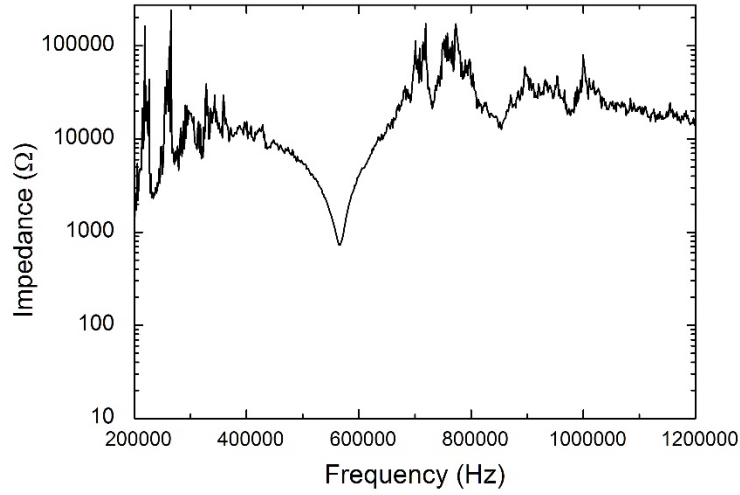


Figure 3.9 Impedance spectrum analysis of $2 \times 2 \times 2 \text{ mm}^3$ PZT

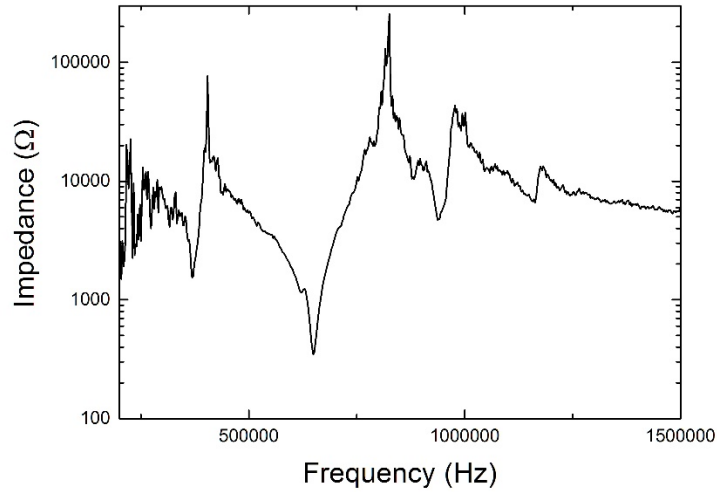


Figure 3.10 Impedance spectrum analysis of $2 \times 4 \times 2 \text{ mm}^3$ PZT

As compared to disk samples, more resonant modes are observed, and the first thickness-mode resonance alters to lower frequencies: 1) 1.27 MHz for $1 \times 1 \times 5 \text{ mm}^3$ PZT; 2) 566 kHz for $2 \times 2 \times 2 \text{ mm}^3$ PZT; 3) 651 kHz for $2 \times 4 \times 2 \text{ mm}^3$ PZT. Thus, for the highest powering efficiency, the resonant frequency of the transmitter should match the resonance of receiver. However, such requirement results in an increase of the transmitter thickness which increase the difficulty of

fabrication. In order to increase the converted voltage, the operation frequency should be firstly matching the resonance of PZT receiver.

3.3 Acoustic Impedance of Materials

For implantable medical device, like implantable micro oxygen generator (IMOG) which has been developed by our group [26], more concerns are drawn onto the issues with biocompatibility and acoustic matching of the device. Due to the potential toxic agents in the device, especially from piezoelectric material, some encapsulation technologies have been developed for ultrasonic transducers. A hermetic epoxy (353ND, Epoxy Technology) is used as encapsulation for ultrasonically powered nerve cuff stimulator [25]. The thickness of the coating and other related powering efficiency test is not provided. For capacitive micromachined ultrasonic transducer (cMUT), PDMS has been used for encapsulation for its good mechanical properties, low glass transition temperature as well as good biocompatibility [54]. The simulation results of 150 μm thick PDMS coating demonstrates that the pull-in voltage of cMUT can be preserved with a small offset to the resonant frequency. In another design by D. Seo, a thin layer of UV-curable epoxy was also used for the isolation for a ultrasonic powered neural stimulator [55]. There is no evidence of lead leakage for a packaging using UV-curable epoxy. Thus, new packaging technology and materials need to be studied for a better isolation for both lead and charges which can maintain the powering efficiency at the same time.

In a simplified configuration, a mismatch of acoustic impedance can cause a large reflection of acoustic power. One property of media can be defined as acoustic impedance evaluate the ability of carrying acoustic power like electric impedance:

$$Z = \rho v \quad (3.4)$$

where Z is the acoustic impedance (unit: MRayls or Rayls), ρ is the density of the material and v is the travelling velocity of sound. If a situation of sound transmission from air to water is considered as shown in Figure 3.11. The power reflection ration is given by:

$$R = \frac{(Z_{water} - Z_{air})^2}{(Z_{water} + Z_{air})^2} \quad (3.5)$$

where Z_{water} is 1.5 MRayls and Z_{air} is 420 Rayls. It can be easily calculated that 99.9% of incident power will be reflected. Similarly, if we consider PZT and soft tissue transmission, Z_{PZT}

of PZT-5A is 33.7 MRayls and $Z_{soft-tissue}$ is around 1.5 MRayls. Then the reflection can be as high as 84%.

Thus, instead of using thin layer of coating for isolation and packaging, for most ultrasonic transducers, Figure 3.12 [50], to maximize the transmission efficiency, an impedance matching layer is needed since most of the piezoelectric materials are hard materials such as PZT with a higher acoustic impedance resulting in a lower transmission at the interface. Thus, a single or multiple-layer structure can serve both as isolation and impedance matching layer at the same time.

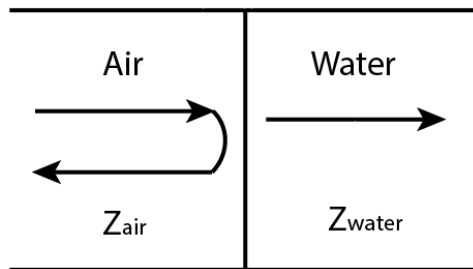


Figure 3.11 Acoustic reflection at air-water interface

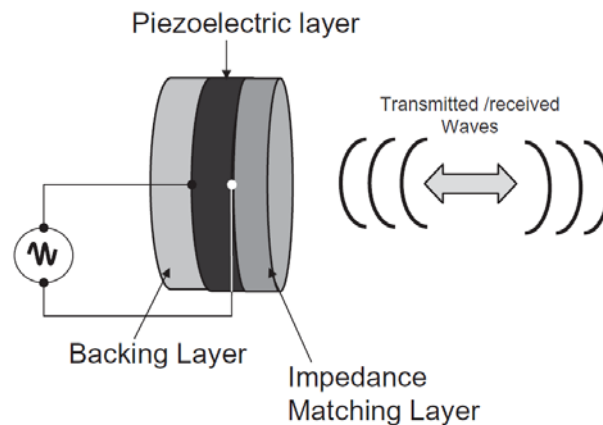


Figure 3.12 Configuration of ultrasonic transducer consisting of three layers: a piezoelectric layer, an impedance matching layer and a backing layer which absorbs the ultrasound on the backside

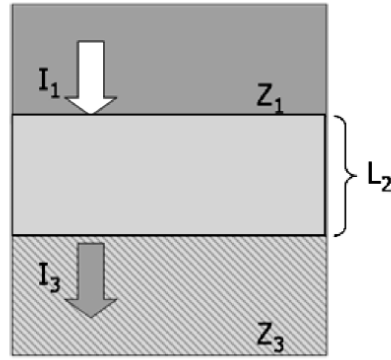


Figure 3.13 Three-layer structure for the case of impedance matching layer (center layer)

To understand the importance of impedance matching layer for increasing the transferring efficiency, we consider a sandwich structure as shown in Figure 3.13 [50]. The acoustic impedance of two interfaced materials are presented as Z_1 and Z_3 and the transmission coefficient γ is given by [50]:

$$\gamma = \frac{I_3}{I_1} = \frac{4Z_1Z_3}{(Z_3+Z_1)^2 \cos^2(K_2L_2) + (Z_2 + \frac{Z_1Z_3}{Z_2})^2 \sin^2(K_2L_2)} \quad (3.4)$$

where I_1 and I_3 are transmitted acoustic intensity in two materials. K_2 is the wave number for the intermediate layer. If we consider a special case that $L_2 = (2n-1)\lambda_2/4$, then the above equation can be simplified to:

$$\gamma = \frac{I_3}{I_1} = \frac{4Z_1Z_3}{(Z_2 + \frac{Z_1Z_3}{Z_2})^2} \quad (3.5)$$

and if $Z_2 = \sqrt{Z_1Z_3}$, the transmission coefficient will be 1 which means that all the energy can be delivered to the tissue.

If we consider the acoustic impedance of tissue and PZT, the ideal acoustic impedance for matching layer can be calculated to be around 7 MRayls. However, only very a few biocompatible materials have such acoustic property. Therefore, multiple layer matching is more practical for implantable devices. A simulated result showing that two-layer matching with a layer of cyanoacrylic glue (0.02 mm) and graphite (1.3 mm) can provide a good impedance matching for PZT [52]. Nevertheless, the thickness of graphite layer is close to the PZT element we used (1-2 mm) which will greatly increase the size of our device.

To accommodate the idea of matching layer to millimeter scale device, the optimized thickness of matching material needs to be re-calculated instead of assuming the quarter wavelength. To resolve

the question, a transmission matrix model can be applied to find out the most appropriate thickness for different materials.

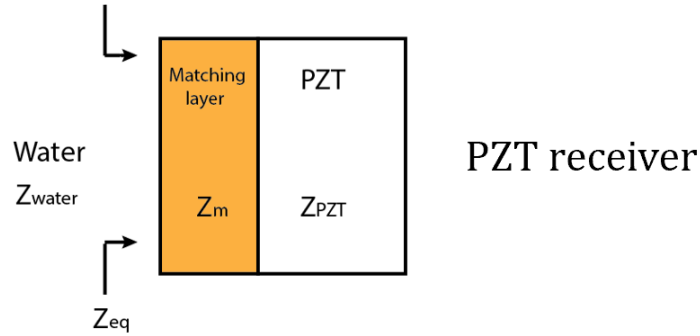


Figure 3.14 Matching layer structure for PZT enabled ultrasonic powering

If the case in Figure 3.14 is considered, the transmission matrix for each layer can be interpreted as [56]:

$$T_m = \begin{bmatrix} \cos\theta_m & jZ_m \sin\theta_m \\ \frac{j}{Z_m} \sin\theta_m & \cos\theta_m \end{bmatrix} = \begin{bmatrix} T_{m11} & T_{m12} \\ T_{m21} & T_{m22} \end{bmatrix} \quad (3.6)$$

$$\theta_m = 2\pi \frac{t_m}{\lambda_m} \quad (3.7)$$

where Z_m is the acoustic impedance of the material and t_m and λ_m are the thickness of the material and sound wavelength respectively. Then, one can calculate the equivalent acoustic impedance of certain thickness by:

$$Z_{eq} = \frac{T_{m11}Z_{PZT} + T_{m12}}{T_{m21}Z_{PZT} + T_{m22}} \quad (3.8)$$

As defined previously, the power reflection ration can be derived by:

$$R = \frac{(Z_{water} - Z_{eq})^2}{(Z_{water} + Z_{eq})^2} \quad (3.9)$$

And the transmission is nothing but:

$$T = 1 - R \quad (3.10)$$

As a result, once understand the acoustic property of a material, the optimized thickness for sound wave transmission at certain frequencies can be easily calculated.

Thus, I propose a 3D printed impedance matching packaging scheme which can increase the powering efficiency without sacrificing the form factor of implantable devices. Another study has some preliminary biocompatibility test on UV curable 3D printing materials [57]. Moreover, such

impedance matching layer can also serve as encapsulation for the PZT receiver. To achieve this, 3D printing technology has been employed to fabricate a well-designed structure which has certain thickness at the sound impinging surface serving as matching layer. For the other surfaces, 3D printing material is used as packaging material for isolation and biocompatibility improvement. A fabricated structure is illustrated in Figure 3.15. For the 3D printed being used (Formlab Form 2), the minimum controlled wall-feature thickness can be down to 300 μm which is enough for the matching purpose for the design of our device. A more complicated design can also be well-supported as the nature of 3D printing itself. A complete study of enhancement for biocompatibility still needs to be conducted to verify the design. The acoustic property of the material and the measurement have been done using a water tank setup. An improvement of the acoustic power transmission can also be visualized.

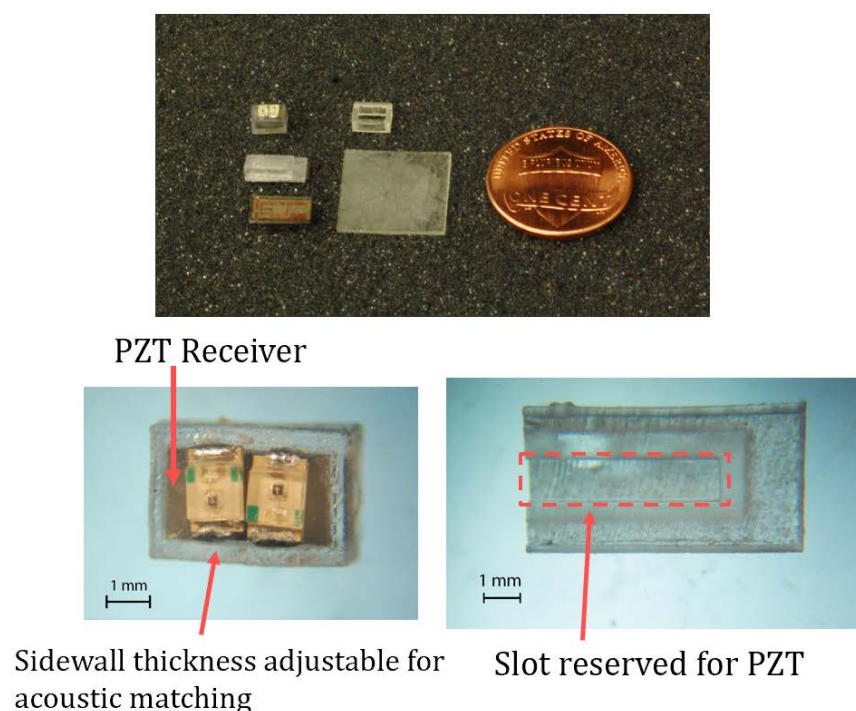


Figure 3.15 Fabricated ultrasonic powered device packaging with acoustic matching

To calculate the thickness needed for the design, the acoustic property of 3D printing material was firstly measured. The sound traveling velocity was firstly measured with a configuration as shown in Figure 3.16. The setup consists of a pair of ultrasound transmitter and receiver in the water. The

transmitter was driven by a signal generator which generates a 1kHz pulse signal. The pulse signal was then detected by a PZT receiver. The time delay was then recorded with and without sample being placed in between. The velocity measurement was then calculated with the sound traveling time difference using equation 3.11, where v_{water} is 1498 m/s.

$$v_{sample} = \frac{v_{water}}{1 - \frac{\Delta t v_{water}}{d}} \quad (3.11)$$

The measured sound traveling speed of 3D printing material is 2694 m/s and the density of the material was also measured to be 1.17 g/cm³. Thus, the acoustic impedance of the material can be calculated using equation 3.4 which is 3.17 MRayls.

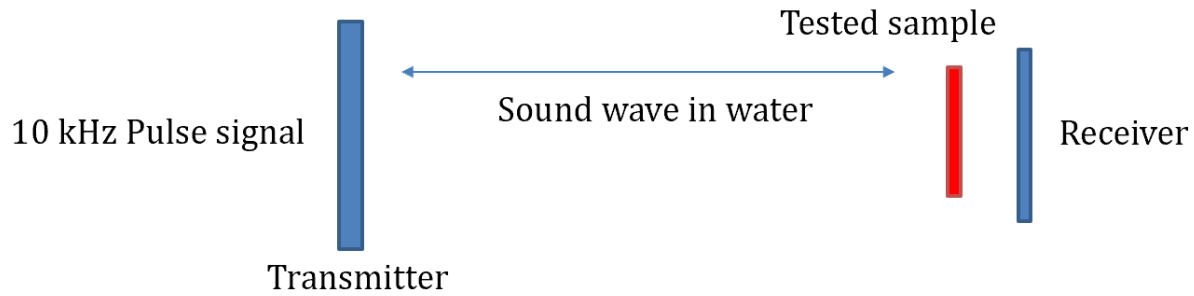


Figure 3.16 Sound travelling velocity measurement

With this information, the acoustic power transmission at various thickness was then calculated using equation 3.6-3.10. The calculation was conducted at 2.3 MHz. The numerical result is plotted in Figure 3.17. Due to the periodic property of wave transmission, there is a repeated pattern for power transmission at different thickness. As we predicted using the simplified equation 3.5, the transmission without matching layer is only 16%. Another lowest transmission point is at around 580 μm . At 290 μm and 880 μm , the power transmission reaches its maximum at 55% which is more than 3 times than the original transmission. Thus, to increase the power transmission through 3D printing material, a optimum thickness would be around 300 μm and 900 μm .

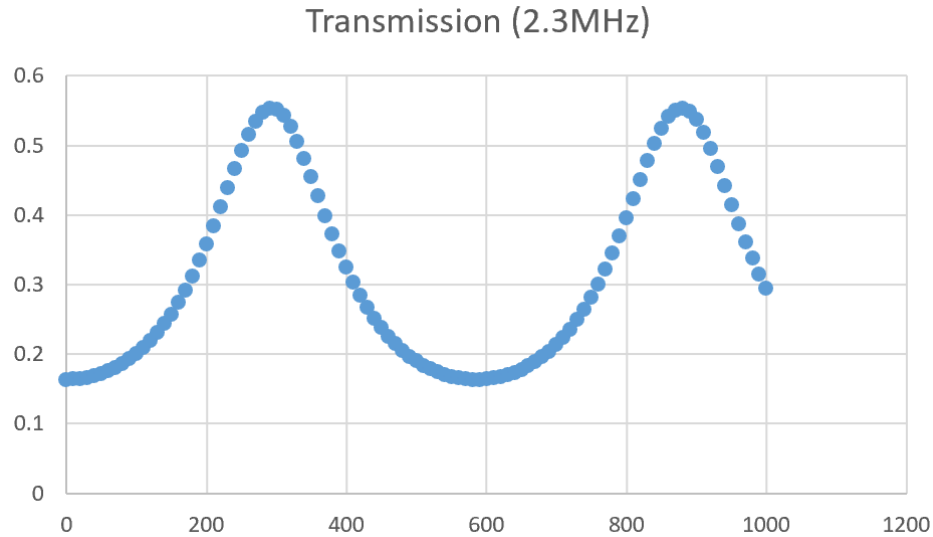


Figure 3.17 Power transmission calculation at 2.3 MHz with 3D printing material

To verify the feasibility of using this material as matching layer, several plastic tiles were printed and attached onto a PZT plate. A fiber optic hydrophone scanned through each sample to measure the power being delivered through the PZT to show a relative transmission. The whole setup was placed under water, as shown in Figure 3.18. Sound absorption layers were attached to the sidewall, the movement of the hydrophone was controlled precisely by the step motor. Acoustic pressure was measured multiple times for average and standard deviation.

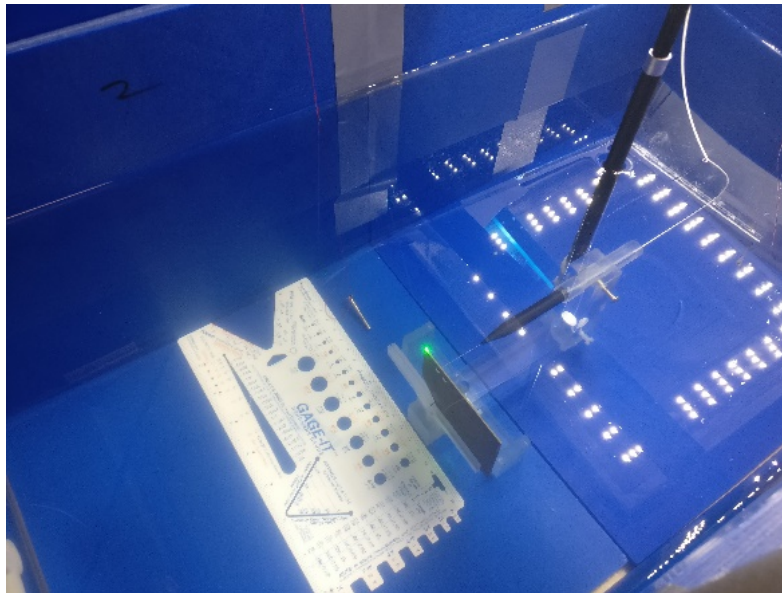


Figure 3.18 Power transmission water tank setup for matching layer

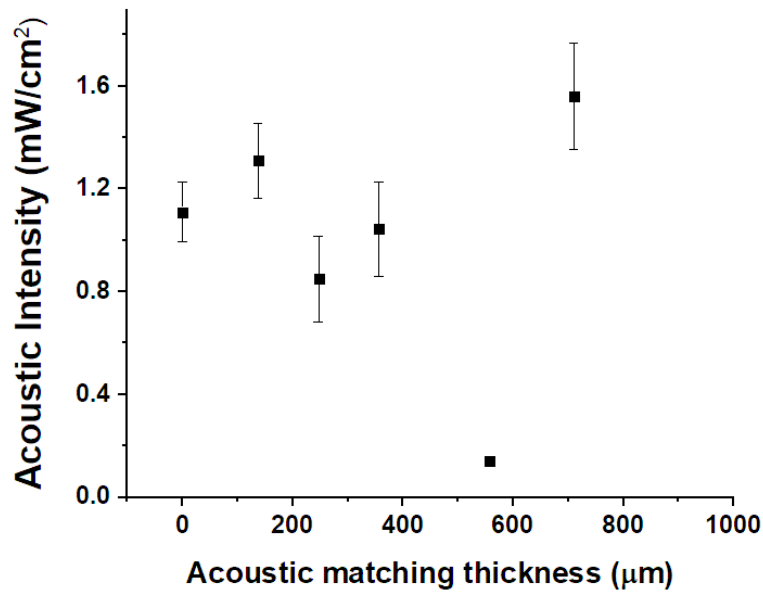


Figure 3.19 Measured transmitted acoustic intensity at 2.3 MHz

The measured results were summarized in Figure 3.19. The input voltage on signal generator was 100 mV peak-to-peak voltage amplified by 55dB. The PZT used was a 70 mm by 70 mm and 2 mm thick PZT transducer. Sample was placed 25 cm away from the transducer. Since the 3D printer used didn't provide a high-resolution printing, the printed sample had unevenly distributed thickness.

As a result, an improvement of 17% has been achieved at 137 μm and 40% increase for 710 μm. However, we saw low acoustic intensity at 300 μm and 500 μm. Such reduced intensity is probably because of the air being trapped between layers while bonding. Moreover, a low-quality printing with thin layer could also contribute to the difference between fabricated samples and theory.

As a proof of concept, some improvement has been achieved with 3D printed matching layer. Even though some defects and bonding issue still need to be addressed and more test on biocompatibility needs to be done, the result is promising and reveal the potential of applying 3D printing technology to implantable medical devices.

4. ULTRASONICALLY CONTROLLED POWER MANAGEMENT SYSTEM

4.1 Introduction

In this chapter, an implantable device is presented as my previous work regarding ultrasonic control. An ultrasonically controlled power management circuit has been design, fabricated and tested, which can significantly preserve the energy of on-board battery in implantable electronic devices. Part of the text is taken from the publication by the author [47][58].

4.2 Background and System Overview

Batteries have been selected and favored for power source for implantable medical devices for over four decades. Lithium ion based batteries were invented in the 1970s [14]. This invention later became the major method of powering for implantable electronics such as cardiac pacemakers. Some implantable medical devices such as deep brain stimulators and cardioverter defibrillators need to be powered for up to 10 years without replacement of on-board power source. These batteries can provide an electric current level from micro-amperes to mili-amperes in a relatively small form factor [15]. After the invention of a lead-less pacemaker, Micra by Medtronic, its miniaturized battery, an embedded lithium-hybrid battery in less than 0.8 cm^3 form factor, has drawn a lot attention to the improvement of longevity of implantable devices. Medtronic invented these cylindrical-shaped miniature batteries that can last for up to 12 years [16]. Another good example of implantable sensing system is Medtronic insertable Reveal® ECG system that can readily monitor heart beat and rhythms for several year (up to three years) without the need to change the battery [59].

Implantable diagnostic and therapeutic systems usually drain power quickly (depending on the number of operations and power-hungry electronics) and a continuous operation in drastically reduce the lifetime of battery. Energy can be easily conserved by turning the system on and off intermittently following a determined manner. As a typical instance, a wireless microsystem for medical application was designed by S. Majerus. This system uses an integrated circuit to reduce and control the operational time to save the battery power [10]. Another system uses a commercial System-on-Chip system (SOC) (CC1110F32, Texas Instrument, USA) as the main approach to

achieve the power control. Such device only has a current consumption of around 1.5 μA current in the sleep mode [22]. The power consumption was mainly reduced by the low-power design of the SOC itself.

An alternative approach to save the on-board power is to employ a remote control, such as RF transmitter, to turn the system on and off. Although direct usage of off-the-shelf system can be controlled wirelessly, RF transceiver still consumes current (μA) in the standby mode. Therefore, such scheme is not suitable for long-term devices. An independent power management system or a passive control system/wireless powered system is ideal for long-term power-saving purpose. Santic and his team have developed a RF switch which consumes only 25 nA at 1.35V power supply voltage in its bi-stable mode while it is in idle [23]. Another radio frequency power management circuit has also been designed to save battery power [24]. Following this design, a RF detector in standby mode which consumes only 100 nA at 2.7 V supply voltage was designed in a pre-determined process to active the device on demand to save the power.

In this work, an ultrasonically controlled power management system is presented to save the energy of on-board battery. The system is powered by the battery from the host and can be controlled individually using the ultrasound signal from external side. One of the potential application of this system will be the implantable urinary bladder pressure monitoring system [22] which is also designed by our group. The on and off state can be easily altered as explained in our previous work [58]. Ultrasonic powering or coupling has attracted considerable attention [26], [52], [60], [61]. This technology offers low or almost zero standby power consumption, and design simplicity. The receiver size can also be reduced for the consideration of overall form factor of the device. In addition, ultrasound has other advantages such as high penetration depth and higher tolerance to the angular misalignment [36].

4.2.1 Device Operation

To save the electric energy in battery-powered implantable devices, an ultrasonic controlled power management circuit has been developed. Figure 4.1 depicts the schematic of the proposed system, an ultrasonically controlled power management system (UCPMS) integrated with a battery-powered device to switch the state of the system. The UCPMS has its power supply connected to the battery or other main power source. The switching system can be controlled by the signal in a specific pattern which is transmitted by ultrasound from the outside. A piezoelectric transducer

follows the ultrasound intensity pattern which is interpreted in a form of generated electric signal. The signal pattern of the controlling signal can be well-designed to increase the reliability of the system control and avoid mis-operation which might be induced by the noise.

The controlling signal is only required the switching for the system. When the state is changed, ultrasonic wave can be turned off. Only a certain pattern of ultrasonic signal (from high to low) can trigger the switch. When the ultrasound in a certain wave form strikes the receiver, the wave pattern will be recognized. Once the operation of the main system is completed, another signal toggle the implant electronics off. Since the only power consumption comes from only a couple of components, this design minimizes the current consumption which offers a much longer battery longevity. Such module can be easily integrated into most current applications without a large change of the circuit in the main system.

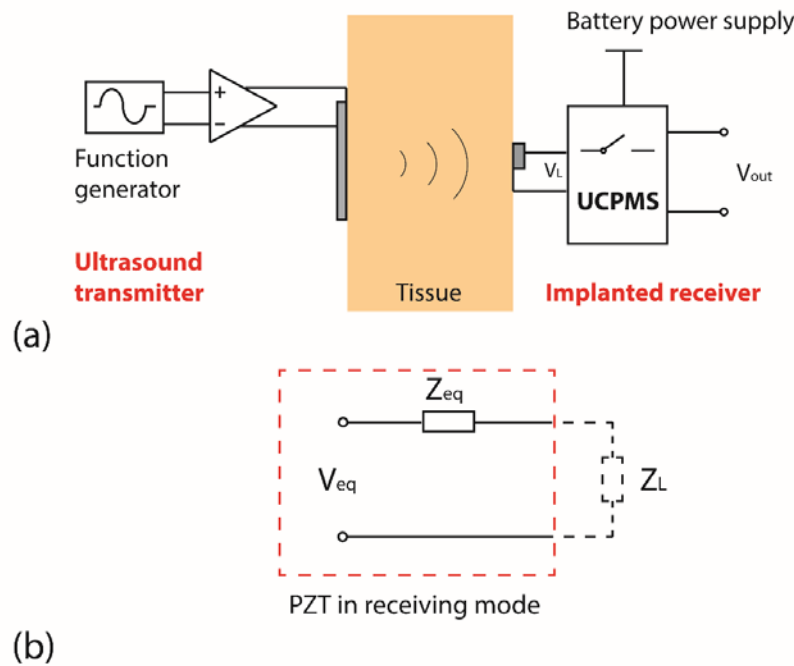


Figure 4.1 System block diagram of (a) UCPMS system (ultrasound transmitter and implanted receiver), and (b) equivalent circuit PZT as an energy converter.

4.2.2 Circuit Schematic

The block diagram of the is illustrated in Figure 4.2. Four nodes are labeled on the figure to reveal the signal pattern at each point. A piezoelectric (PZT-5A) receiver, in a size of $2 \times 4 \times 2 \text{ mm}^3$, was

selected as the main energy converter. This PZT element was designed to operate at its first thickness-expander mode resonant frequency (665 kHz). Followed by the receiver, the signal conditioning circuit consists of a full-bridge rectifier, a Schottky diode and a filter capacitor (100 pF) were connected afterwards. As the main logic part, a Schmitt trigger chip (SN74LVC1G14, Texas Instrument), and a D flip-flop chip (SN74LVC1G80, Texas Instrument) were connected in the correct order to achieve the switching functionality. At last, a low-dropout regulator (LDO) was used to stabilize the output voltage. When the system is not on and the stand-by power consumption comes from only the Schmitt trigger and D flip-flop.

Four nodes of the circuit have been chosen to explain the signal flow of the system, Figure 4.2 (b). Firstly, ultrasound induced voltage (at node 1) is rectified and filtered by a full-bridge rectifier before entering the Schmitt trigger (at node 2). To further reduce the signal fluctuation at each node, a Schmitt trigger is selected which sets a threshold voltage to screen the fuzzy signals. As a result, a plosive edge is created at the output of the Schmitt trigger and such signal can be used as a clock signal for D flip-flop. To change the status of the system, the acoustic intensity input should be firstly lowered, which is later translated into a positive edge at the clock input of D flip-flop. The threshold voltage of transition for the Schmitt trigger was set to 1.5-1.87 V to avoid unintentional switching with 3 V power supply. Such threshold varies for different V_{cc} level and D flip-flop type. Once the \bar{Q} output is connected to the D input, the \bar{Q} output toggles on every positive edge at the clock input. Note that for most commercially available D flip-flop, there is a voltage drop between the power supply voltage (V_{cc}) and the output voltage. For example, under 3 V power supply, the maximum output voltage of D flip-flop we used is measured to be 2.9 V (with high load resistance). It is important to note that the maximum output current also needs to be sufficient for the controlled system. For example, the output current should achieve certain current level (mA) for most RF modules.

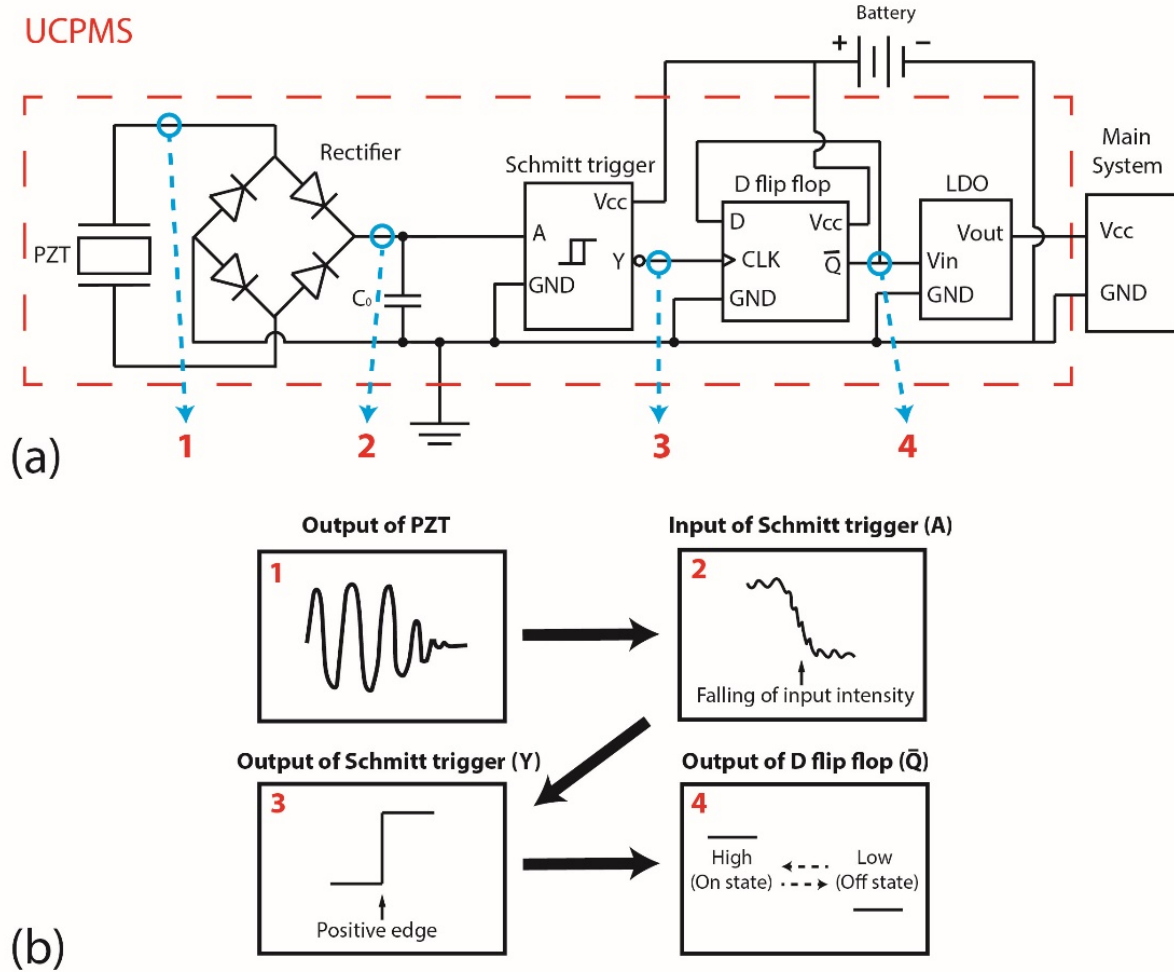


Figure 4.2 Circuit diagram of the UCPMS and signal patterns at four points: 1. electric output of PZT receiver; 2. rectified electric signal; 3. output of the Schmitt trigger; 4. output signal of D flip-flop.

4.3 Fabrication

The prototyping process of the UCPMS is illustrated in Figure 4.3. Instead of using printed circuit board (PCB), a copper clad polyimide substrate is chosen to reduce the cost for prototyping. The circuit trace is design and transferred to the substrate through toner transfer method. The designed layout is directly laser-patterned and cut using CO₂ laser (PLS6MW, Universal Laser System). After the removal of redundant copper tape, a $2 \times 4 \times 2 \text{ mm}^3$ PZT-5A receiver (PZT-5A4E, Peizeo Systems Inc., MA, USA) and all other components are sequentially soldered onto the substrate, Figure 4.3 (b).

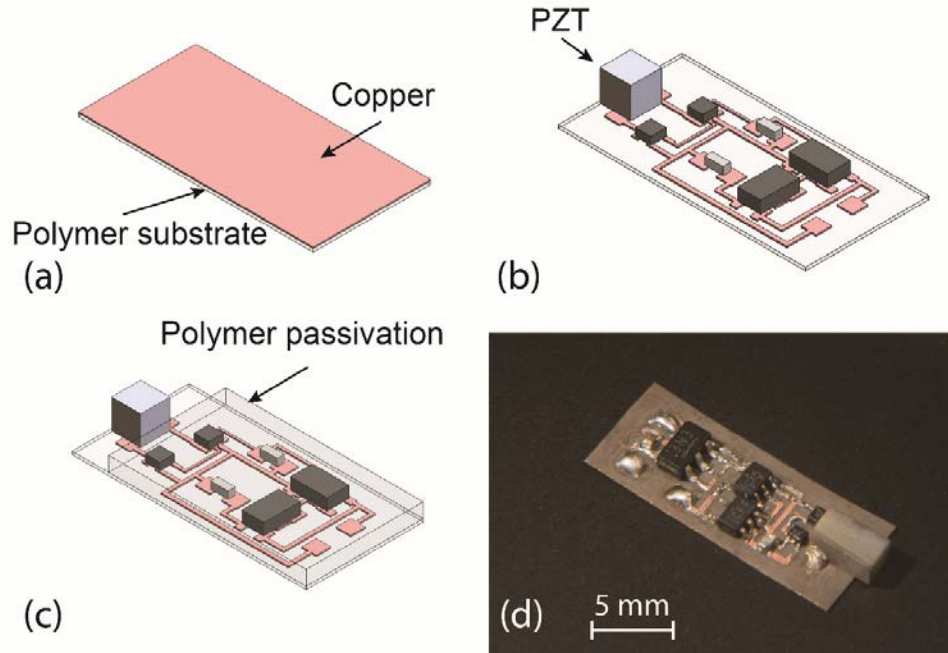


Figure 4.3 Fabrication process: (a) Pattern the circuit on copper clad polyimide substrate; (b) solder components onto the substrate; (c) polymeric packaging and passivation with parylene-C; (d) fabricated UCPMS circuit.

After soldering, a passivation layer is needed to provide the isolation and bio-compatibility for the electronics. Finally, a 5 μm thick Parylene-C was deposited onto the system for the final passivation. The Parylene-C coating has been widely used to create a good isolation from other electrical interference. The fabricated system is shown in Figure 4.3 (d).

In addition of the fabrication of UCPMS, in order to test the driving capability for a basic RF communication system, an ultrasound-controlled RF transmitter is designed using Attiny 85 micro-controller (Atmel Corporation, USA) and a 2.4 GHz wireless module (nRF24L01, Nordic Semiconductor, Norway). A 3 V battery (CR2032, Panasonic, Japan) is integrated as the power source. The whole system can be packaged in 1.5 mm-thick acrylic shell. The dimension of this device is measured to be $3.1 \times 2.6 \times 1.4 \text{ cm}^3$. It is important to note that the PZT receiver is placed outside the acrylic shell (red circle in the photograph) since the acrylic shell has a higher acoustic impedance which significantly impedes the ultrasound transmission. In this device, the PZT is connected to the reserved pads of UCPMS with wires. The size of such device can be smaller if the circuit is integrated into an ASIC design.

4.4 Experimental Results

4.4.1 *In Vitro* Results

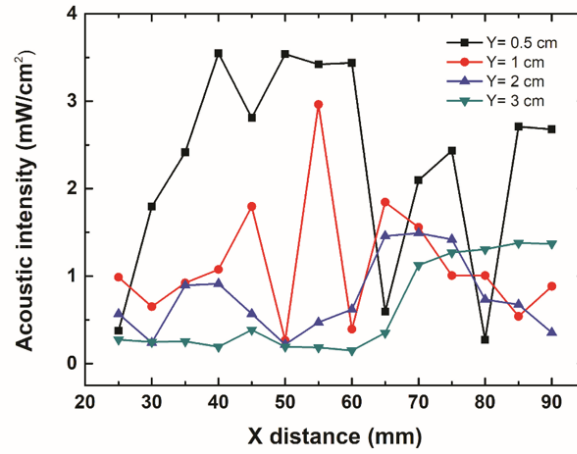


Figure 4.4 Rectified output voltage at various distance along central axis in a non-reflective condition

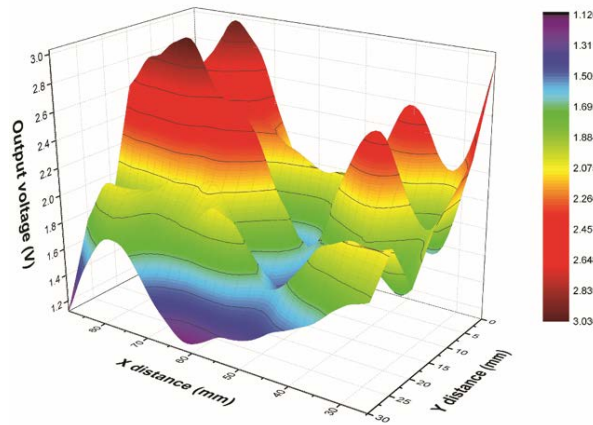


Figure 4.5 Rectified output voltage at various lateral distance in a non-reflective condition

The output voltage at node 2 was firstly measured to verify the output power of PZT. The test was done in a non-reflective condition with absorption layers placed on the side-wall. The experiment setup was similar to Figure 2.12 with UCPMS being placed at the center. Since echo is eliminated from the experiment, similar to the acoustic results in the previous chapters, the converted voltage changes rapidly within the near-field range. During the measurement, the poling direction of the receive PZT is parallel to the central axis of the transmitter. Figure 4.4 plots the output voltage along the central axis (x) while the acoustic input acoustic intensity was set at 3.5 mW/cm^2 . The

output voltage is generated by a $2 \times 4 \times 2 \text{ cm}^3$ PZT element. Several maximum and minimum points are observed along the central axis. The transducer, 3.5 cm in diameter, can provide an operational range up to 9 cm distance away from the transmitter. By increasing the size of the transmitter and the input acoustic intensity, the operational range can be increased. Figure 4.5 is a 3D plot indicating the output voltage measurements at different central-axial and lateral distances away from the central axis. As shown, the output power varies and drops drastically when lateral distance increases. Thus, the transducer needs to be large enough to guarantee the functionality. The switching and power characteristics of UCPMS were also measured. By decreasing the acoustic input, a drop of the converted voltage is observed at node 2. Such signal can trigger an output change which consequentially changes the status of the system. As measured, the falling time of rectified voltage decreases from 0.5 ms at the rectifier to around 2 ns at the output of D flip-flop, Figure 4.6. This switching time is short enough to satisfy the timing constraints for most embedded systems.

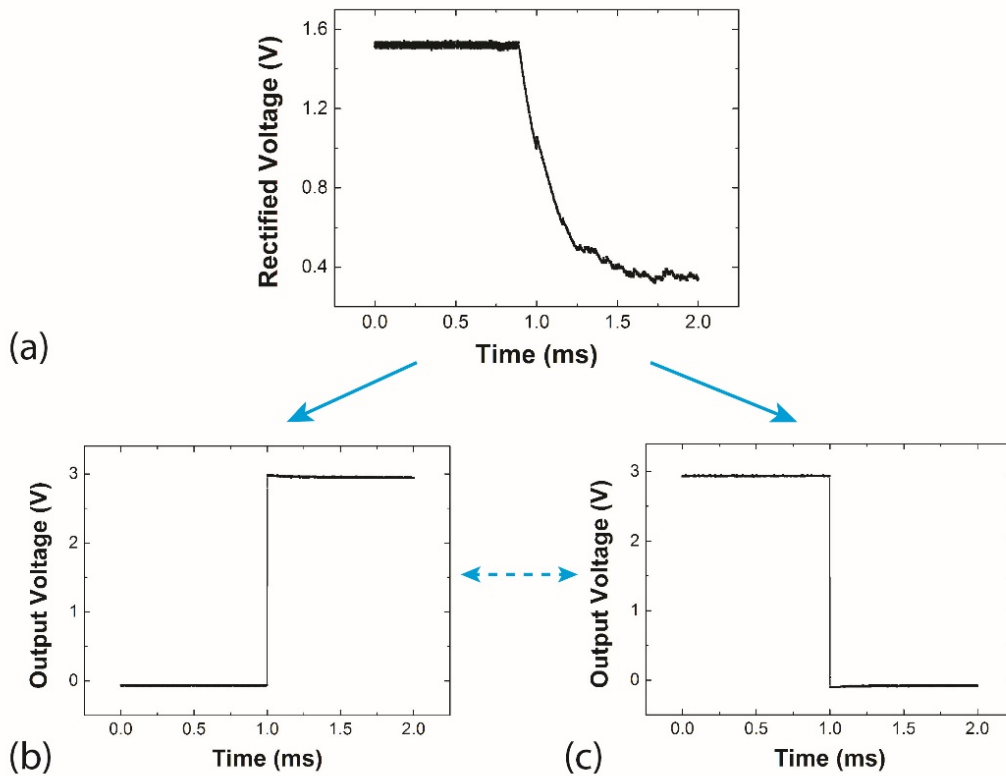


Figure 4.6 Switching time of UCPMS: (a) voltage drop at node 2 as input acoustic intensity decreases; (b) output (at node 4) change from low to high; (c) output (at node 4) change from high to low.

The output of D flip-flop is also depicted as an I-V curve plot when different load resistors were applied, as shown in Figure 4.7(a). The ultrasonic wave was kept off all the time to simulate the real situation. As shown in the IV curve, the output current decreases at higher output voltages. The maximum output power can be detected at a load of $92\ \Omega$ where the output power is around 48 mW. Thus, battery type, and electrical requirements must be appropriately designed to maintain a reliable operation of controlled electronics.

The output power of a 2.5V LDO regulator (Toshiba, Japan) was then measured, Figure 4.7(b). The output voltage can be tuned by using different LDO and D flip-flops. As expected from a standard LDO, the output voltage can be maintained at 2.55 V with a current lower than 10 mA. The maximum output power can be observed with a load of $76\ \Omega$.

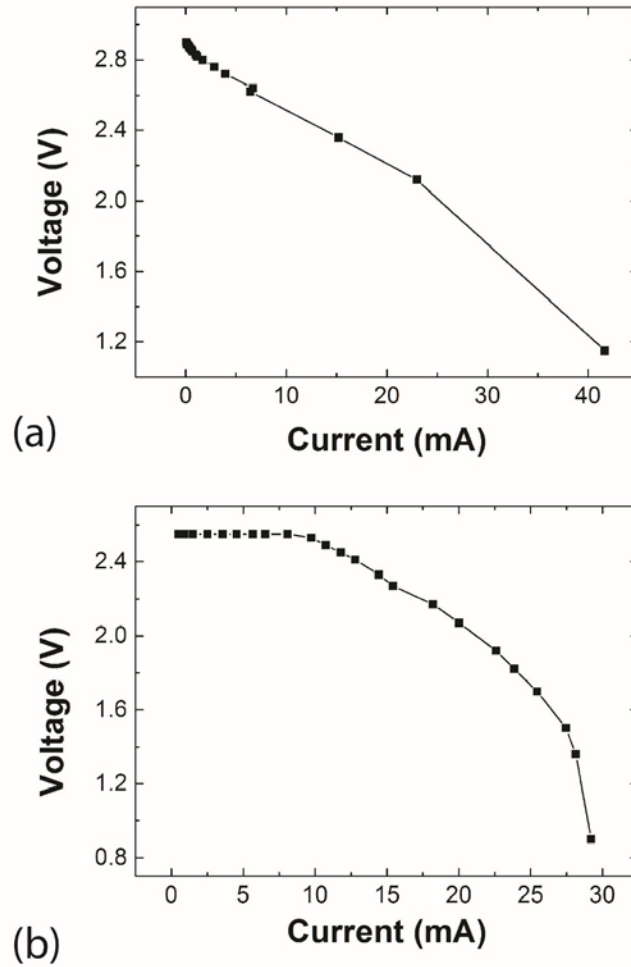


Figure 4.7 (a) I-V output characterization of UCPMS; (b) I-V output characterization of 2.5 V LDO regulator.

Since the output driving capability depends largely on the D flip-flops being used. Several D flip-flops on the market are compared in Table 3.1. As shown, in this work, the maximum output voltage can be 2.12 while maintaining an output current at 23 mA. The current consumption in the off-state is also measured as one of the critical specifics. A source meter has been used to measure the current consumption in the off state. Table 3.2 is a list comparing several commercially available SoCs with their standby current consumption in a micro-amperes level. As compared, the off state current consumption of proposed UCPMS is only 14.5 nA. Additionally, these numbers excluded power consumption by any possible peripheral components (e.g., clock generators).

Table 4.1 Output characteristics of some common D flip-flops [47]

D Flip-flop Type	High level output voltage (v)	High level output current (mA)
SN74LVC1G80 (Texas Instruments, this work)	2.12 (measured)	23 (measured)
74LVC1G74 (Nexperia)	2.62	24
NC7SZ175 (Fairchild)	2.68	24

Table 4.2 UCPMS current consumption as compared to several commercial RF SoC systems [47]

RF-SoC Type	Current in sleep mode (μ A)
UCPMS (this work)	0.0145 (measured)
CC1110 (Texas Instruments)	1.5 (measured)[22]
CC430 (Texas Instruments)	1.7
RF430 (Texas Instruments)	< 20
Si4010 (Silicon Labs)	0.7
nRF905 (Nordic Semiconductor)	12.5

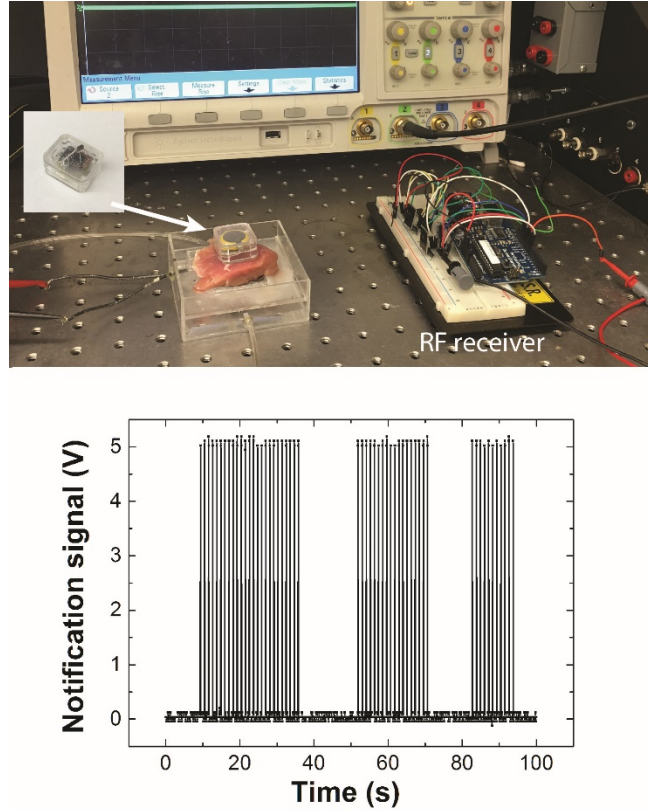


Figure 4.8 Notification signal for successful switching operations and photograph of ex vivo experiment setup.

4.4.2 Ex Vivo Results

Lastly, an *ex vivo* validation was performed with porcine tissues. The fabricated UCPMS with a RD system were tested cross a 2 cm-thick tissue. To visualize the change of the system, a received signal was shown on an oscilloscope when the system is on.

The ultrasound transducer was placed under the tissue for the operation. On the RF receiver end, as demonstrated on Figure 4.8, within a 100-second period, the device can be turned on and off three times successfully.

4.5 Conclusion

The author has developed an ultrasonically controlled power management system (UCPMS) for electronic implantable devices. The *in vitro* characterization on ultrasound transmission and power specifications of this system verifies the change of state with a low acoustic intensity operation.

An ultra-low standby power consumption was monitored which is lower than most RF controlled System-on-Chip systems. We believe this ultrasonic coupling technique can be applied to conserve the battery power and control the state of the implantable system which dose not require a continuous mode operation.

5. AN IMPLANTABLE MINITUARIZED LIGHT SOURCE FOR LOCALIZED PHOTODYNAMIC THERAPY

5.1 Introduction

Photodynamic therapy (PDT) is one of promising cancer treatments that has spatial control and can select the affected area to kill cancerous cells. It consists of two, otherwise non-toxic components: a photosensitizer (PS) and light. The photosensitizer generates cytotoxic agents only under light illumination with a specific wavelength. Although PDT's localized cancer treatment reduces many side effects, its adoption has been hampered by limited light penetration into most biological tissues. In this chapter, we introduce an ultrasonically powered implantable microlight source, μ Light, which enables *in-situ* localized light delivery to deep-seated solid tumors. Part of the text is taken from the publication by the author [39][62].

5.2 Background and System Overview

Three major cancer treatments, chemotherapy, radiation therapy and surgery have been adopted in modern clinical practice for decades [63]. For most of the tumor therapies, a lack of selectivity and the potential of attacking normal cells around the tumor simultaneously. Such spread of cytotoxic chemicals can cause some side effects such as constipation, nausea, fatigue, blood disorders, pain and hair loss. Researchers have developed several modalities to minimize the side effect which may take place aiming to increase the drug efficacy and interaction with target, without causing severe damage to healthy tissue. As one of the examples, immunotherapy has been intensively studied in both academy and clinic [64], [65]. Another example is photodynamic therapy (PDT), which delivers selective drug activation triggered by certain light [66], [67]. This therapy starts using a chemically coupled combination, which is photosensitizer (PS) and light. The photosensitizer is an agent which generates cytotoxic group due to light at certain wavelength. Energy-transfer playing an important role in generating toxic species. PS absorbs photons and can be activated from the ground energy state (S_0) to an excited state (S_1), as shown in Figure 5.1a. When it release energy and relaxes to ground state, two reactions undergo along with the energy transfer [68], [69]. The first reaction can form radicals that can transform oxygen into some singlet state products (1O_2). The other reaction directly transfer energy to oxygen. These two reactions

can both create reactive oxygen species (ROS) which is local toxic for malignant cells [70].

Although there are several obvious advantages over the conventional chemotherapy, the limited light penetration depth inside body has impeded the applications of PDT to deeply seeded tumors [71]. A possible approach to overcome this limitation is the use of wireless light source to locally deliver the light within the tumor [72], [73]. An inductively coupled implantable light source has been presented by Bansal [74]. A wireless powered LED chip which is encapsulated with biocompatible polymeric material, poly-dimethylsiloxane (PDMS), has been invented for metronomic PDT, which is a low-intensity long-term modality [75]. Some superficial or non-deeply seated organs could be accessed by fiber optic light source [76]–[79].

In this work, an ultrasonically powered micro light source, μ Light, has been proposed to overcome the aforementioned limitation for the application of PDT in other types of cancers. The device can be powered through ultrasound. The use of ultrasonic powering has the advantage of using small receiver for easy implantation. In addition, ultrasonic powering offers long range powering, which is not achievable by most inductive powering methods [26]. The μ Light is primarily targeted for non-metastatic unresectable solid tumors. An example is pancreatic cancer, which is unresectable for 80% of the cases. The μ Light can be implanted and used to shrink the size of the pancreatic tumor tissue which allows for the surgical removal [80]. Moreover, some recent studies in transmitting ultrasound across the bone structures to treat tumors has created the potential to use μ Light in more tumor types without the need for invasive removal of bones [81].

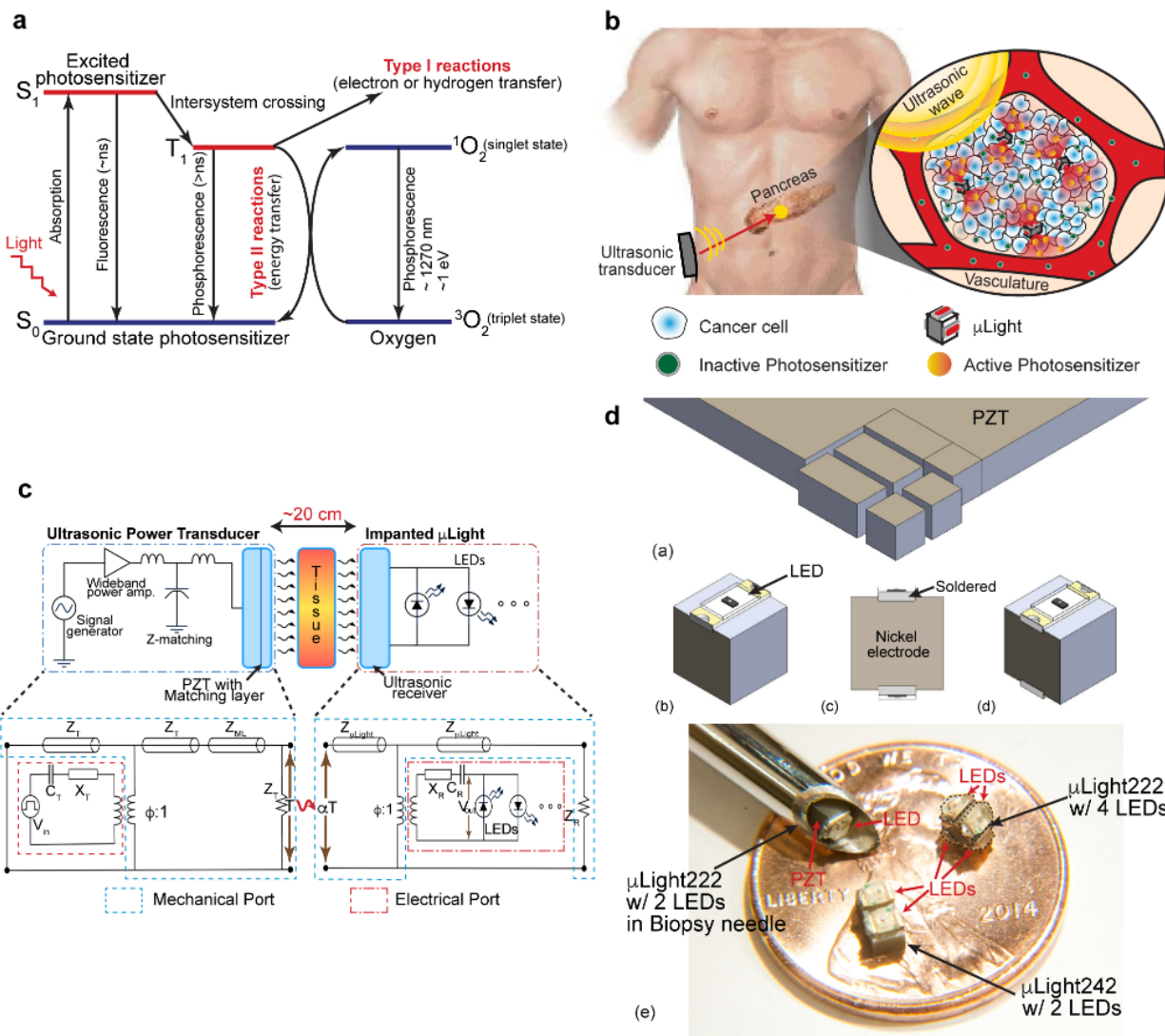


Figure 5.1 a. Photosensitizer: Light at certain wavelength excites the molecule from ground singlet state to an excited state. b. μ Light in a tumor: ultrasound activates the device to generate light resulting in a generation of reactive oxygen species (ROS) which is cytotoxic to the cells. c. Equivalent transmission diagram for ultrasonic powering [82]. d. Fabrication process: (a) PZT was firstly cut into $2 \times 2 \times 2 \text{ mm}^3$ and $2 \times 4 \times 2 \text{ mm}^3$ dimensions, (b-d) solder LEDs on PZT, deposit parylene-C for passivation, (e) fabricated prototypes.

5.3 Fabrication

The fabrication process of the prototype is illustrated in Figure 5.1d. The lead zirconate titanate disk (PSI-5A4E, Piezo Systems Inc., MA, USA) was micro-machined into two dimensions, $2 \times 2 \times 2$ mm³ (μ Light222) and $2 \times 4 \times 2$ mm³ (μ Light242), were selected based on previous characterizations. Two red LEDs (peak wavelength $\lambda = 640$ nm, Kingbright Ltd.) or two blue LEDs (peak wavelength

$\lambda = 470$ nm, Lite-On Technology Corp.) were soldered across the nickel electrodes of the PZT in a flipped polarization, Figure 1d(b). A more detailed information of components used were summarized in Table 5.1. The emission angles of the red LED and the blue LED are 120° and 130° respectively. Thus, the implantation of multiple LEDs can provide a viewing angle of nearly 360° . Lastly, 5 μm -thick parylene-C was deposited onto the device for passivation and biocompatibility, Figure 5.1d(d). Prototyped devices are shown in Figure 5.1d(e).

Table 5.1 Specifications of the components used in the μLight [62]

Characteristics of the PZT-5A receiver		Electrical and optical characteristics of LEDs	
Longitudinal velocity of sound in PZT-5A	4350 m/s	Peak wavelength for the red LED	655 nm
Thickness of the μLight PZT	2 mm	Peak wavelength for the blue LED	470 nm
Resonant frequency for the PZT, $\mu\text{Light}242$	672 kHz	Turn-on voltage for the red LED	1.55 V
Resonant frequency for the PZT, $\mu\text{Light}242$	720 kHz	Turn-on voltage for the blue LED	2.8 V

5.4 Experimental Results

Experimental validation of the device was firstly conducted using *in vitro* water tank experiment. Light generation and ultrasound transmission were measured to treatment evaluation. After power validation, cytotoxicity generated by the photosensitizer was validated with cell culture experiment. With promising *in vitro* results, *in vivo* test in animal model was then conducted to prove the efficacy of the μLight coupled photodynamic therapy.

5.4.1 Validation of Ultrasonic Powered Light Source

The light intensity is critical for activating photosensitizer. The light intensity characterization has been done using the setup similar to the setup as shown in Figure 2.12. The device was placed in water tank. The light irradiance was detected by PIN photodiode. The measurement was done with device being powered under different intensities and at various locations away from the transducer. The experimental result was extrapolated and plotted, Figure 5.2. Two plots on the left-hand side shows the output light irradiance at different acoustic input levels, ranging from 0 to 720 mW/cm^2 . Three curves were measured at 0 mm, 5 mm and 10 mm distance away from the LED. Red LED was selected for this measurement. During the test, the frequency was set to 650 kHz which is

close to the resonance as measured. In the case of $\mu\text{Light242}$, at 720 mW/cm^2 acoustic input, the light irradiance was diminished from around $80 \text{ }\mu\text{W/cm}^2$ to around $3 \text{ }\mu\text{W/cm}^2$ at 10 mm separation, Figure 5.2 (b). A degradation of 84% light intensity was measured from $\mu\text{Light222}$ at a distance of 5 mm. Thus, to increase the overall delivered light intensity, multiple implants are expected to acquire a higher irradiance.

As discussed in Chapter 2, the irradiances at different x separations also follow the acoustic intensity transmitting pattern in the near-field region, i.e., a series of maxima and minima along the axial direction. The corresponding light intensity generated by μLight along the central axis was also measured, as shown in Figure 5.2 on the right-hand side. The acoustic input was set to 185 mW/cm^2 during the measurement. As shown in the plot, the light intensity varies from $0.16 \text{ }\mu\text{W/cm}^2$ to around $0.01 \text{ }\mu\text{W/cm}^2$ for $\mu\text{Light222}$. The intensity also varies between $20 \text{ }\mu\text{W/cm}^2$ and around zero for $\mu\text{Light242}$. The light intensity dropped to zero probably due to the voltage threshold of LED. In clinic, FDA has regulated the maximum peak-to-peak acoustic intensity in anywhere within the range to be 720 mW/cm^2 for diagnostic system [53]. Thermal and heating issues can be caused under a long-term high intensity ultrasonic treatment. The light intensity with reflective boundary condition was also evaluated with a hemi-sphere water tank (5 cm in diameter, 2.5 cm away from the transducer). No acoustic absorption layer was placed during this experiment. The $\mu\text{Light242}$ was selected and measured during the experiment. PIN photodiode was attached onto the surface of the LED during the experiment. The acoustic input for these experiments were changed between 0 and 720 mW/cm^2 . As shown in Figure 5.3, the generated light irradiance was much higher than the previous condition. The resultant light irradiance from $\mu\text{Light242}$ was measured to be around 1.0 mW/cm^2 at 720 mW/cm^2 .

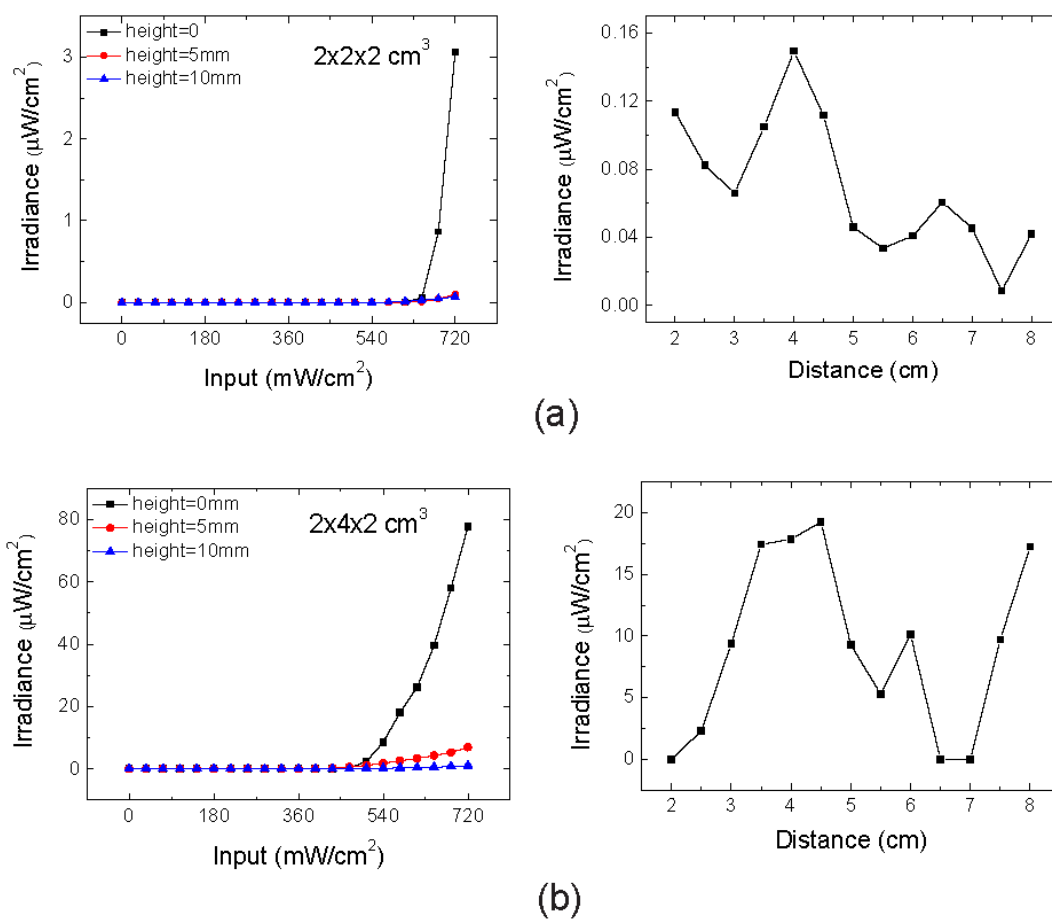


Figure 5.2 Light irradiance characterizations of μLight without reflection

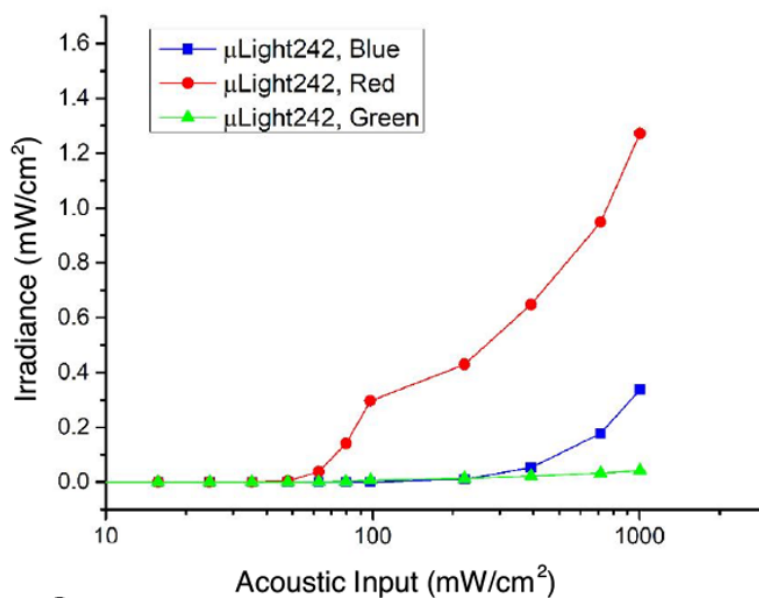


Figure 5.3 Light intensity with reflections

According to the measured light intensity and reported light dosage for several photosensitizers, a treatment time can be estimated [62], [68], [71], [83]. Table 5.2 summarizes the required treatment time when μ Light242 is implanted and assume they can be powered up at same level. After the injection of the administrated photosensitizer, different light dosages were tested to treat different types of tumors. Conventional light source has been used for most studies, such as lamp and laser optics. Another study also suggested that there is no direct relevance between efficacy and high light intensity [83]. As a result, considering one device with two red LEDs, with 20 minutes of treatment, an energy delivery of 1.3 J/cm^2 can be achieved. Thus, the treatment time using this device is not significantly longer than other conventional external light source. More importantly, the final treatment time could be shorter since the light penetration could be much lower with the external light sources. For a large tumor tissue, an implantation of multiple devices can also significantly reduce the total treatment time. A recent study has also demonstrated the feasibility of using a similar low light intensity device which can be applied for metronomic photodynamic therapy [84].

Table 5.2 Photosensitizers and estimated treatment time using μ Light [62], [68], [71], [83]

Platform	Substance	Wavelength (nm)	Concentration (mg/kg)	Light Energy (J/cm^2)	Treatment time (hours)			Target organ
					μ Light222 red	μ Light242 red	μ Light242 blue	
Porphyrin	HpD	408, 630	0.8 - 2.0	200-300	1157.4 - 1736.1	50.5 - 75.8	9.1 - 13.7	Lung, Head, Neck, Bladder
Porphyrin	ALA	410, 635	100 $\mu\text{mol/L}$	3-4	34.7 - 138.9	1.5 - 6.1	0.13 - 13.7	Head, Neck, Bladder, Prostate
Chlorine	Temoporfin	652	0.1-0.2	20	115.7	5.1	0.9	Lip, Oral, Lung, Stomach, Pancreatic
Chlorine	Talaporphin sodium	408, 664	>2.5	100	578.7	25.3	4.3	Head, Neck
Chlorine	HPPH	408, 665	2.5-6	44.4-133.2	256.9 - 770.8	11.2 - 25.3	1.9 - 5.7	Lung
Padoporfin	Phthalocyanine	670-763	-	100	578.7	25.3	4.3	Lip, Pharynx, Larynx, Tongue
Porphyrin	Verteporfin	690	-	100	578.7	25.3	4.3	Eye
Tetraphyrins	Lutetaphyrin	732	0.5 - 2	2.5-150	-	-	-	Breast

5.4.2 Ex Vivo Results

Since the previous studies used water as media for light transmission, *ex vivo* validation has also been performed using soft bovine tissue for the penetration depth of the light from μ Light, Figure 5.4. The transmitted light intensity was measured across different thicknesses of soft tissue. When penetrating 1.3 mm-thick tissue, the light was attenuated to 67% for red LED. And the degradation can be more than 50% for blue LED. This result is reasonable since the light absorption is more significant for light with lower wavelength. Thus, multiple light sources are required for a target area.

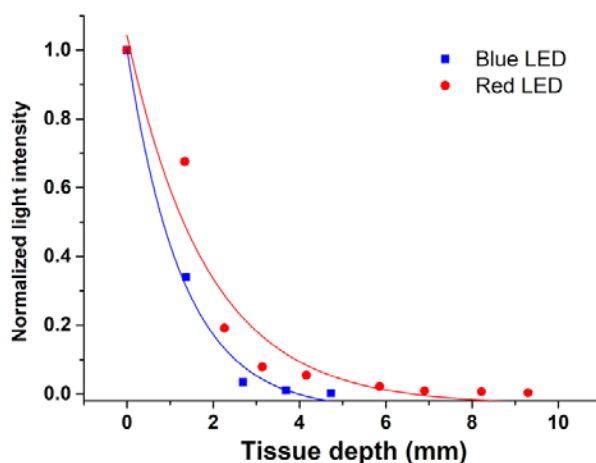


Figure 5.4 Ex vivo light penetration through bovine tissue

5.4.3 In Vitro Results

The μ Light devices were tested with cell culture experiments. The functionality of the device was firstly examined in an *in vitro* setup. Verteporfin has been selected as photosensitizer for the cell culture experiment. Its efficacy and characteristics has been studied [80]. Verteporfin has a wide range of absorption with two significant absorptions peaks at 400-450 nm and 665-685 nm [85]. Based on the previous device powering characterizations (e.g., light intensity and threshold voltage of LED), μ Light242 with red LED was tested for cytotoxicity generation test.

The cell culture media for the experiment was prepared before freshly. Since the verteporfin was not water soluble, the administration of photosensitizer was assisted with dimethyl-sulfoxide

(DMSO, Sigma Aldrich). Verteporfin (0.5 mg, Sigma Aldrich) was firstly dissolved in DMSO. The solution was then further diluted to a save concentration for the experiment.

The concentration at which the photosensitizer was not cytotoxic was firstly determined for the HeLa cells in the experiment. A critical lethal dose, 50% value (LD50) was evaluated. Cells were mixed with a gradient of concentration (2.7mM to 0.084 mM). To quantify the toxicity, CellTiter 96® Aqueous One Solution Cell Proliferation Assay (MTS) has been used following the protocol. The LD50 result was illustrated as shown in Figure 5.5. As the result, at a concentration of 4 μ M, the transition happened which labeled as the LD50 concentration for verteporfin. Thus, for all the groups with photosensitizer, 1.44 μ L of verteporfin solution was added the cell culture media to create a mixture of 1 mL, which results in a concentration of 4 μ M for verteporfin.

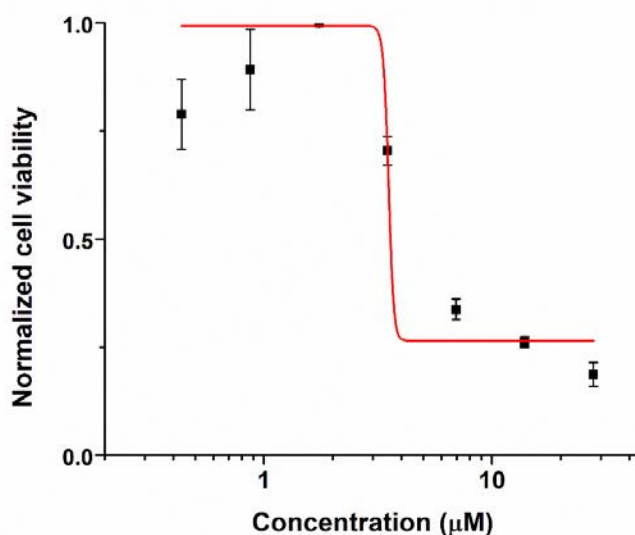


Figure 5.5 LD50 value measurement: Relative cell viability vs. verteporfin concentration

Agarose gel was prepared as tissue phantom to hold the device during the treatment. Due to the amount of water in the agarose, agarose gel has a similar acoustic property to soft tissue. Ultrasonic wave can easily travel through agarose gel and it is ideal for imitating the real tissue. TRIS/Borate/EDTA buffer solution (Fluka Analytical) was used to prepare 10% v/v. base solution. Agarose (Sigma Aldrich) was dissolved into the base solution to a concentration of 0.5% w/v. The agarose gel is molded and cooled under the room temperature.

The *in vitro* experiment setup was designed as shown in Figure 5.6a. The agarose gel phantom was placed on a PZT transducer. Two red μ Light242s (655nm) were embedded in gel under each well and powered through a distance of 3 cm-thick agarose gel.

For *in vitro* test, five different groups with different conditions were tested. For the control group, cells were mixed with only cell culture media. For the second group, cells were mixed with 1 mL cell culture media and DMSO water solution (concentration of 0.14% v/v.). For the groups with photosensitizers, 4 μ M verteporfin was added. There were two groups with photosensitizer where one of the groups will be treated with ultrasound. To show the most cytotoxic effect, Triton[®] X100 was added to the last group to kill the cells. During the experiments, all the well plates were carefully handled to avoid accidentally exposure to the ambient light. The ultrasound treatment continues for 30 minutes with an acoustic power of 185 mW/cm². The functionality of the device can be confirmed once the light was observed. Considering the treatment time and measured light intensity, the light dose for each well was calculated to be around 4 J/cm². Figure 5.6b plots the relative cell viability for all five groups. As compared to non-treated group, the photodynamic therapy with μ Light has reduce the average cell viability by around 70%. And a decrease of 82% in viability as compared to the control group. The result of *in vitro* experiment verified the feasibility of using proposed device to trigger the toxicity of the drug.

5.4.4 *In Vivo* Results

To move forward with the promising result with *in vitro* experiment, *in vivo* experiment was designed and conducted in mouse model.

For *in vivo* validation, female BALB/cJ mice (Jackson Laboratory) were selected. For each group, there were six to eight animals. As for the cancer cell lines, 4T1 cell line was selected due to its easier handling and spherical shape of the tumor. Before the implantation, one million tumor cells were implanted for each mouse. The hind flank region was selected as the target. Before the implantation surgery, the device was sterilized in 70% ethanol for 30 minutes. One μ Light242 was implanted into the tumor once the size reaches approximately 200 mm³.

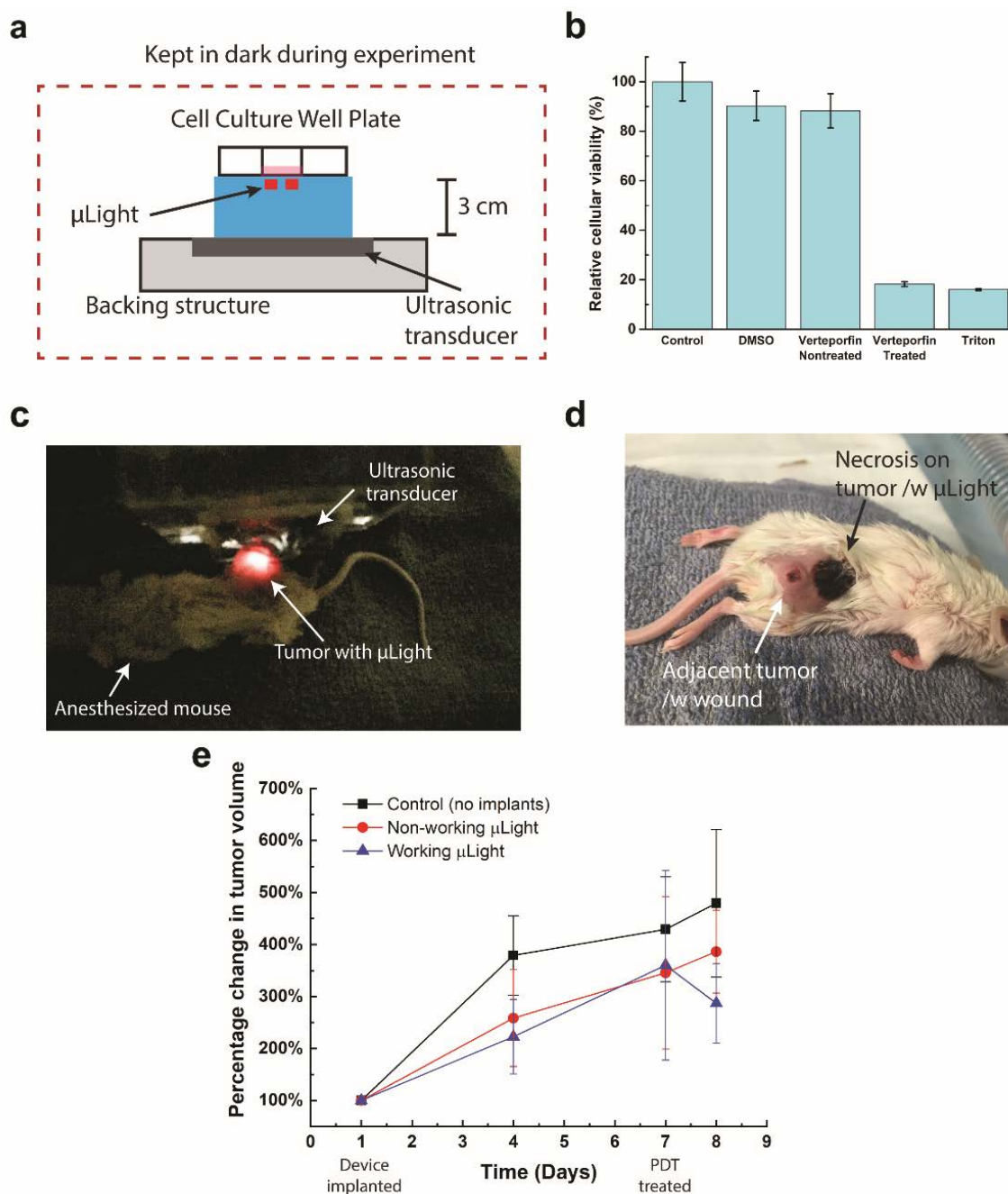


Figure 5.6 a. Experiment setup for cell culture assay, b. cytotoxicity assay of five experimental groups (control, DMSO only, photosensitizer only, photosensitizer with PDT treatment, cells killed by Triton), c. in vivo treatment with μ Light being activated using a ultrasound transducer, d. image of mouse treated with PDT (after 24 hours), e. Tumor volume change for three different groups (control, mouse with dummy device, mouse with working device).

After a week of healing, ultrasound treatment was conducted. The administration of photosensitizer starts from a dissolution of 1mg verteporfin into 0.25 mL DMSO. The DMSO solution was then diluted by 10 times. For each mouse, 25 μ L of diluted verteporfin solution was injected resulting in a dosage of 0.5mg/kg per mouse. The body temperature of the mouse was maintained on a heating pad during the treatment. After the treatment, the size of the tumors was measured for each mouse and an averaged size of the tumor was then calculated.

The process of the treatment was pictured in Figure 5.6c. For a better ultrasound transmission, hair on the treated area was shaved. Ultrasound gel was applied which can both increase the powering efficiency and reduce the heat generation associated with ultrasound vibration. Since the device was implanted near or inside the tumor, some of the device have been completely deployed inside tumor tissue due to the continuous growth of the tumor cells after the surgery. The PDT treatment was conducted on the 7th day after the surgery. Mice were divided into three groups, control group without implant and treatment, a group with implant but no treatment, and the last group with implant and treatment. To calculate the average volume of the tumor, we excluded the mice which suffered from an early death and underwent a natural healing of the cancer.

For the group with implant and ultrasound treatment, the treatment time was 30 minutes for each mouse (expecting a delivered light dose of 2 J/cm² light). During the treatment, the red light has been generated inside the mouse, Figure 5.6c. The size of the tumors were plotted in Figure 5.6e. As shown, the tumor size of the control group continuously increased over 8 days. For the group with implant and ultrasound activation, a shrinkage of the averaged tumor size can be measured to be around 20%. Along with the shrinkage, some necrotic regions were observed 24 hours after the treatment, Figure 5.6d. Since it is a result of the PDT treatment, the necrosis area was adjacent to the area where μ Light was implanted. Although further complete study is expected for a comprehensive analysis of the efficacy of the treatment, this preliminary *in vivo* result is promising and indicates the feasibility of using a wireless powered implantable light source to trigger the photo-reaction for PDT.

5.5 Conclusion

In conclusion, we reported an implantable ultrasonically powered micro light source for localized photodynamic therapy applications. Ultrasonic powering offers several advantaged including higher powering distance, less insensitive to angular alignment, and smaller form factor. The

characterizations of light irradiance have proven that the generated light intensity is sufficient for the photodynamic therapy. The small form factor of μ Light enable to be fit inside of the biopsy needle for an easy implantation. *In vivo* validation demonstrated a certain effect on the shrinkage of the tumor while using verteporfin coupled PDT with proposed device. We believe the proposed implantable micro light source, μ Light, can broaden the application of PDT to more types of cancers and even other type of disease.

6. ULTRASONICALLY POWERED MICRO-IMPLANT FOR COMBINED PHOTODYNAMIC AND ELECTROLYTIC TUMOR ABLATION

6.1 Introduction

Oxygen generated during the electrolytic ablation can be utilized to enhance photodynamic therapy efficacy through generation of reactive oxygen species (ROS). In this chapter, we have developed an ultrasonically powered micro-implant combining electrolytic ablation with a micro-light source. A rapid prototyped device and some preliminary characterizations are also presented in this chapter.

6.2 Background and System Overview

According to a recent report, over one million new cancer patients have been diagnosed in 2018, and more than 600,000 deaths are expected in the United States [86]. A few solid tumors, such as liver and pancreatic tumors, are deep-seated and cannot be safely removed surgically or called non-resectable [87]. As reported, in 2018, nearly 12% of cancer deaths were related to liver and pancreatic cancer [86]. The difficulty of surgical tumor removal mainly arises due to the concerns such as inadequate healthy liver remains, or the deterioration of health [88], [89]. There are also some other disadvantages of resection which includes the need for large incision, risk of infections, and possible morbidity due to surgery. A more advanced technique of surgery requires additional surgery resulting in increased morbidity, mortality, and healthcare cost [90], [91].

As stated in previous chapter, other cancer treatment modalities are chemotherapy and radiotherapy. Such treatments are suitable for the case where cancer cells spread, or uncontrolled systematic symptoms happens. However, the treatment can also increase the liver burden [92], [93]. Modern chemotherapy usually entails systemic or localized injection of the drug through a catheter [92]. The localized delivery of cytotoxic agents minimizes side effects. Radiotherapy features direct injection of radioactive beads into the arteries leading to the tumors [93]. Once activated, the radioactive decay of the beads over time kills the tumor. Such targeted radiotherapy decreases the side effect as compared to the conventional radiation therapy. However, these treatments still suffer from some other side effects, such as pain, nausea, and reduced immune system function.

To resolve the mentioned situations, ablation therapy is an alternative emerging technique that locally burns the tumors. Radiofrequency and microwave have been used to generate heat and kill tumor thermally [94]. These techniques usually require the insertion of a special probe or electrode into the target area using an image-guided procedure. However, some major concerns are related to the possible harm due to the localized acute energy delivery. More recently, electrochemical ablation (EA) became another promising non-thermal cancer ablation modality [95]–[99]. The efficacy of electrolytic ablation can be explained by various mechanisms such as toxic chemical species, such as ROS, direct electric current and local pH changes in the microenvironment of cancerous cells. Instead of high energy, electrolysis delivers a moderate direct current through the tissue and a production of various chemical compounds. Similarly, electrochemical therapy with a series of short DC pulses has also been reported [100], [101]. Despite definite advantages offered by electrochemical therapy, the need of inserting needle-like electrodes into the tumor hampers its application where direct insertion of electrode is not easily accessible. An implantable micro-ablator that is ultrasonically-powered can be a way to resolve this limitation. As demonstrated previous, ultrasound can achieve higher power density as compared to inductive powering for the receiver size [21], [61]. In addition, there are some other advantages including a deeper transmission depth (a few cm) and higher tolerance to angular misalignment (requires accurate alignment of the transmitter and the receiver) [26], [36], [39], [47], [102], [103].

In addition to electrolytic ablation, PDT, as introduced in the previous chapter, is another treatment modality that uses a combination of cytotoxic drugs and light to kill the tumor cells through the generation of cytotoxic agents and reactive oxygen species (ROS) as described in the previous chapter. As the by-product of electrolytic ablation, e.g. electrolysis, oxygen can be used for the reaction of photosensitizer, Figure 5.1a, to enhance the efficacy of PDT. In this paper, we combine the electrolytic ablation with PDT in the form of an ultrasonically powered micro-implant an on-board micro-light-source.

6.2.1 Circuit Schematic

The circuit system of the device is depicted in Figure 6.1. Lead titanate zirconate (PZT) is used as the piezoelectric material for energy conversion. Ultrasonic waves are launched by the transmitter to power the implant and generate enough energy to perform EA and PDT. A full-bridge rectifier

is connected to a shunt capacitor for voltage conditioning. 2 LEDs (655nm) are connected in series to escalate forward bias voltage above the threshold for electrolysis.

6.2.2 System Operation

Figure 6.1 shows a schematic of the device being implanted in a pancreatic tumor. During the operation, ultrasonic wave is excited from the outside and being transmitted into the body with the help of ultrasound gel. Prior to the ultrasound treatment, photosensitizer needs to be injected systematically for intratumorally (green particle in Figure 6.1). Once ultrasound strikes the device, PZT element can convert the vibration into electric voltage. The generated electricity is divided into electrodes and LEDs. Due to the forward bias characteristics of LEDs, two LEDs are required to maintain sufficient voltage drop for the electrolysis across the electrodes. The generated oxygen is then converted into reactive oxygen species by the photosensitizer.

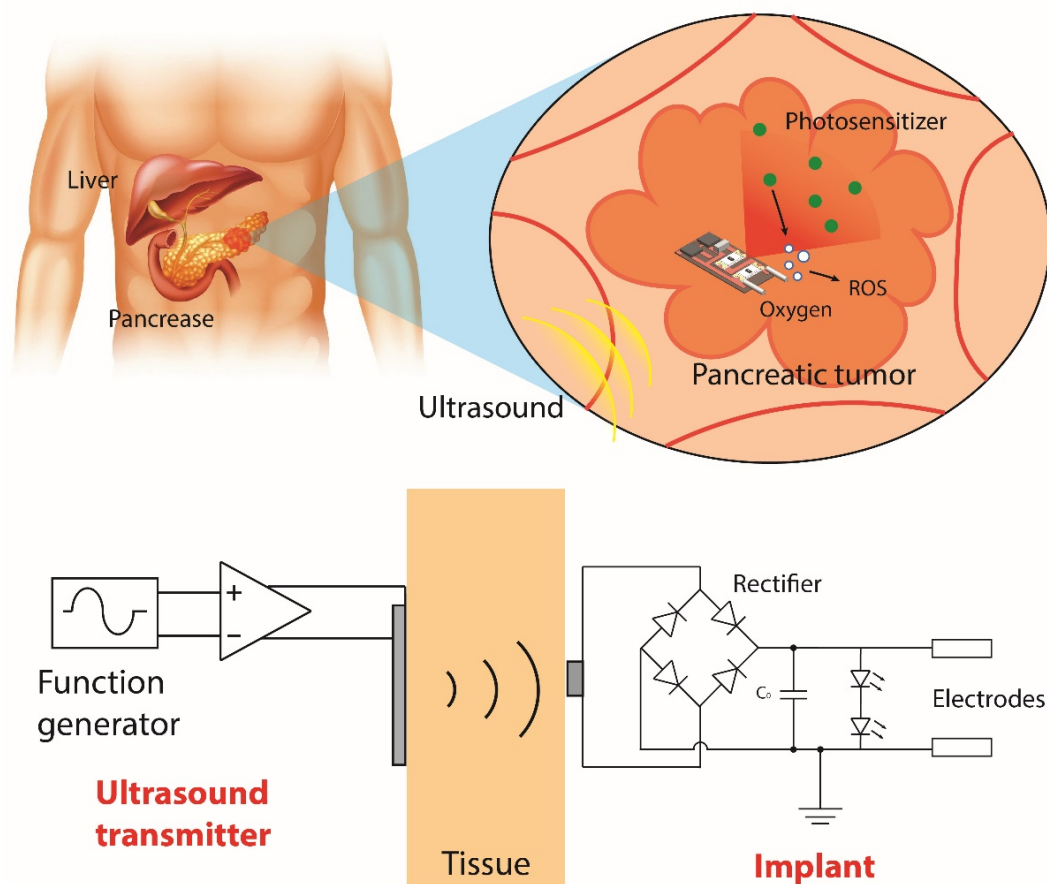


Figure 6.1 Schematic of the combined EA-PDT system.

6.3 Fabrication

The fabrication of the device started from patterning circuit trace on copper clad polyimide (Pyrallux®), followed by components assembly and soldering, Figure 6.2(a). The PZT disk was diced into desired dimension ($1 \times 1 \times 5 \text{ mm}^3$) before assembly. Next, all the components were sequentially soldered onto the substrate. The surface mounted components and PZT were designed to be placed on two different sides. Finally, the whole device was passivated with $5 \mu\text{m}$ thick Parylene-C coating. The tip of the electrode (1-2 mm long) was not coating. The fabricated prototype device is shown in Figure 6.2(b). More PZTs and LEDs can be integrated into the design to increase the total power output.

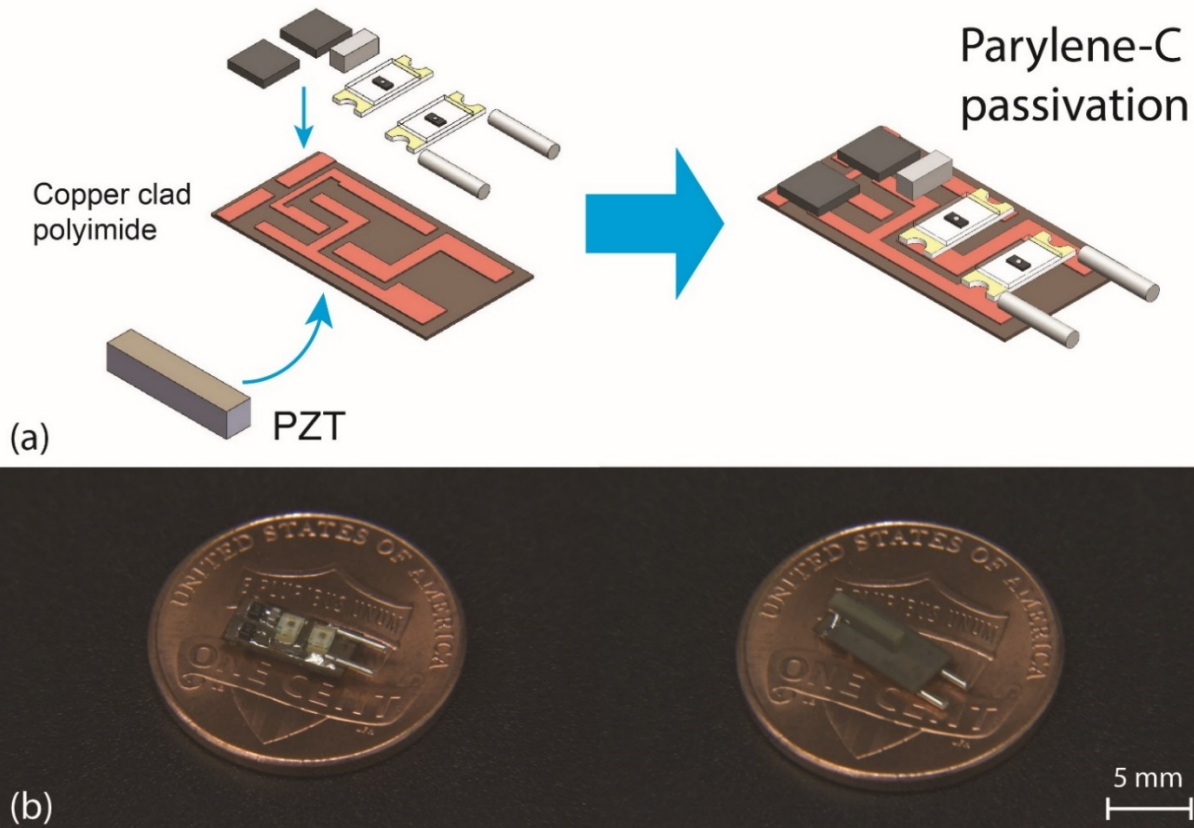


Figure 6.2 (a) Fabrication process of micro-implant on a double-sided copper-clad flexible substrate. (b) Photographs of front and back side of fabricated device.

6.4 Experimental Results

For the validation of the device, performance for electrolysis and light generation have been tested in different conditions. To examine the functionality of electrolytic ablation, localized pH change

was monitored by a needle type pH sensor in soft tissue phantom. In addition to the electrolysis measurement, generated voltage, current and lighting intensity were also evaluated for photodynamic therapy. At least, generated oxygen has also been observed as a proof-of-concept result before any further studies in the future.

6.4.1 Induced pH Change

The change of pH during electrolysis was quantified with a needle-type pH probe while the device was embedded within a 2.5cm-thick 1% w/v agarose gel as tissue phantom, Figure 6.3(a).

Agarose gel was prepared firstly as tissue phantom to house the electrodes and served as media with electrolyte for the electrolysis. Agarose gel was selected due to its similar mechanical property to the soft tissue. Agarose was dissolved in the buffer solution at a temperature around 100 °C to acquire a concentration of 1.0% w/v. The agarose gel can be degassed during the heating. Thus, no more degassing was conducted for this experiment. The degassed pre-gel solution was poured into well plates and cooled over time.

During the experiment, the current flowing through the electrodes was measured to be around 150 μ A. Figure 6.3(b) shows the change of pH in the phantom gel over time at distances of 3 mm and 5 mm away from both cathode and anode. pH value increased at the cathode and decreased at the anode within several minutes of treatment. As a result, on the cathode, the pH value can be increased from 7 to 10 within 150s. And around anode, the pH value decreases from 7 to 3 within 200s. At 5 mm distance, the change of pH was delayed as compared to the case of 3 mm, which is because of the diffusion of the ions to the probes. Moreover, the pH change was also delayed for cathode due to the lower diffusion coefficient for OH ion.

Such localized pH change can be cytotoxic to cells. Increase number of ions could also possibly increase the conductivity of the electricity which in turn increase the overall efficacy of the electrolytic ablation.

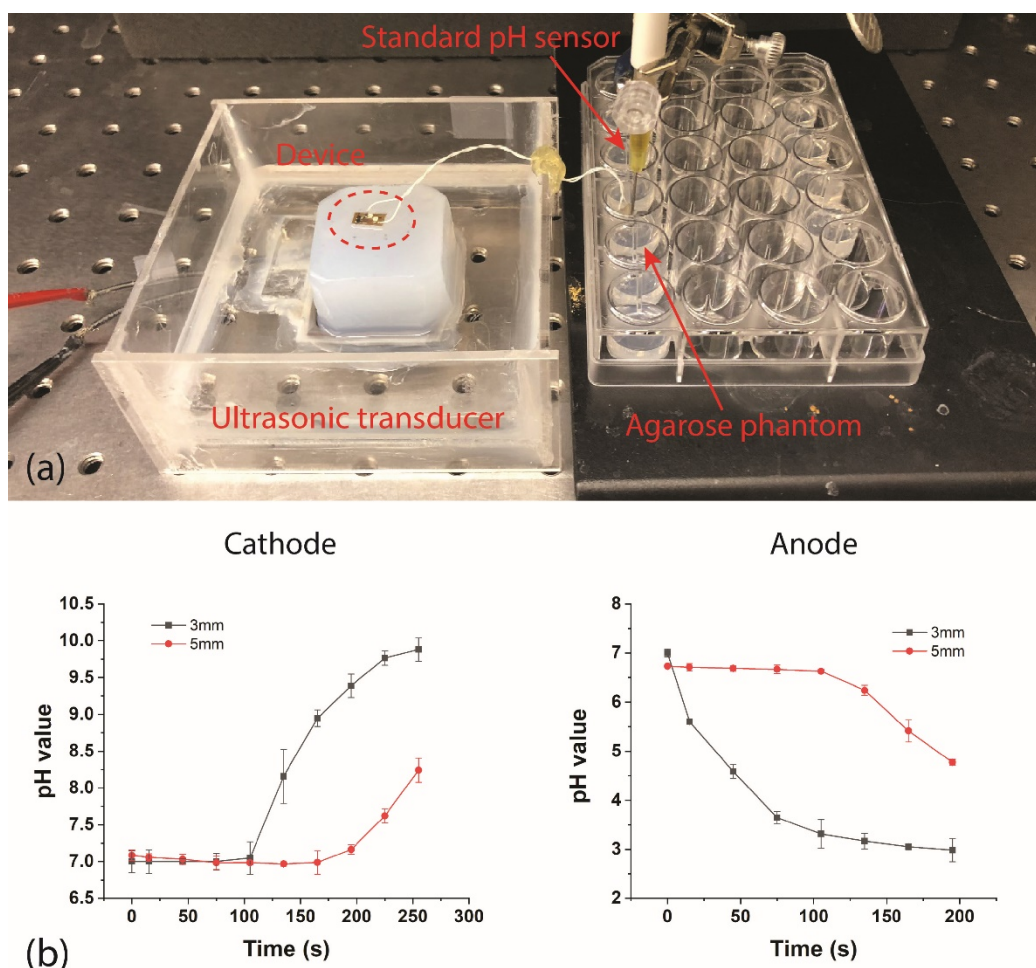


Figure 6.3 (a) Characterization setup for ultrasonic powering and pH measurement. (b) pH changes over time at various locations around the electrodes.

6.4.2 Light and Electrical Output Evaluation

The voltage across electrolytic electrodes was then measured under different ultrasonic intensities, Figure 6.4. A hydrophone was used to evaluate the acoustic intensity. The output voltage can be maintained at a level of $\sim 3.2\text{V}$ when the acoustic intensity was higher than $300\text{mW}/\text{cm}^2$. It is important to note that the FDA limit for the ultrasound intensity for diagnostic system is $720\text{mW}/\text{cm}^2$. The light intensity was measured by a PIN photodiode attached to the surface of the LED. Two LEDs were measured at the same time for a total generated light intensity. The result shows an increase in irradiance and voltage with the rise of input power. The irradiance was $33\mu\text{W}/\text{cm}^2$ at an acoustic input of $438\text{mW}/\text{cm}^2$.

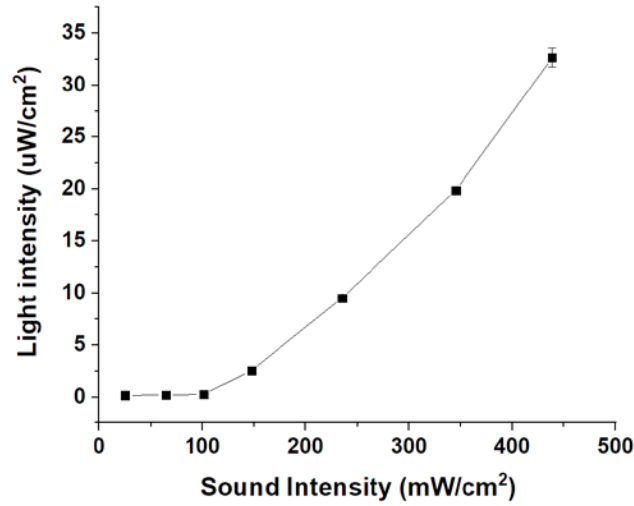


Figure 6.4 Light intensity under various acoustic inputs.

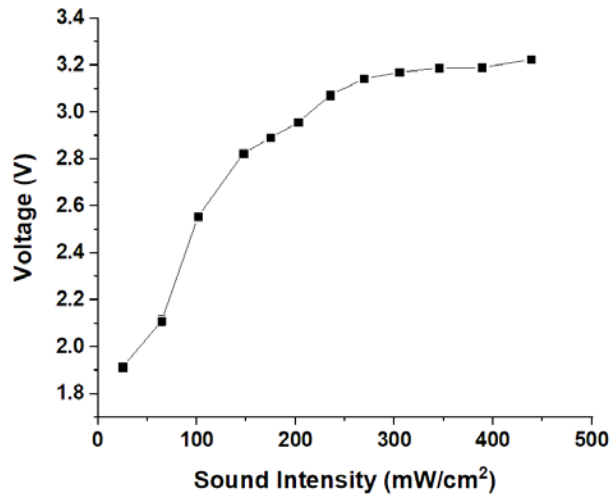


Figure 6.5 Output voltage across electrodes under various acoustic inputs.

The generated voltage was also monitored with multimeter and plotted on Figure 6.5. As shown, once the sound intensity increases above certain level ($\sim 100 \text{ mW/cm}^2$), LEDs were turned on and the output voltage jumped up to around 3 V and gradually increase to 3.2 V. Once the voltage reaches 3.2 V, the output voltage slightly changes because of the property of LED p-n junction. Thus, the output voltage can be stabilized regardless of the input acoustic intensity which is desirable for safety concerns.

6.4.3 Oxygen Generation

The change of the oxygen concentration was also measured using a setup similar to Figure 6.3a. Oxygen generation was tested when electrodes were placed in 2mL 0.9% NaCl solution. During the experiment, the treatment was conducted for 5 minutes and turned off for oxygen monitoring for another 5 minutes. The dissolved oxygen concentration was measured using an optic oxygen probe. The measured result was plotted in Figure 6.6. After every 5-minute treatment, the oxygen concentration increased by around 0.25mg/L. The generated oxygen bubbles can also be observed at the tip of the electrodes.

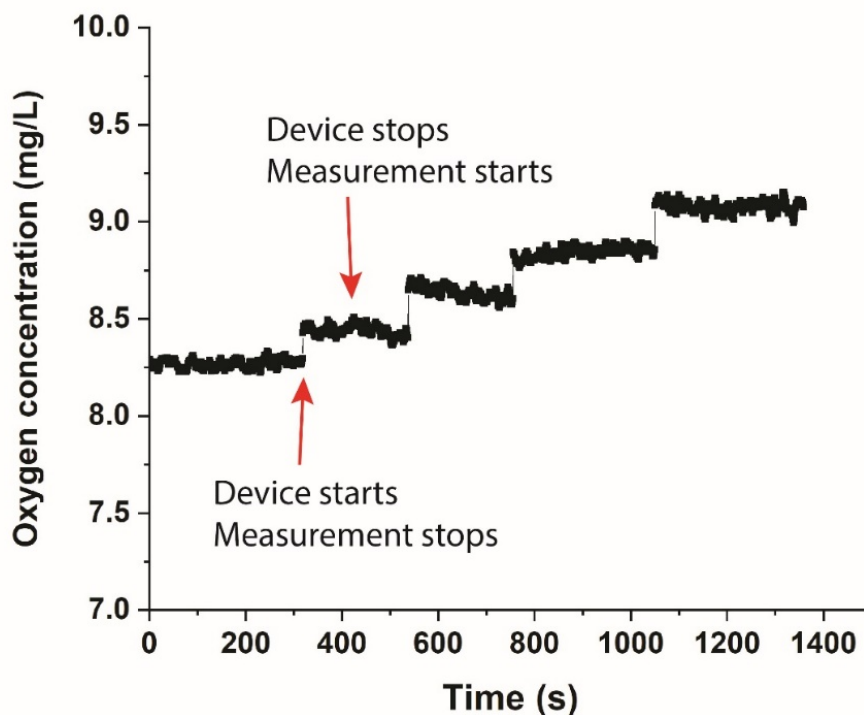


Figure 6.6 Dissolved oxygen concentration increases over time in 0.9% wt. NaCl solution. A continuous 5-minute monitoring of oxygen concentration was taken after every 5 minutes of treatment.

6.5 Conclusion

In this chapter, a device with both light source and electrolytic ablator integrated has been presented. The small form factor, multi-mechanism, and easy implantation are the advantages offered by this design. To verify the functionality of the device, localized pH change, light

irradiance rating and oxygen concentration change were evaluated. As a result, generated light intensity, pH changes and oxygen generation were observed. Although further validation is expected for the efficacy of the treatment, the device is promising and firstly enables the combination of electrolytic ablation with photodynamic therapy for un-resectable tumors.

REFERENCES

- [1] P. M. Zoll, "Resuscitation of the heart in ventricular standstill by external electric stimulation," *N. Engl. J. Med.*, vol. 247, no. 20, pp. 768–771, 1952.
- [2] E. Regar, G. Sianos, and P. W. Serruys, "Stent development and local drug delivery," *British Medical Bulletin*, vol. 59, pp. 227–248, 2001.
- [3] W. Greatbatch and C. F. Holmes, "History of implantable devices," *IEEE Eng. Med. Biol. Mag.*, vol. 10, no. 3, p. 38–41+49, 1991.
- [4] J. Garbade, H. B. Bittner, M. J. Barten, and F.-W. Mohr, "Current trends in implantable left ventricular assist devices.," *Cardiol. Res. Pract.*, vol. 2011, p. 290561, 2011.
- [5] R. Magjarevic and B. Ferek-Petric, "Implantable Cardiac Pacemakers-50 Years from the First Implantation," *Zdr. Vestnik-Slovenian Med. J.*, vol. 79, pp. 55–67, 2010.
- [6] H. Beck, W. E. Boden, S. Patibandla, D. Kireyev, V. Gutpa, F. Campagna, M. E. Cain, and J. E. Marine, "50th Anniversary of the first successful permanent pacemaker implantation in the United States: historical review and future directions.," *Am. J. Cardiol.*, vol. 106, no. 6, pp. 810–818, 2010.
- [7] K. Rajappan, "Permanent pacemaker implantation technique: part II.," *Heart*, vol. 95, no. 4, pp. 334–342, 2009.
- [8] S. Furman, "Early history of cardiac pacing and defibrillation," *Indian Pacing Electrophysiol. J.*, vol. 2, no. 1, pp. 2–3, 2002.
- [9] P. R. Kileny, S. Zimmerman-Phillips, J. L. Kemink, and S. P. Schmaltz, "Effects of preoperative electrical stimulability and historical factors on performance with multichannel cochlear implant," *Ann Otol Rhinol Laryngol*, vol. 100, no. 7, pp. 563–568, 1991.
- [10] S. J. A. Majerus, P. C. Fletter, M. S. Damaser, and S. L. Garverick, "Low-power wireless micromanometer system for acute and chronic bladder-pressure monitoring," *IEEE Trans. Biomed. Eng.*, vol. 58, no. 3 PART 2, pp. 763–767, 2011.
- [11] Y.-H. Joung, "Development of Implantable Medical Devices: From an Engineering Perspective," *Int. Neurol. J.*, vol. 17, no. 3, p. 98, 2013.
- [12] X. Wei and J. Liu, "Power sources and electrical recharging strategies for implantable medical devices," *Front. Energy Power Eng. China*, vol. 2, no. 1, pp. 1–13, 2008.

- [13] K. Zhang, J.X. and Hoshino, *Molecular Sensors and Nanodevices: Principles, Designs and Applications in Biomedical Engineering*. Academic press, 2018.
- [14] J. R. Moser and A. A. Schneider, "Primary cells and iodine containing cathodes therefor," 1972.
- [15] D. C. Bock, A. C. Marschilok, K. J. Takeuchi, and E. S. Takeuchi, "Batteries used to power implantable biomedical devices," *Electrochim. Acta*, vol. 84, no. 1, pp. 155–164, Dec. 2012.
- [16] P. Ritter, G. Z. Duray, S. Zhang, C. Narasimhan, K. Soejima, R. Omar, V. Laager, K. Stromberg, E. Williams, and D. Reynolds, "The rationale and design of the Micra Transcatheter Pacing Study: Safety and efficacy of a novel miniaturized pacemaker," *Europace*, vol. 17, no. 5, pp. 807–813, 2015.
- [17] M. Preminger and S. Mittal, "Value of EP study and other cardiac investigations," *Card. Electrophysiol. Clin.*, vol. 5, no. 4, pp. 413–421, 2013.
- [18] M. L. Hsia, Y. S. Tsai, and O. T. C. Chen, "An UHF passive RFID transponder using a low-power clock generator without passive components," in *Midwest Symposium on Circuits and Systems*, 2006, vol. 2, pp. 11–15.
- [19] C. Sauer, M. Stanaćević, G. Cauwenberghs, and N. Thakor, "Power harvesting and telemetry in CMOS for implanted devices," *IEEE Trans. Circuits Syst. I Regul. Pap.*, vol. 52, no. 12, pp. 2605–2613, 2005.
- [20] Ping Si, a P. Hu, S. Malpas, and D. Budgett, "A frequency control method for regulating wireless power to implantable devices.," *Biomed. circuits Syst.*, vol. 2, no. 1, pp. 22–9, 2008.
- [21] A. Denisov and E. Yeatman, "Ultrasonic vs. Inductive Power Delivery for Miniature Biomedical Implants," *2010 Int. Conf. Body Sens. Networks*, pp. 84–89, Jun. 2010.
- [22] W. S. Lee, A. Kim, B. Ziaie, V. Raghunathan, and C. R. Powell, "UP-link: An ultra-low power implantable wireless system for long-term ambulatory urodynamics," *IEEE 2014 Biomed. Circuits Syst. Conf. BioCAS 2014 - Proc.*, pp. 384–387, 2014.
- [23] A. Santić, S. Vamvakas, and M. R. Neuman, "Micropower electronic switches for implanted instrumentation.," *IEEE Trans. Biomed. Eng.*, vol. 29, no. 8, pp. 583–589, 1982.
- [24] H. V Allen and J. W. Knutti, "A Fully Integrated RF Actuated Battery Controller," *Solid-State Circuits Conf. Dig. Tech. Pap. 1981 IEEE Int. IEEE*, vol. 24, pp. 166–167, 1981.
- [25] P. J. Larson and B. C. Towe, "Miniature ultrasonically powered wireless nerve cuff stimulator," in *2011 5th International IEEE/EMBS Conference on Neural Engineering*,

- NER 2011*, 2011, pp. 265–268.
- [26] T. Maleki, N. Cao, S. H. Song, C. Kao, S.-C. A. Ko, and B. Ziaie, “An ultrasonically powered implantable micro-oxygen generator (IMOG).,” *IEEE Trans. Biomed. Eng.*, vol. 58, no. 11, pp. 3104–11, Nov. 2011.
 - [27] D. J. Young, P. Cong, M. a. Suster, N. Chimanonart, and W. H. Ko, “Wireless power recharging for implantable bladder pressure chronic monitoring,” *2010 IEEE 5th Int. Conf. Nano/Micro Eng. Mol. Syst. NEMS 2010*, pp. 604–607, 2010.
 - [28] S. D. O’Driscoll, “A mm-sized implantable power receiver with adaptive matching,” *Proc. IEEE Sensors*, no. 2, pp. 83–88, 2010.
 - [29] F. Zhang, X. Liu, S. a. Hackworth, R. J. Scwabassi, and M. Sun, “In vitro and in vivo studies on wireless powering of medical sensors and implantable devices,” *2009 IEEE/NIH Life Sci. Syst. Appl. Work. LiSSA 2009*, pp. 84–87, 2009.
 - [30] P. Si, A. P. Hu, J. W. Hsu, M. Chiang, Y. Wang, S. Malpas, and D. Budgett, “Wireless Power Supply for Implantable Biomedical Device Based on Primary Input Voltage Regulation,” *Ind. Electron. Appl. 2007. ICIEA 2007. 2nd IEEE Conf.*, pp. 235–239, 2007.
 - [31] M. a Hannan, S. Mutashar, S. a Samad, and A. Hussain, “Energy harvesting for the implantable biomedical devices: issues and challenges.,” *Biomed. Eng. Online*, vol. 13, no. 1, p. 79, 2014.
 - [32] A. M. Sodagar and P. Amiri, “Capacitive coupling for power and data telemetry to implantable biomedical microsystems,” *2009 4th Int. IEEE/EMBS Conf. Neural Eng. NER ’09*, pp. 411–414, 2009.
 - [33] K Goto;T Nakagawa;O Nakamura;S Kawata, “An implantable power supply with an optically rechargeable lithium battery,” *IEEE Trans. Biomed. Eng.*, vol. 48, no. 7, pp. 830–833, 2001.
 - [34] M. Khan, J. M. Islamia, and S. Iqbal, “SPICE simulation of implantable solar power supply for sustainable operation of cardiac biosensors SPICE simulation of implantable solar power supply for sustainable operation of cardiac biosensors Munna Khan and Ajai Kumar Singh * Syed Shakir Iqbal,” no. June 2016, 2015.
 - [35] R. Bansal, *Ultrasound for Surgeons*, vol. 45, no. 6. 1997.
 - [36] S. H. Song, A. Kim, and B. Ziaie, “Omnidirectional ultrasonic powering for millimeter-scale implantable devices,” *IEEE Trans. Biomed. Eng.*, vol. 62, no. 11, pp. 2717–2723, 2015.

- [37] W. B. Phillips, B. C. Towe, and P. J. Larson, "An ultrasonically-driven piezoelectric neural stimulator," *Proc. 25th Annu. Int. Conf. IEEE Eng. Med. Biol. Soc. (IEEE Cat. No.03CH37439)*, vol. 2, pp. 1983–1986, 2003.
- [38] Y. Zhu, S. O. R. Moheimani, S. Member, and M. R. Yuce, "Ultrasonic Energy Transmission and Conversion Using a 2-D MEMS Resonator," no. April, pp. 374–376, 2010.
- [39] J. Zhou, A. Kim, S. H. Song, and B. Ziaie, "An Ultrasonically Powered Implantable Micro-Light Source for Localized Photodynamic Therapy," *2015 Transducers - 2015 18th Int. Conf. Solid-State Sensors, Actuators Microsystems*, pp. 876–879, 2015.
- [40] S. S. Rao and M. Sunar, "Piezoelectricity and its use in disturbance sensing and control of flexible structures - A survey," *Appl. Mech. Rev.*, vol. 47, no. 4, pp. 113–124, 1994.
- [41] J. Sirohi and I. Chopra, "Fundamental Understanding of Piezoelectric Strain Sensors," *J. Intell. Mater. Syst. Struct.*, vol. 11, no. 4, pp. 246–257, 2000.
- [42] H. S. Kim, J. H. Kim, and J. Kim, "A review of piezoelectric energy harvesting based on vibration," *Int. J. Precis. Eng. Manuf.*, vol. 12, no. 6, pp. 1129–1141, 2011.
- [43] S. J. Jeong, D. S. Lee, M. S. Kim, D. H. Im, I. S. Kim, and K. H. Cho, "Properties of piezoelectric ceramic with textured structure for energy harvesting," in *Ceramics International*, 2012, vol. 38, no. SUPPL. 1.
- [44] R. Elfrink, T. M. Kamel, M. Goedbloed, S. Matova, D. Hohlfeld, Y. van Andel, and R. van Schaijk, "Vibration energy harvesting with aluminum nitride-based piezoelectric devices," *J. Micromechanics Microengineering*, vol. 19, no. 9, p. 094005, 2009.
- [45] C. M. T. Tien and N. S. Goo, "Use of a Piezocomposite Generating Element in Energy Harvesting," *J. Intell. Mater. Syst. Struct.*, vol. 21, no. 14, pp. 1427–1436, 2010.
- [46] D. Seo, J. M. Carmena, J. M. Rabaey, E. Alon, and M. M. Maharbiz, "Neural Dust: An Ultrasonic, Low Power Solution for Chronic Brain-Machine Interfaces," *arXiv.org*, vol. q-NC, no. April, 2013.
- [47] J. Zhou, A. Kim, and B. Ziaie, "An ultrasonically controlled switching system for power management in implantable devices," *Biomed. Microdevices*, vol. 20, no. 2, p. 42, 2018.
- [48] R. Krimholtz, D. A. Leedom, and G. L. Matthaei, "New Equivalent Circuits for Elementary Piezoelectric Transducers," *Electron. Lett.*, vol. 6, no. 13, pp. 398–399, 1970.
- [49] R. Holland, "Resonant properties of piezoelectric ceramic rectangular parallelepipeds," *J. Acoust. Soc. Am.*, vol. 43, no. 5, pp. 988–997, 1968.

- [50] H. Azhari, *Basics of Biomedical Ultrasound for Engineers*. 2010.
- [51] K. B. Ocheltree and L. A. Frizzell, "Sound Field Calculation for Rectangular Sources," vol. 36, no. 2, pp. 242–248, 1989.
- [52] S. Ozeri and D. Shmilovitz, "Ultrasonic transcutaneous energy transfer for powering implanted devices.," *Ultrasonics*, vol. 50, no. 6, pp. 556–66, May 2010.
- [53] G. Harris and H. Services, "Guidance for Industry and FDA Staff Information for Manufacturers Seeking Marketing Clearance of Diagnostic Ultrasound Systems and Transducers," 2008.
- [54] D. S. Lin, X. Zhuang, S. H. Wong, M. Kupnik, and B. T. Khuri-Yakub, "Encapsulation of capacitive micromachined ultrasonic transducers using viscoelastic polymer," *J. Microelectromechanical Syst.*, vol. 19, no. 6, pp. 1341–1351, 2010.
- [55] D. Seo, R. M. Neely, K. Shen, U. Singhal, E. Alon, J. M. Rabaey, J. M. Carmenta, and M. M. Maharbiz, "Wireless Recording in the Peripheral Nervous System with Ultrasonic Neural Dust," *Neuron*, vol. 91, no. 3, pp. 529–539, 2016.
- [56] C. Bruneel and J. Assaad, "Matching ultrasonic transducer using two matching layers where one of them is glue," vol. 37, pp. 591–596, 2004.
- [57] S. Sivashankar, S. Agambayev, U. Buttner, K. N. Salama, and A. Samples, "Characterization of Solid UV Curable 3D Printer Resins for Biological Applications," pp. 17–20, 2016.
- [58] J. Zhou, A. Kim, and B. Ziaie, "An ultrasonically controlled power management system for implantable biomedical devices," *IEEE Biomed. Circuits Syst. Conf. Eng. Heal. Minds Able Bodies, BioCAS 2015 - Proc.*, pp. 1–4, 2015.
- [59] S. Iskandar, M. Reddy, M. Lavu, M. Atoui, M. Vodapally, R. Neerumalla, M. Molugu, R. Swarna, Q. Javed, K. Gangu, and A. Gone, "Real World Experience With Medtronic Reveal LINQ," *Circulation*, vol. 134, no. Suppl 1, p. A16029, 2016.
- [60] A. Arbabian, T. C. Chang, M. L. Wang, J. Charthad, S. Baltsavias, M. Fallahpour, and M. J. Weber, "Sound Technologies, Sound Bodies: Medical Implants with Ultrasonic Links," *IEEE Microw. Mag.*, vol. 17, no. 12, pp. 39–54, Dec. 2016.
- [61] H. Basaeri, D. B. Christensen, and S. Roundy, "A Review of Acoustic Power Transfer for Bio-Medical Implants," *Smart Mater. Struct.*, vol. 25, no. 12, pp. 1–23, 2016.
- [62] A. Kim, J. Zhou, S. Samaddar, S. H. Song, B. D. Elzey, D. H. Thompson, and B. Ziaie, "An

- Implantable Ultrasonically-Powered Micro-Light-Source (μ Light) for Photodynamic Therapy,” *Sci. Rep.*, vol. 9, no. 1, p. 1395, 2019.
- [63] R. T. Skeel and S. N. Khelif, *Handbook of Cancer Chemotherapy*. 2011.
- [64] C. Sawyers, “Targeted cancer therapy,” *Nature*, vol. 432, no. 7015, pp. 294–297, 2004.
- [65] W. K. Decker, R. F. da Silva, M. H. Sanabria, L. S. Angelo, F. Guimarães, B. M. Burt, F. Kheradmand, and S. Paust, “Cancer immunotherapy: historical perspective of a clinical revolution and emerging preclinical animal models,” *Front. Immunol.*, vol. 8, p. 829, 2017.
- [66] I. J. Macdonald and T. J. Dougherty, “Basic principles of photodynamic therapy,” *J. Porphyrins Phthalocyanines*, vol. 05, no. 02, pp. 105–129, Feb. 2001.
- [67] P. Agostinis, K. Berg, K. A. Cengel, T. H. Foster, A. W. Girotti, S. O. Gollnick, S. M. Hahn, M. R. Hamblin, A. Juzeniene, and D. Kessel, “Photodynamic therapy of cancer: an update,” *CA. Cancer J. Clin.*, vol. 61, no. 4, pp. 250–281, 2011.
- [68] R. R. Allison and C. H. Sibata, “Oncologic photodynamic therapy photosensitizers: a clinical review,” *Photodiagnosis Photodyn. Ther.*, vol. 7, no. 2, pp. 61–75, Jun. 2010.
- [69] K. Plaetzer, B. Krammer, J. Berlanda, F. Berr, and T. Kiesslich, “Photophysics and photochemistry of photodynamic therapy: Fundamental aspects,” *Lasers Med. Sci.*, vol. 24, no. 2, pp. 259–268, 2009.
- [70] J. Moan and K. Berg, “The photodegradation of porphyrins in cells can be used to estimate the lifetime of singlet oxygen,” *Photochem. Photobiol.*, vol. 53, no. 4, pp. 549–553, 1991.
- [71] T. S. Mang, “Lasers and light sources for PDT: past, present and future,” *Photodiagnosis Photodyn. Ther.*, vol. 1, no. 1, pp. 43–8, May 2004.
- [72] R. A. Lustig, T. J. Vogl, D. Fromm, R. Cuenca, R. A. Hsi, A. K. D’Cruz, Z. Krajina, M. Turić, A. Singhal, and J. C. Chen, “A multicenter phase I safety study of intratumoral photoactivation of talaporfin sodium in patients with refractory solid tumors,” *Cancer*, vol. 98, no. 8, pp. 1767–1771, 2003.
- [73] J. Chen, L. Keltner, J. Christophersen, F. Zheng, M. Krouse, A. Singhal, and S. S. Wang, “New technology for deep light distribution in tissue for phototherapy,” *Cancer J.*, vol. 8, no. 2, pp. 154–163, 2002.
- [74] A. Bansal, F. Yang, T. Xi, Y. Zhang, and J. S. Ho, “In vivo wireless photonic photodynamic therapy,” *Proc. Natl. Acad. Sci.*, p. 201717552, 2018.
- [75] K. Yamagishi, I. Kirino, I. Takahashi, H. Amano, S. Takeoka, Y. Morimoto, and T. Fujie,

- “Tissue-adhesive wirelessly powered optoelectronic device for metronomic photodynamic cancer therapy,” *Nat. Biomed. Eng.*
- [76] G. Shafirstein, D. Bellnier, E. Oakley, S. Hamilton, M. Potasek, K. Beeson, and E. Parilov, “Interstitial photodynamic therapy—a focused review,” *Cancers (Basel)*, vol. 9, no. 2, p. 12, 2017.
 - [77] E. Oakley, B. Wrazen, D. A. Bellnier, Y. Syed, H. Arshad, and G. Shafirstein, “A new finite element approach for near real-time simulation of light propagation in locally advanced head and neck tumors,” *Lasers Surg. Med.*, vol. 47, no. 1, pp. 60–67, 2015.
 - [78] M. Kulik, C. Nedelcu, F. Martin, S. Lebdaï, M. C. Rousselet, A. R. Azzouzi, and C. Aubé, “Post-treatment MRI aspects of photodynamic therapy for prostate cancer,” *Insights Imaging*, vol. 5, no. 6, pp. 697–713, 2014.
 - [79] J. Swartling, J. Axelsson, G. Ahlgren, K. M. Kälkner, S. Nilsson, S. Svanberg, K. Svanberg, and S. Andersson-Engels, “System for interstitial photodynamic therapy with online dosimetry: first clinical experiences of prostate cancer,” *J. Biomed. Opt.*, vol. 15, no. 5, p. 58003, 2010.
 - [80] M. T. Huggett, M. Jermyn, A. Gillams, R. Illing, S. Mosse, M. Novelli, E. Kent, S. G. Bown, T. Hasan, B. W. Pogue, and S. P. Pereira, “Phase I/II study of verteporfin photodynamic therapy in locally advanced pancreatic cancer,” *Br. J. Cancer*, vol. 110, no. 7, pp. 1698–704, 2014.
 - [81] L. Lamsam, E. Johnson, I. D. Connolly, M. Wintermark, and M. H. Gephart, “A review of potential applications of MR-guided focused ultrasound for targeting brain tumor therapy,” *Neurosurg Focus*, vol. 44, no. February, pp. 1–7, 2018.
 - [82] R. Krimholtz, D. Leedom, and G. Matthaei, “Erratum: New equivalent circuits for elementary piezoelectric transducers,” *Electronics Letters*, vol. 6, no. 17, p. 560, 1970.
 - [83] P. Babilas, E. Kohl, T. Maisch, H. Bäcker, B. Gross, a L. Branzan, W. Bäuml, M. Landthaler, S. Karrer, and R.-M. Szeimies, “In vitro and in vivo comparison of two different light sources for topical photodynamic therapy,” *Br. J. Dermatol.*, vol. 154, no. 4, pp. 712–8, Apr. 2006.
 - [84] K. Yamagishi, I. Kirino, I. Takahashi, H. Amano, S. Takeoka, Y. Morimoto, and T. Fujie, “Tissue-adhesive wirelessly powered optoelectronic device for metronomic photodynamic cancer therapy,” *Nature Biomedical Engineering*, pp. 1–10, 2018.

- [85] U. Schmidt-Erfurth and T. Hasan, "Mechanisms of action of photodynamic therapy with verteporfin for the treatment of age-related macular degeneration.," *Surv. Ophthalmol.*, vol. 45, no. 3, pp. 195–214, 2000.
- [86] A. Noone, N. Howlader, M. Krapcho, D. Miller, A. Brest, M. Yu, J. Ruhl, Z. Tatalovich, A. Mariotto, D. Lewis, H. Chen, E. Feuer, and K. Cronin, "SEER Cancer Statistics Review, 1975-2015," Bethesda, MD, 2017.
- [87] R. L. Siegel, K. D. Miller, and A. Jemal, "Cancer statistics, 2018," *CA. Cancer J. Clin.*, vol. 68, no. 1, pp. 7–30, 2018.
- [88] J. Dou, P. Liang, and J. Yu, "Microwave ablation for liver tumors," *Abdom. Radiol.*, vol. 41, no. 4, pp. 650–658, 2016.
- [89] G. Carrafiello, D. Laganà, M. Mangini, F. Fontana, G. Dionigi, L. Boni, F. Rovera, S. Cuffari, and C. Fugazzola, "Microwave tumors ablation: Principles, clinical applications and review of preliminary experiences," *Int. J. Surg.*, vol. 6, no. SUPPL. 1, pp. 65–69, 2008.
- [90] G. Chau, W. Lui, S. Tsay, K. King, C. Loong, J. Chiu, C. Wu, and F. P'eng, "Prognostic significance of surgical margin in hepatocellular carcinoma resection: an analysis of 165 Childs' A patients," *J. Surg. Oncol.*, vol. 66, no. 2, pp. 122–126, 1997.
- [91] R. T.-P. Poon, S.-T. Fan, I. O.-L. Ng, and J. Wong, "Significance of resection margin in hepatectomy for hepatocellular carcinoma: a critical reappraisal," *Ann. Surg.*, vol. 231, no. 4, p. 544, 2000.
- [92] J. M. Llovet and J. Bruix, "Systematic review of randomized trials for unresectable hepatocellular carcinoma: chemoembolization improves survival," *Hepatology*, vol. 37, no. 2, pp. 429–442, 2003.
- [93] B. Sangro, L. Carpanese, R. Cianni, R. Golfieri, D. Gasparini, S. Ezziddin, P. M. Paprottka, F. Fiore, M. Van Buskirk, and J. I. Bilbao, "Survival after yttrium-90 resin microsphere radioembolization of hepatocellular carcinoma across Barcelona clinic liver cancer stages: a European evaluation," *Hepatology*, vol. 54, no. 3, pp. 868–878, 2011.
- [94] Y. Keisari, *Tumor ablation: effects on systemic and local anti-tumor immunity and on other tumor-microenvironment interactions*, vol. 5. Springer Science & Business Media, 2012.
- [95] D. P. Berry, A. R. Dennison, R. Ward, and G. J. Maddern, "Electrolytic ablation of colorectal liver metastases: 1-Year histological patient follow-up," *Dig. Surg.*, vol. 17, no. 5, pp. 518–519, 2000.

- [96] G. Gravante, S. L. Ong, M. S. Metcalfe, R. Sorge, A. J. Fox, D. M. Lloyd, G. J. Maddern, and A. R. Dennison, "Changes in acid-base balance during electrolytic ablation in an ex vivo perfused liver model," *Am. J. Surg.*, vol. 204, no. 5, pp. 666–670, 2012.
- [97] A. K. Majumdar, S. Islam, and A. Kim, "An Ultrasonically Powered Implantable Micro Electrolytic Ablation (IMEA) for Tumor Necrosis," in *Hilton Head Workshop*, 2018.
- [98] B. G. Fosh, J. G. Finch, A. A. Anthony, M. Texler, and G. J. Maddern, "Electrolytic ablation of the rat pancreas: A feasibility trial," *BMC Gastroenterol.*, vol. 1, 2001.
- [99] N. R. Perkons, E. J. Stein, C. Nwaezeapu, J. C. Wildenberg, K. Saleh, R. Itkin-ofar, D. Ackerman, M. C. Soulen, S. J. Hunt, G. J. Nadolski, and T. P. Gade, "Electrolytic ablation enables cancer cell targeting through pH modulation," *Commun. Biol.*, no. 2018, pp. 1–10.
- [100] K. P. Charpentier, F. Wolf, L. Noble, B. Winn, M. Resnick, and D. E. Dupuy, "Irreversible electroporation of the pancreas in swine: A pilot study," *Hpb*, vol. 12, no. 5, pp. 348–351, 2010.
- [101] M. K. Stehling, E. Guenther, P. Mikus, N. Klein, L. Rubinsky, and B. Rubinsky, "Synergistic combination of electrolysis and electroporation for tissue ablation," *PLoS One*, vol. 11, no. 2, pp. 1–23, 2016.
- [102] A. Kim, C. R. Powell, and B. Ziaie, "An implantable pressure sensing system with electromechanical interrogation scheme," *IEEE Trans. Biomed. Eng.*, vol. 61, no. 7, pp. 2209–2217, 2014.
- [103] A. Kim, M. Ochoa, R. Rahimi, and B. Ziaie, "New and Emerging Energy Sources for Implantable Wireless Microdevices," *Access, IEEE*, pp. 89–98, 2015.

VITA

Jiawei Zhou received his B.S. degree in Electrical Engineering from Huazhong University of Science and Technology, Wuhan, China in 2013. Since then, he has been a graduate research assistant at Ziaie Biomedical Microdevices Laboratory at Purdue University and pursuing a direct Ph.D. degree in Electrical and Computer Engineering at Purdue University, West Lafayette, IN. His research interest are ultrasonic powered electronic medical devices, and low-cost microsystems for biomedical applications using polymeric materials.

PUBLICATIONS

JOURNAL PUBLICATIONS

Zhou, Jiawei, Albert Kim, and Babak Ziaie. "An ultrasonically controlled switching system for power management in implantable devices." *Biomedical microdevices* 20, no. 2 (2018): 42.

Kim, Albert, **Jiawei Zhou**, Shayak Samaddar, Seung Hyun Song, Bennet D. Elzey, David H. Thompson, and Babak Ziaie. "An Implantable Ultrasonically-powered Micro-Light-source (μ Light) for photodynamic therapy." *Scientific reports* 9, no. 1 (2019): 1395.

Yoon, Chang Keun, Manuel Ochoa, Albert Kim, Rahim Rahimi, **Jiawei Zhou**, and Babak Ziaie. "Yeast Metabolic Response as an Indicator of Radiation Damage in Biological Tissue." *Advanced Biosystems* 2, no. 9 (2018): 1800126.

Park, J. H., A. Kim, H. Jiang, Seung Hyun Song, **J. Zhou**, and B. Ziaie. "A Wireless Chemical Sensing Scheme using Ultrasonic Imaging of Silica-Particle-Embedded Hydrogels (Silicagel)." *Sensors and Actuators B: Chemical* 259 (2018): 552-559.

CONFERENCE PUBLICATIONS

Zhou, Jiawei, Albert Kim, and Babak Ziaie. "An ultrasonically controlled power management system for implantable biomedical devices." In *2015 IEEE Biomedical Circuits and Systems Conference (BioCAS)*, pp. 1-4. IEEE, 2015.

Zhou, J., M. Ochoa, S. Samaddar, R. Rahimi, V. D. Badwaik, D. H. Thompson, and B. Ziaie. "A rapid micro-molding process for fabricating polymeric biodegradable 3D structures using hydrophobic elastomeric molds." In *2017 IEEE 30th International Conference on Micro Electro Mechanical Systems (MEMS)*, pp. 422-425. IEEE, 2017.

Zhou, Jiawei, Albert Kim, Manuel Ochoa, Hongjie Jiang, and Babak Ziaie. "An ultrasonically powered micropump for on-demand in-situ drug delivery." In *2016 IEEE 29th International Conference on Micro Electro Mechanical Systems (MEMS)*, pp. 349-352. IEEE, 2016.

Zhou, J., A. Kim, S. H. Song, and B. Ziaie. "An ultrasonically powered implantable micro-light source for localized photodynamic therapy." In *2015 Transducers-2015 18th International Conference on Solid-State Sensors, Actuators and Microsystems (TRANSDUCERS)*, pp. 876-879. IEEE, 2015.

Ochoa, M., **J. Zhou**, R. Rahimi, V. Badwaik, D. Thompson, and B. Ziaie. "Rapid 3D-print-and-shrink fabrication of biodegradable microneedles with complex geometries." In *2015 Transducers-2015 18th International Conference on Solid-State Sensors, Actuators and Microsystems (TRANSDUCERS)*, pp. 1251-1254. IEEE, 2015.

Seo, Weeseong, Wuyang Yu, Tianlin Tan, **Jiawei Zhou**, Tianshuo Zhang, Babak Ziaie, and Byunghoo Jung. "Diaper-embedded urinary tract infection monitoring system powered by a urine-powered battery." In *2015 IEEE Biomedical Circuits and Systems Conference (BioCAS)*, pp. 1-4. IEEE, 2015.